

## **Electronic Supplementary Information**

**for**

**Indium Phosphasalen Catalysts Showing High Isolelectivity and Activity in**

**Racemic Lactide and Lactone Ring Opening Polymerizations**

*Nattawut Yuntawattana,<sup>a</sup> Thomas M. McGuire,<sup>b</sup> Christopher B. Durr,<sup>a</sup> Antoine Buchard,<sup>b\*</sup> and*

*Charlotte K. Williams<sup>\*a</sup>*

<sup>a</sup> *Chemistry Research Laboratory, Department of Chemistry, University of Oxford, 12 Mansfield Road, Oxford, OX1 3TA, UK.*

<sup>b</sup> *Department of Chemistry, University of Bath, Claverton Down, Bath BA2 7AY, UK*

## Contents

<b>S1. General procedures</b>	<b>S3</b>
<b>S2. Experimental Section</b>	<b>S5</b>
<b>S2.1. Synthesis of phosphasalen ligands H<sub>2</sub>L<sup>1</sup>–H<sub>2</sub>L<sup>4</sup></b>	<b>S5</b>
<b>S2.2. Synthesis of indium complexes 1–5</b>	<b>S8</b>
<b>S2.3. Typical polymerization procedures</b>	<b>S10</b>
<b>S2.4. Polymer purification</b>	<b>S11</b>
<b>S2.5. Determination of PLA tacticity</b>	<b>S12</b>
<b>S2.6. Spectral characterization data for ligands H<sub>2</sub>L<sup>1</sup>–H<sub>2</sub>L<sup>4</sup></b>	<b>S12</b>
<b>S2.7. Spectral characterization data of indium complexes 1–5</b>	<b>S23</b>
<b>S2.8. Additional crystallographic data for ligand H<sub>2</sub>L<sup>4</sup></b>	<b>S35</b>
<b>S2.9. Additional crystallographic data for indium complexes 2–5 and intermediate 4'a</b>	<b>S37</b>
<b>S3. Additional polymerization data</b>	<b>S42</b>
<b>S4. Computational details</b>	<b>S56</b>
<b>S5. References</b>	<b>S76</b>

## S1. General procedures

### General procedure

All chemical reagents were obtained from commercial sources (Aldrich, Fisher and Fluorochem) and used as received unless stated otherwise. All solvents used in the reactions were collected from an MBraun solvent purification system (SPS) and degassed three times by freeze-pump-thaw before use. Tetrahydrofuran was distilled over Na/benzophenone, under a nitrogen atmosphere, and degassed three times before use. Benzene-*d*<sub>6</sub>, toluene-*d*<sub>8</sub>, and chloroform-*d* were distilled over CaH<sub>2</sub> and stored over activated molecular sieves, under nitrogen. THF-*d*<sub>8</sub> was degassed three times and stored over activated molecular sieves, under nitrogen. Racemic lactide was recrystallized from hot anhydrous toluene and sublimed three times before use.  $\epsilon$ -Caprolactone,  $\epsilon$ -decalactone,  $\delta$ -hexalactone, and  $\beta$ -butyrolactone were distilled over CaH<sub>2</sub> and degassed three times before use.

All reactions were carried out under a dry nitrogen atmosphere, using standard Schlenk techniques. The complexation reactions and polymerizations were performed in an MBraun glovebox (O<sub>2</sub> and water levels below 0.1 ppm) unless stated otherwise.

**NMR spectroscopy:** NMR spectra were recorded on Bruker Avance III HD Nanobay 400 MHz, Bruker Avance III 500 MHz and Bruker Avance III 500 MHz (with <sup>13</sup>C cryoprobe) NMR spectrometers. The following abbreviations are used in the report of spectra: s, singlet; bs, broad singlet; d, doublet, dd: doublet of doublets; t, triplet; q, quartet; quin; quintet; sex, sextet; sept, septet; m, multiplet.

**Gel permeation chromatography:** The molar masses and dispersity values of highly isotactic polylactide were recorded on an Agilent PL GPC-50 instrument, using HPLC grade CHCl<sub>3</sub> as the eluent, at a flow rate of 1.0 mL min<sup>-1</sup>, at 40 °C. In the case of other polyesters, GPC data were obtained using a Shimadzu LC-20AD instrument, with HPLC grade THF as the eluent, at 1.0 mL/min flow rate, at 30 °C. Two Polymer labs Mixed D columns were used in series. Narrow dispersity polystyrene standards were used to calibrate the instrument. The polyesters were dissolved in HPLC grade THF or CHCl<sub>3</sub> and filtered prior to analysis (200  $\mu$ m PTFE filter). The molar mass of the resultant PLA was corrected by a factor of 0.58 and a correction factor of 0.56 was used to correct the molar mass of resultant PCL.<sup>1</sup>

**Differential scanning calorimetry:** DSC data were recorded on DSC3+ (Mettler Toledo, Ltd). A sealed empty crucible was used as a reference, and the DSC was calibrated using indium and zinc standards. The PLA samples were heated from room temperature to 200 °C, at a rate of 5 °C min<sup>-1</sup>, under N<sub>2</sub> flow (100 mL min<sup>-1</sup>). Subsequently, the samples were cooled to -20 °C, at a rate of 5 °C·min<sup>-1</sup>, followed by a heating procedure from -20 °C to 200 °C, at a rate of 5 °C/min. Each sample was run for two heating-cooling cycles. The glass transition (*T*<sub>g</sub>) and melting (*T*<sub>m</sub>) temperatures reported are taken from the second heating cycle.

**Single crystal X-ray diffraction:** Air sensitive samples were isolated in a nitrogen glove box or on a Schlenk line and immediately immersed in fluorinated oil (Fomblin Y). Suitable single crystals were mounted on MiTeGen MicroMounts and cooled to 150 K under a stream of nitrogen with an Oxford Cryosystems Cryostream. Data collection was carried out with an Oxford Diffraction Supernova diffractometer using, Cu K $\alpha$  ( $\lambda = 1.5417 \text{ \AA}$ ) radiation. The resulting raw data was processed using CrysAlisPro. All the X-ray single crystal structures were solved using SHELXT and Full-matrix least-squares refinements, based on *F*<sup>2</sup>, were performed in SHELXL-14,<sup>2</sup> as incorporated in the WinGX package<sup>3</sup> by Dr. Christopher B. Durr .

All structures found in this paper were registered with the Cambridge Structural Database. CCDC 2018635 – 2018640 contains the supplementary crystallographic data for this paper. The data can be obtained free of charge from The Cambridge Crystallographic Data Centre via [www.ccdc.cam.ac.uk/structures](http://www.ccdc.cam.ac.uk/structures).

Structures **2**, **4'a**, **5** and **H<sub>2</sub>L<sup>4</sup>** all suffered from highly disordered lattice solvent. After numerous attempts to model excess solvent in each case, the SQUEEZE program as incorporated into PLATON was utilized.<sup>4,5</sup>

Several structures also showed disorder of ligands and solvent that could be successfully modeled:

**2**: A *para*-<sup>t</sup>Bu group was modeled in two locations and the occupancy was refined on a free variable. No restraints or constraints were required to achieve a stable refinement.

**4**: A *para*-<sup>t</sup>Bu group was modeled in two locations and the occupancy was refined on a free variable. Restraints were placed on the bond distances and thermal parameters to ensure a stable refinement.

**5**: Three separate areas of disorder were found: a *para*-<sup>t</sup>Bu group, the OEt group and the ligand backbone (en). In each case the disorder was modeled in two locations and refined on a free variable. To ensure a stable refinement, restraints on bond distances and thermal parameters were used.

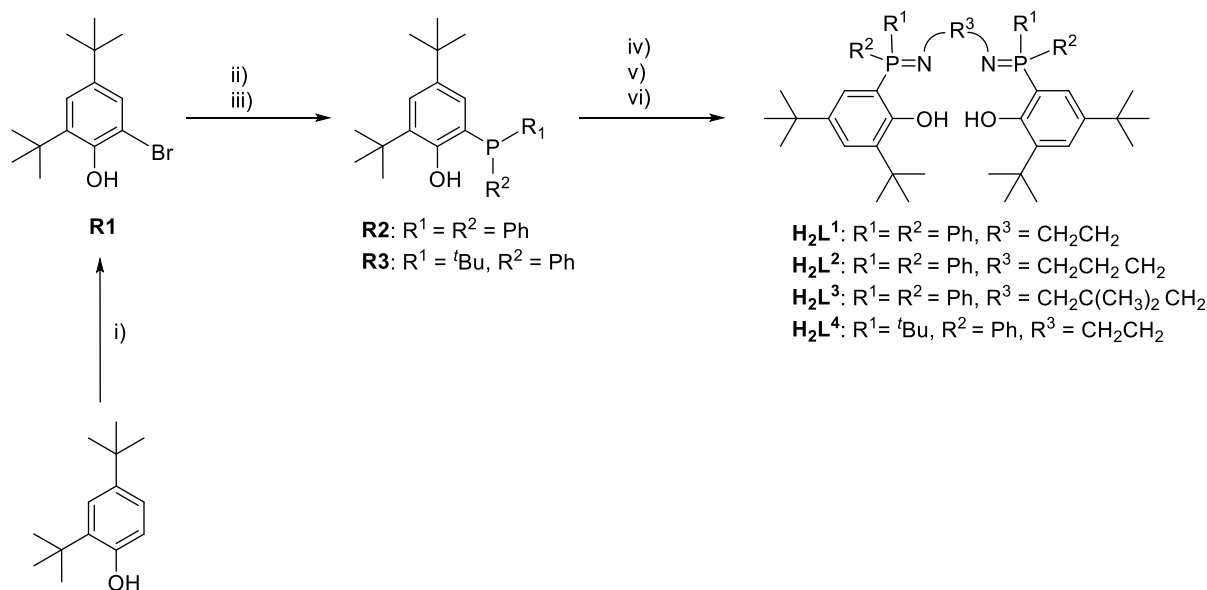
**H<sub>2</sub>L<sup>4</sup>**: A *para*-<sup>t</sup>Bu group was modeled in two locations and the occupancy was refined on a free variable. Restraints were placed on the bond distances to ensure a stable refinement.

**Elemental analysis:** were performed by Mr Stephen Boyer at London Metropolitan University.

**High-resolution mass spectrometry:** HRMS were performed on an Agilent 7200 quadrupole time of flight (Q-ToF) instrument, equipped with a direct insertion probe, supplied by Scientific Instrument Manufacturer (SIM) GmbH, using electron ionization (EI) as an ionization technique. Instrument control and data processing were performed using Agilent MassHunter software.

## S2. Experimental Section

### S2.1. Synthesis of phosphasalen ligands H<sub>2</sub>L<sup>1</sup>–H<sub>2</sub>L<sup>4</sup>



**Scheme S1.** i) NBS (1 equiv.), acetonitrile; ii) <sup>n</sup>BuLi (2.1 equiv.), Et<sub>2</sub>O, –78 °C, 1 h; iii) Ph<sub>2</sub>PCl or (<sup>t</sup>Bu)PhCl (1 equiv.), Et<sub>2</sub>O, –78 °C, 18 h; iv) Br<sub>2</sub> (1 equiv.), DCM, –78 °C, 2 h; v) <sup>n</sup>Bu<sub>3</sub>N (0.5 equiv.), vi) diamine backbone (0.5 equiv.) DCM, –78 °C, 18 h.

#### Synthesis of 2-bromo-4,6-di-*tert*-butylphenol (R1)

2-Bromo-4,6-di-*tert*-butylphenol was successfully synthesized according to the literature route.<sup>6</sup> To a solution of 2,4-di-*tert*-butylphenol (20.00 g, 96.93 mmol), in acetonitrile (300 mL), at 0 °C, was slowly added *N*-bromosuccinimide (17.25 g, 96.93 mmol), affording a clear yellow solution. The reaction mixture was then warmed to ambient temperature and allowed to stir overnight. The solution was washed with Na<sub>2</sub>SO<sub>3</sub> (10 mL of a 1 M) after which the solvent was removed under vacuum to give the product as a pale orange solid (21.84 g, 79%).

<sup>1</sup>H NMR (400.17 MHz, CDCl<sub>3</sub>): δ 7.32 (1H, d, <sup>4</sup>J<sub>HH</sub> = 2.3 Hz, ArH), 7.24 (1H, d, <sup>4</sup>J<sub>HH</sub> = 2.3 Hz, ArH), 5.65 (1H, s, OH), 1.41 (9H, s, ArH), 1.29 (9H, s, ArH).

<sup>13</sup>C NMR (125.82 MHz, CDCl<sub>3</sub>): δ 148.0 (ArCBr), 143.7 (ArCO), 136.7 (ArC), 126.2 (ArCH), 123.7 (ArCH), 111.9 (ArC), 35.6 (C(CH<sub>3</sub>)<sub>3</sub>), 34.4 (C(CH<sub>3</sub>)<sub>3</sub>), 31.4 (C(CH<sub>3</sub>)<sub>3</sub>), 29.4 (C(CH<sub>3</sub>)<sub>3</sub>).

Anal. Calc. (C<sub>14</sub>H<sub>21</sub>BrO): C, 58.95; H, 7.42 Found C, 58.87; H, 7.54

#### Synthesis of 2,4-di-*tert*-butyl-6-(diphenylphosphanyl)phenol (R2)

Compound **R2** was synthesized according to the reported procedure.<sup>7</sup> Under a nitrogen atmosphere, to a stirred solution of 2-bromo-4,6-di-*tert*-butylphenol (4.00 g, 14.02 mmol), in diethyl ether (50 mL) at –78 °C, was slowly added <sup>n</sup>BuLi (1.6 M in hexane, 18.41 mL, 29.45 mmol), affording a pale yellow suspension. The reaction mixture was allowed to stir at ambient temperature for 1 hour, generating a clear pale yellow solution. The cold bath was then reapplied and chlorodiphenylphosphine (2.59 mL, 14.02 mmol) was added to the cooled solution. The reaction mixture was warmed to room temperature and allowed to stir overnight, during which time a white suspension formed. The white suspension was washed with KH<sub>2</sub>PO<sub>4</sub> (120 mL of a 1 M solution). The organic layer was dried (MgSO<sub>4</sub>) and the solvent removed under vacuum to isolate the product (7.44 g, 45 %).

$^1\text{H}$  NMR (400 MHz,  $\text{CDCl}_3$ ):  $\delta$  7.31-7.22 (10H, m, ArH), 6.80 (1H, dd,  $^3J_{\text{HH}} = 5.8$  Hz,  $^4J_{\text{HH}} = 2.4$  Hz, ArH), 6.58 (1H, d,  $^3J_{\text{PH}} = 10.0$  Hz, ArH), 1.34 (9H, s,  $\text{CH}_3$ ), 1.07 (9H, s,  $\text{CH}_3$ ).

$^{13}\text{C}$  NMR (125 MHz,  $\text{CDCl}_3$ ):  $\delta$  155.9 (d,  $^2J_{\text{CP}} = 19.9$  Hz, ArCO), 142.2 (d,  $^3J_{\text{PC}} = 2.8$  Hz, ArC), 135.4 (d,  $^3J_{\text{PC}} = 3.8$  Hz, ArC), 135.2 (d,  $^1J_{\text{PC}} = 1.8$  Hz, ArC), 133.4 (ArCH), 133.2 (ArCH), 129.2 (ArCH), 128.8 (ArCH), 128.6 (d,  $^1J_{\text{PC}} = 3.8$  Hz, ArC), 128.5 (ArCH), 126.2 (ArCH), 119.9 (ArCH), 35.1 ( $\text{C}(\text{CH}_3)_3$ ), 34.4 ( $\text{C}(\text{CH}_3)_3$ ), 31.4 ( $\text{C}(\text{CH}_3)_3$ ), 29.6 ( $\text{C}(\text{CH}_3)_3$ ).

$^{31}\text{P}$  NMR (162 MHz,  $\text{CDCl}_3$ ):  $\delta$  -30.0 (s, P)

Anal. Calc. ( $\text{C}_{26}\text{H}_{31}\text{OP}$ ): C, 79.97; H, 8.00 Found C, 80.11; H, 8.11

### Synthesis of 2,4-di-*tert*-butyl-6-(*tert*-butyl(phenyl)phosphaneyl)phenol (R3)

Compound **R3** was synthesized by a modification to the route to **R2**. Chloro(*tert*-butyl)phenylphosphine (0.99 mL, 3.50 mmol) was used instead of chlorodiphenylphosphine. The product was obtained as colourless crystals (0.91 g, 47 %).

$^1\text{H}$  NMR (400 MHz,  $\text{CDCl}_3$ ):  $\delta$  7.61-7.54 (2H, m, ArH), 7.37-7.28 (5H, m, ArH), 1.41 (9H, s,  $\text{C}(\text{CH}_3)_3$ ), 1.28 (9H, s,  $\text{C}(\text{CH}_3)_3$ ), 1.19 (9H, d,  $^3J_{\text{PH}} = 13.7$  Hz,  $\text{C}(\text{CH}_3)_3$ ).

$^{13}\text{C}$  NMR (125 MHz,  $\text{CDCl}_3$ ):  $\delta$  157.3 (d,  $^2J_{\text{PC}} = 20.7$  Hz, ArCO), 140.8 (ArC), 135.1 (d,  $^1J_{\text{PC}} = 9.1$  Hz, ArC), 134.8 (ArC), 133.6 (d,  $^2J_{\text{PC}} = 16.9$  Hz, ArCH), 129.2 (ArCH), 128.2 (ArC), 128.1 (d,  $^2J_{\text{PC}} = 8.0$  Hz, ArCH), 125.9 (ArCH), 118.3 (ArCH), 35.1 ( $\text{C}(\text{CH}_3)_3$ ), 34.3 ( $\text{C}(\text{CH}_3)_3$ ), 31.6 ( $\text{C}(\text{CH}_3)_3$ ), 31.4 (d,  $^1J_{\text{PC}} = 7.8$  Hz,  $\text{C}(\text{CH}_3)_3$ ), 29.5 ( $\text{C}(\text{CH}_3)_3$ ), 28.6 (d,  $^2J_{\text{PC}} = 14.4$  Hz,  $\text{C}(\text{CH}_3)_3$ ).

$^{31}\text{P}$  NMR (162 MHz,  $\text{CDCl}_3$ ):  $\delta$  -19.2 (s, P).

HRMS (EI) Calc. ( $\text{C}_{24}\text{H}_{35}\text{OP}$ ): m/z: 370.2420 Found: m/z 370.2414

### Synthesis of ligand **H<sub>2</sub>L<sup>1</sup>**

Ligand **H<sub>2</sub>L<sup>1</sup>** was prepared following the literature method.<sup>8</sup> Under a nitrogen atmosphere, liquid bromine (0.26 mL, 5.12 mmol) was slowly added to a stirred solution of **R2** (2.00 g, 5.12 mmol), in dichloromethane (60 mL) at  $-78$  °C, affording a clear yellow solution. The reaction mixture was then allowed to stir at room temperature for 2 hours. The reaction mixture was cooled again and tributylamine (0.61 mL, 2.56 mmol) and ethylenediamine (0.17 mL, 2.56 mmol) were slowly added to it affording a pale yellow solution. The reaction mixture was allowed to stir at ambient temperature overnight during which time a pale yellow suspension formed. The reaction mixture was filtered and the filtrate dried under vacuum to give a yellow oil. The crude oil was vigorously stirred in THF (10 mL) for 20 minutes during which time a white solid precipitated. The white solid was filtered and was purified by column chromatography ( $\text{Al}_2\text{O}_3$ , DCM:EtOH = 40:1). The product was isolated under as a pale yellow powder (0.46 g, 11 %).

$^1\text{H}$  NMR (400 MHz,  $\text{CDCl}_3$ ):  $\delta$  7.66-7.50 (12H, m, ArH), 7.45-7.37 (8H, m, ArH), 7.36 (2H, d,  $^4J_{\text{HH}} = 2.6$  Hz, ArH), 6.21 (2H, dd,  $^4J_{\text{HH}} = 2.6$  Hz,  $^3J_{\text{PH}} = 15.7$  Hz, ArH), 5.29 (2H, s, OH), 3.21-3.10 (4H, m,  $\text{CH}_2$ ), 1.39 (18H, s,  $\text{CH}_3$ ), 1.07 (18H, s,  $\text{CH}_3$ ).

$^{13}\text{C}$  NMR (125 MHz,  $\text{CDCl}_3$ ):  $\delta$  173.5 (ArCO), 140.2 (d,  $^3J_{\text{PC}} = 9.4$  Hz, ArC), 133.4 (d,  $^1J_{\text{PC}} = 10.3$  Hz, ArC), 132.7 (d,  $^3J_{\text{PC}} = 2.6$  Hz, ArC), 129.9 (ArCH), 129.0 (d,  $^3J_{\text{PC}} = 12.2$  Hz, ArCH), 126.4 (ArCH), 126.2 (d,  $^2J_{\text{PC}} = 14.4$  Hz, ArCH), 125.6 (ArCH), 101.3 (d,  $^1J_{\text{PC}} = 112.5$  Hz, ArC), 44.0 (dd.

$^2J_{PC} = 10.3$  Hz,  $^3J_{PC} = 3.5$  Hz, CH<sub>2</sub>), 35.3 (d,  $^4J_{PC} = 2.0$  Hz, C(CH<sub>3</sub>)<sub>3</sub>), 33.9 (d,  $^4J_{PC} = 1.1$  Hz, C(CH<sub>3</sub>)<sub>3</sub>), 31.5 (C(CH<sub>3</sub>)<sub>3</sub>), 29.3 (C(CH<sub>3</sub>)<sub>3</sub>).

$^{31}P$  NMR (162 MHz, CDCl<sub>3</sub>):  $\delta$  41.8 (s, P)

Anal. Calc. (C<sub>54</sub>H<sub>66</sub>N<sub>2</sub>O<sub>2</sub>P<sub>2</sub>): C, 77.48; H, 7.95; N, 3.35 found C, 77.35; H, 8.01; N, 3.42

### Synthesis of ligand H<sub>2</sub>L<sup>2</sup>

Ligand H<sub>2</sub>L<sup>2</sup> was synthesized according to the procedure used to prepare H<sub>2</sub>L<sup>1</sup>. 1,3-Diaminopropane (0.21 mL, 2.56 mmol) was used instead of ethylenediamine. The product was isolated as a yellow solid after column chromatography (Al<sub>2</sub>O<sub>3</sub>, DCM:EtOH = 40:1) (0.98 g, 22 %)

$^1H$  NMR (400 MHz, CDCl<sub>3</sub>):  $\delta$  7.69-7.48 (12H, m, ArH), 7.48-7.31 (10H, m, ArH), 6.23 (2H, d,  $^4J_{HH} = 16.2$  Hz, ArH), 2.96 (4H, bs, CH<sub>2</sub>), 1.75 (2H, bs, CH<sub>2</sub>), 1.41 (18H, s, C(CH<sub>3</sub>)<sub>3</sub>), 1.07 (18H, s, C(CH<sub>3</sub>)<sub>3</sub>).

$^{13}C$  NMR (125 MHz, CDCl<sub>3</sub>):  $\delta$  173.6 (ArCO), 140.4 (d,  $^3J_{PC} = 9.6$  Hz, ArC), 133.5 (d,  $^1J_{PC} = 10.3$  Hz, ArC), 132.9 (d,  $^3J_{PC} = 2.5$  Hz, ArC), 129.7 (ArCH), 129.0 (d,  $^3J_{PC} = 12.2$  Hz, ArCH), 125.8 (ArCH), 125.6 (d,  $^2J_{PC} = 14.2$  Hz, ArCH), 125.0 (ArCH), 100.4 (d,  $^1J_{PC} = 113.5$  Hz, ArC), 40.2 (d,  $^{2/3}J_{PC} = 4.4$  Hz, CH<sub>2</sub>), 35.4 (d,  $^4J_{PC} = 1.9$  Hz, C(CH<sub>3</sub>)<sub>3</sub>), 33.9 (d,  $^4J_{PC} = 1.2$  Hz, C(CH<sub>3</sub>)<sub>3</sub>), 31.5 (C(CH<sub>3</sub>)<sub>3</sub>), 29.3 (C(CH<sub>3</sub>)<sub>3</sub>).

$^{31}P$  NMR (162 MHz, CDCl<sub>3</sub>):  $\delta$  41.8 (s, P)

Anal. Calc. (C<sub>55</sub>H<sub>68</sub>N<sub>2</sub>O<sub>2</sub>P<sub>2</sub>): C, 77.62; H, 8.05; N, 3.19 Found C, 77.70; H, 8.14; N, 3.22

### Synthesis of ligand H<sub>2</sub>L<sup>3</sup>

Ligand H<sub>2</sub>L<sup>3</sup> was synthesized according to the procedure used to make H<sub>2</sub>L<sup>1</sup>. 2,2-Dimethyl-1,3-propanediamine (0.31 mL, 2.56 mmol) was used instead of ethylenediamine. The product was isolated as a yellow solid after column chromatography (Al<sub>2</sub>O<sub>3</sub>, DCM:EtOH = 40:1) (0.64 g, 14 %).

$^1H$  NMR (400 MHz, CDCl<sub>3</sub>):  $\delta$  7.69-7.60 (8H, m, ArH), 7.60-7.52 (4H, m, ArH), 7.45-7.35 (10H, m, ArH), 6.25 (2H, dd,  $^4J_{HH} = 2.6$  Hz,  $^3J_{PH} = 16.1$  Hz, ArH), 5.30 (2H, s, OH), 2.78 (4H, d,  $^2J_{HH} = 6.8$  Hz, CH<sub>2</sub>), 1.41 (18H, s, C(CH<sub>3</sub>)<sub>3</sub>), 1.06 (18H, s, C(CH<sub>3</sub>)<sub>3</sub>), 0.91 (6H, s, CH<sub>3</sub>).

$^{13}C$  NMR (125 MHz, CDCl<sub>3</sub>):  $\delta$  173.0 (d,  $^2J_{PC} = 4.2$  Hz, ArCO), 140.3 (d,  $^3J_{PC} = 9.3$  Hz, ArC), 133.7 (d,  $^1J_{PC} = 10.0$  Hz, ArC), 132.9 (d,  $^3J_{PC} = 2.6$  Hz, ArC), 129.5 (ArCH), 129.0 (d,  $^3J_{PC} = 11.9$  Hz, ArCH), 125.8 (ArCH), 125.6 (d,  $^2J_{PC} = 13.9$  Hz, ArCH), 125.1 (ArCH), 100.8 (d,  $^1J_{PC} = 113.4$  Hz, ArC), 51.1 (d,  $^2J_{PC} = 5.8$  Hz, CH<sub>2</sub>), 37.2 (t,  $^3J_{PC} = 12.3$  Hz, (C(CH<sub>3</sub>)<sub>2</sub>), 35.4 (d,  $^4J_{PC} = 2.0$  Hz, C(CH<sub>3</sub>)<sub>3</sub>), 33.9 (d,  $^4J_{PC} = 1.1$  Hz, C(CH<sub>3</sub>)<sub>3</sub>), 31.5 (C(CH<sub>3</sub>)<sub>3</sub>), 29.4 (C(CH<sub>3</sub>)<sub>3</sub>), 23.6 (C(CH<sub>3</sub>)<sub>2</sub>).

$^{31}P$  NMR (162 MHz, CDCl<sub>3</sub>):  $\delta$  41.6 (s, P)

Anal. Calc. (C<sub>57</sub>H<sub>72</sub>N<sub>2</sub>O<sub>2</sub>P<sub>2</sub>): C, 77.87; H, 8.26; N, 3.19 Found C, 77.84; H, 8.36; N, 3.25

## Synthesis of ligand $\mathbf{H_2L^4}$

Ligand  $\mathbf{H_2L^4}$  was synthesized according to the procedure used for  $\mathbf{H_2L^1}$ .  $\mathbf{R_3}$  (1.00 g, 2.70 mmol) was used instead of  $\mathbf{R_2}$ . After column chromatography, a crude pink oil was isolated and crystallized using cold pentane to afford the product as pale pink crystals (0.22 g, 10%).

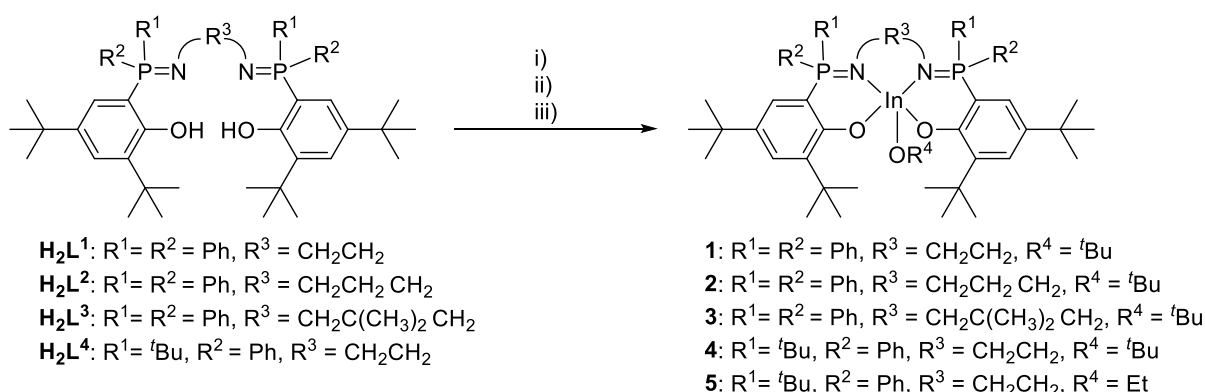
$^1\text{H}$  NMR (400 MHz,  $\text{CDCl}_3$ ):  $\delta$  7.97-7.88 (4H, m, ArH), 7.57-7.50 (2H, m, ArH), 7.48-7.40 (4H, m, ArH), 7.33 (2H, d,  $^4J_{\text{HH}} = 2.6$  Hz, ArH), 6.80 (2H, dd,  $^4J_{\text{HH}} = 2.6$  Hz,  $^3J_{\text{PH}} = 13.7$  Hz, ArH), 3.08-2.83 (4H, m,  $\text{CH}_2$ ), 1.42 (9H, s,  $\text{C}(\text{CH}_3)_3$ ), 1.30 (9H, d,  $^3J_{\text{PH}} = 15.5$  Hz,  $\text{C}(\text{CH}_3)_3$ ), 1.16 (9H, s,  $\text{C}(\text{CH}_3)_3$ ).

$^{13}\text{C}$  NMR (125 MHz,  $\text{CDCl}_3$ ):  $\delta$  173.8 (weak, ArCO), 140.6 (d,  $^1J_{\text{PC}} = 8.4$  Hz, ArC), 133.4 (d,  $^3J_{\text{PC}} = 8.6$  Hz, ArCH), 131.8 (d,  $^4J_{\text{PC}} = 2.8$  Hz, ArCH), 130.7 (d,  $^1J_{\text{PC}} = 11$  Hz, ArC), 128.9 (ArCH), 128.2 (d,  $^2J_{\text{PC}} = 11.4$  Hz, ArCH), 127.4 (d,  $^2J_{\text{PC}} = 12.9$  Hz, ArCH), 125.8 (ArC), 124.8 (ArC), 43.2 (dd,  $^3J_{\text{PC}} = 2.6$  Hz,  $^2J_{\text{PC}} = 8.0$  Hz,  $\text{CH}_2$ ), 36.1 ( $\text{C}(\text{CH}_3)_3$ ), 35.4 (d,  $^1J_{\text{PC}} = 27.2$  Hz,  $\text{C}(\text{CH}_3)_3$ ), 33.9 ( $\text{C}(\text{CH}_3)_3$ ), 31.6 ( $\text{C}(\text{CH}_3)_3$ ), 29.2 ( $\text{C}(\text{CH}_3)_3$ ), 26.7 ( $\text{C}(\text{CH}_3)_3$ ).

$^{31}\text{P}\{^1\text{H}\}$  NMR (162 MHz,  $\text{CDCl}_3$ ):  $\delta$  55.9 (s, P)

Anal. Calc. ( $\text{C}_{50}\text{H}_{74}\text{N}_2\text{O}_2\text{P}_2$ ): C, 75.34; H, 9.36; N, 3.51 Found C, 75.42; H, 9.50; N, 3.54

## S2.2. Synthesis of indium complexes 1–5



**Scheme S2.** i)  $\text{KN}(\text{Si}(\text{CH}_3)_3)_2$  (2 equiv.), THF, 25 °C; ii)  $\text{InCl}_3$  (1 equiv.), THF, 25 °C, 1 h; iii)  $\text{KO}^t\text{Bu}$  or  $\text{KOEt}$  (1 equiv.), THF, 25 °C.

## Synthesis of indium complex 1

Complex **1** was synthesized according to a published procedure.<sup>10</sup> A solution of potassium bis(trimethylsilyl)amide (0.14 g, 0.72 mmol) in THF (3 mL) was added into a suspension of  $\mathbf{H_2L^1}$  (0.30 g, 0.36 mmol) in THF (8 mL). The reaction mixture was allowed to stir at room temperature for 2 hours. An aliquot was analysed with  $^{31}\text{P}\{^1\text{H}\}$  NMR spectroscopy.  $\text{InCl}_3$  (0.08 g, 0.72 mmol) was then added and the reaction was allowed to stir, at room temperature, for 2 hours. An aliquot was analysed with  $^{31}\text{P}\{^1\text{H}\}$  NMR spectroscopy, before addition of  $\text{KO}^t\text{Bu}$  (0.04 g, 0.36 mmol). The reaction mixture was then allowed to stir at room temperature overnight. The suspension was centrifuged to remove the KCl salt. The solvent layer was separated, filtered and dried under vacuum to give the product as a white solid (0.28 g, 76 %).

$^1\text{H}$  NMR (400 MHz,  $\text{THF-d}_3$ ):  $\delta$  7.81-7.72 (4H, m, ArH), 7.67-7.53 (6H, m, ArH), 7.52-7.43 (6H, m, ArH), 7.38-7.29 (6H, m, ArH), 6.34 (2H, dd,  $^4J_{\text{HH}} = 2.2$  Hz,  $^3J_{\text{PH}} = 17.2$  Hz, ArH), 3.13-2.81 (4H, m,  $\text{CH}_2$ ), 1.51 (18H, s,  $\text{C}(\text{CH}_3)_3$ ), 1.06-0.92 (27H, m,  $\text{CH}_3$ )

$^{13}\text{C}\{^1\text{H}\}$  NMR (125 MHz, THF- $d_8$ ):  $\delta$  171.2 (d,  $^2J_{\text{PC}} = 2.8$  Hz, ArCO), 142.7 (d,  $^3J_{\text{PC}} = 9.7$  Hz, ArC), 135.0 (d,  $^3J_{\text{PC}} = 8.70$  Hz, ArC), 133.5 (d,  $^2J_{\text{PC}} = 9.7$  Hz, ArCH), 132.8 (d,  $^1J_{\text{PC}} = 97.1$  Hz, ArC), 129.6 (d,  $^4J_{\text{PC}} = 11.7$  Hz, ArCH), 129.4 (d,  $^3J_{\text{PC}} = 10.7$  Hz, ArCH), 129.1 (ArCH), 127.3 (d,  $^2J_{\text{PC}} = 13.7$  Hz, ArCH), 108.6 (d,  $^1J_{\text{PC}} = 118.6$  Hz, ArC), 69.1 (OC(CH $_3$ ) $_3$ ), 47.0 (d,  $^2J_{\text{PC}} = 8.5$  Hz, CH $_2$ ), 36.7 (C(CH $_3$ ) $_3$ ), 34.5 (C(CH $_3$ ) $_3$ ), 31.8 (C(CH $_3$ ) $_3$ ), 31.0 (C(CH $_3$ ) $_3$ ) 30.8 (OC(CH $_3$ ) $_3$ ),.

$^{31}\text{P}\{^1\text{H}\}$  NMR (162 MHz, THF- $d_8$ ):  $\delta$  40.2 (s, P)

Anal. Calc. (C $_{58}$ H $_{73}$ InN $_2$ O $_3$ P $_2$ ): C, 68.10; H, 7.19; N, 2.74 Found C, 68.18; H, 7.30; N, 2.62

### Synthesis of indium complex 2

Complex **2** was synthesized according to the method used to prepare **1**. **H $_2$ L $^2$**  (0.30 g, 0.35 mmol) was used instead of **H $_2$ L $^1$** . The product was isolated as a white powder, after washing with hexane (0.16 g, 44 %).

$^1\text{H}$  NMR (400 MHz, THF- $d_8$ ):  $\delta$  7.77-7.62 (8H, m, ArH), 7.62-7.33 (12H, m, ArH), 7.31 (2H, d,  $^4J_{\text{HH}} = 2.4$  Hz, ArH), 6.42 (2H, dd,  $^3J_{\text{PH}} = 16.5$  Hz,  $^4J_{\text{HH}} = 2.4$  Hz, ArH), 3.49-2.95 (6H, bs, CH $_2$ ), 1.30 (18H, s, C(CH $_3$ ) $_3$ ), 1.06 (18H, s, C(CH $_3$ ) $_3$ ), 1.04 (9H, s, C(CH $_3$ ) $_3$ ).

$^{13}\text{C}\{^1\text{H}\}$  NMR (125 MHz, THF- $d_8$ ):  $\delta$  171.0 (d,  $^2J_{\text{PC}} = 2.7$  Hz, ArCO), 142.4 (d,  $^3J_{\text{PC}} = 10.2$  Hz, ArC), 135.2 (d,  $^3J_{\text{PC}} = 14.5$  Hz, ArC), 134.4 (bs, ArCH), 132.7 (bs, ArC), 129.4 (d,  $^{3/4}J_{\text{PC}} = 10.9$  Hz, ArCH), 129.0 (ArCH), 127.3 (d,  $^2J_{\text{PC}} = 12.8$  Hz, ArCH), 109.6 (d,  $^1J_{\text{PC}} = 113.8$  Hz, ArC), 69.2 (OC(CH $_3$ ) $_3$ ), 46.5 (CH $_2$ ), 44.4 (CH $_2$ CH $_2$ CH $_2$ ), 36.4 (C(CH $_3$ ) $_3$ ), 34.6 (C(CH $_3$ ) $_3$ ), 31.9 (C(CH $_3$ ) $_3$ ), 30.8 (C(CH $_3$ ) $_3$ ), 30.5 (OC(CH $_3$ ) $_3$ ).

$^{31}\text{P}\{^1\text{H}\}$  NMR (162 MHz, THF- $d_8$ ):  $\delta$  40.3 (s, P)

Anal. Calc. (C $_{59}$ H $_{75}$ InN $_2$ O $_3$ P $_2$ ): C, 68.33; H, 7.29; N, 2.70 Found C, 67.81; H, 6.90; N, 2.78.

### Synthesis of indium complex 3

Complex **3** was synthesized according to the procedure used to make **1**. **H $_2$ L $^3$**  (0.13 g, 0.14 mmol) was used instead of **H $_2$ L $^1$** . The product was isolated as a white powder, after washing with hexane (0.07 g, 43 %).

$^1\text{H}$  NMR (400 MHz, THF- $d_8$ ):  $\delta$  7.99-7.88 (4H, m, ArH), 7.67-7.44 (12H, m, ArH), 7.43-7.34 (4H, m, ArH), 7.33 (2H, d,  $^4J_{\text{HH}} = 2.6$  Hz, ArH), 6.58 (2H, dd,  $^4J_{\text{HH}} = 2.5$  Hz,  $^3J_{\text{PH}} = 16.2$  Hz, ArH), 3.41-3.26 (2H, m, CH $_2$ ), 2.93-2.80 (2H, m, CH $_2$ ), 1.33 (18H, s, CH $_3$ ), 1.11-1.05 (27H, m, CH $_3$ ), 0.60 (3H, s, CH $_3$ ), 0.13 (3H, s, CH $_3$ )

$^{13}\text{C}\{^1\text{H}\}$  NMR (125 MHz, THF- $d_8$ ):  $\delta$  171.4 (d,  $^2J_{\text{PC}} = 3.8$  Hz, ArCO), 142.3 (d,  $^3J_{30\text{PC}} = 9.9$  Hz, ArC), 135.4 (d,  $^4J_{\text{PC}} = 15.0$  Hz, ArCH), 135.1 (d,  $^{2/3}J_{\text{PC}} = 9.9$  Hz, ArCH), 134.7 (d,  $^{2/3}J_{\text{PC}} = 9.5$  Hz, ArCH), 132.7 (d,  $^{2/3}J_{\text{PC}} = 10.4$  Hz, ArCH), 131.7 (d,  $^1J_{\text{PC}} = 92.3$ , ArC), 130.3 (d,  $^1J_{\text{PC}} = 88.5$  Hz, ArC), 129.1 (d,  $^{2/3}J_{\text{PC}} = 11.5$  Hz, ArCH), 128.9 (ArCH), 127.6 (d,  $^2J_{\text{PC}} = 13.2$  Hz, ArCH), 109.2 (d,  $^1J_{\text{PC}} = 114.7$  Hz, ArC), 69.6 (C(CH $_3$ ) $_3$ ), 57.1 (d,  $^2J_{\text{PC}} = 7.8$  Hz, CH $_2$ ), 37.6 (d,  $^3J_{\text{PC}} = 10.0$  Hz, C(CH $_3$ ) $_2$ ), 36.5 (C(CH $_3$ ) $_3$ ), 35.3 (C(CH $_3$ ) $_3$ ), 34.6 (C(CH $_3$ ) $_3$ ), 31.8 (C(CH $_3$ ) $_3$ ), 30.8 (C(CH $_3$ ) $_3$ ), 26.4 (C(CH $_3$ ) $_2$ ), 25.9 (C(CH $_3$ ) $_2$ ).

$^{31}\text{P}\{^1\text{H}\}$  NMR (162 MHz, THF- $d_8$ ):  $\delta$  40.6 (s, P)

Anal. Calc. (C $_{61}$ H $_{79}$ InN $_2$ O $_3$ P $_2$ ): C, 68.79; H, 7.48; N, 2.63 Found C, 68.90; H, 7.62; N, 2.45

## Synthesis of indium complex 4

Complex **4** was synthesized according to the method used to make **1**. **H<sub>2</sub>L<sup>4</sup>** (0.12 g, 0.15 mmol) was used instead of **H<sub>2</sub>L<sup>1</sup>**. The product was isolated as a white powder, after washing with hexane (0.01 g, 64%).

<sup>1</sup>H NMR (400 MHz, THF-d<sub>8</sub>): δ 8.27-8.16 (4H, m, ArH), 7.64-7.52 (6H, m, ArH), 7.31 (2H, d, <sup>4</sup>J<sub>HH</sub> = 2.4 Hz, ArH), 6.22 (2H, dd, <sup>3</sup>J<sub>PH</sub> = 16.7 Hz, <sup>4</sup>J<sub>HH</sub> = 2.6 Hz, ArH), 5.51 (2H, s, OH), 3.13-2.85 (4H, m, CH<sub>2</sub>), 1.54 (18H, s, C(CH<sub>3</sub>)<sub>3</sub>), 1.43 (18H, d, <sup>3</sup>J<sub>PH</sub> = 14.5 Hz, C(CH<sub>3</sub>)<sub>3</sub>), 1.02 (18H, s, C(CH<sub>3</sub>)<sub>3</sub>), 0.99 (9H, s, C(CH<sub>3</sub>)<sub>3</sub>).

<sup>13</sup>C{<sup>1</sup>H} NMR (125 MHz, THF-d<sub>8</sub>): δ 171.3 (d, <sup>3</sup>J<sub>PC</sub> = 3.8 Hz, ArCO), 142.6 (d, <sup>4</sup>J<sub>PC</sub> = 10.4 Hz, ArC), 134.9 (d, <sup>2</sup>J<sub>PC</sub> = 7.9 Hz, ArCH), 134.5 (d, <sup>1</sup>J<sub>PC</sub> = 14.3 Hz, ArC), 132.7 (d, <sup>4</sup>J<sub>PC</sub> = 2.6 Hz, ArCH), 130.4 (ArC), 129.5 (d, <sup>3</sup>J<sub>PC</sub> = 10.4 Hz, ArCH), 128.8 (d, <sup>2</sup>J<sub>PC</sub> = 13.3 Hz, ArCH), 128.2 (d, <sup>4</sup>J<sub>PC</sub> = 2.5 Hz, ArCH), 106.9 (d, <sup>1</sup>J<sub>PC</sub> = 105.8, ArC), 68.9 (OC(CH<sub>3</sub>)<sub>3</sub>), 48.6 (dd, <sup>3</sup>J<sub>PC</sub> = 5.0 Hz, <sup>2</sup>J<sub>PC</sub> = 12.5 Hz, CH<sub>2</sub>), 38.8 (C(CH<sub>3</sub>)<sub>3</sub>), 36.7 (d, <sup>4</sup>J<sub>PC</sub> = 1.7 Hz, C(CH<sub>3</sub>)<sub>3</sub>), 35.5 (C(CH<sub>3</sub>)<sub>3</sub>), 34.4 (C(CH<sub>3</sub>)<sub>3</sub>), 31.7 (C(CH<sub>3</sub>)<sub>3</sub>), 31.1 (C(CH<sub>3</sub>)<sub>3</sub>), 28.0 (C(CH<sub>3</sub>)<sub>3</sub>)

<sup>31</sup>P{<sup>1</sup>H} NMR (162 MHz, THF-d<sub>8</sub>): δ 56.4 (s, P)

Anal. Calc. (C<sub>54</sub>H<sub>81</sub>InN<sub>2</sub>O<sub>3</sub>P<sub>2</sub>): C, 65.98; H, 8.31; N, 2.85 Found C, 65.85; H, 8.16; N, 2.97

## Synthesis of indium complex 5

Complex **5** was synthesized according to procedure used for to make **1** but, with ligand **H<sub>2</sub>L<sup>4</sup>** instead of **H<sub>2</sub>L<sup>1</sup>** and KOEt (0.02 g, 0.26 mmol) instead of KO<sup>t</sup>Bu. The product was isolated as colourless crystals (0.08 g, 41 %).

<sup>1</sup>H NMR (400 MHz, THF-d<sub>8</sub>): δ 8.21-8.13 (4H, m, ArH), 7.64-7.54 (6H, m, ArH), 7.31 (2H, <sup>4</sup>J<sub>HH</sub> = 2.5 Hz, ArH), 6.33 (2H, dd, <sup>3</sup>J<sub>PH</sub> = 16.6 Hz, <sup>4</sup>J<sub>HH</sub> = 2.6 Hz, ArH), 3.70 (2H, q, <sup>3</sup>J<sub>HH</sub> = 6.2 Hz, OCH<sub>2</sub>CH<sub>3</sub>), 3.11-2.83 (4H, m, CH<sub>2</sub>), 1.53 (18H, s, CH<sub>3</sub>), 1.44 (18H, d, <sup>3</sup>J<sub>PH</sub> = 14.6 Hz, CH<sub>3</sub>), 1.02 (18H, s, CH<sub>3</sub>), 0.82 (3H, t, <sup>3</sup>J<sub>HH</sub> = 6.3 Hz, OCH<sub>2</sub>CH<sub>3</sub>).

<sup>13</sup>C{<sup>1</sup>H} NMR (125 MHz, THF-d<sub>8</sub>): δ 171.3 (d, <sup>3</sup>J<sub>PC</sub> = 3.4 Hz, ArCO), 142.5 (d, <sup>1</sup>J<sub>PC</sub> = 9.9 Hz, ArC), 134.8 (d, <sup>2</sup>J<sub>PC</sub> = 7.9 Hz, ArCH), 132.8 (d, <sup>4</sup>J<sub>PC</sub> = 2.5 Hz, ArCH), 130.3 (ArC), 129.6 (d, <sup>3</sup>J<sub>PC</sub> = 10.3 Hz, ArCH), 129.0 (d, <sup>2</sup>J<sub>PC</sub> = 13.3 Hz, ArCH), 128.3 (d, <sup>4</sup>J<sub>PC</sub> = 1.9 Hz, ArCH), 107.7 (ArC), 106.8 (ArC), 62.2 (OCH<sub>2</sub>CH<sub>3</sub>), 48.9 (dd, <sup>3</sup>J<sub>PC</sub> = 4.1 Hz, <sup>2</sup>J<sub>PC</sub> = 11.3 Hz, CH<sub>2</sub>), 38.8 (d, <sup>1</sup>J<sub>PC</sub> = 57.1 Hz, C(CH<sub>3</sub>)<sub>3</sub>), 36.7 (d, <sup>4</sup>J<sub>PC</sub> = 1.7 Hz, C(CH<sub>3</sub>)<sub>3</sub>), 34.4 (C(CH<sub>3</sub>)<sub>3</sub>), 31.8 (C(CH<sub>3</sub>)<sub>3</sub>), 30.9 (C(CH<sub>3</sub>)<sub>3</sub>), 28.0 (C(CH<sub>3</sub>)<sub>3</sub>), 22.8 (OCH<sub>2</sub>CH<sub>3</sub>).

<sup>31</sup>P{<sup>1</sup>H} NMR (162 MHz, THF-d<sub>8</sub>): δ 56.9 (s, P)

Anal. Calc. (C<sub>54</sub>H<sub>81</sub>InN<sub>2</sub>O<sub>3</sub>P<sub>2</sub>): C, 65.40; H, 8.25; N, 2.93 Found C, 65.52; H, 8.25; N, 2.72

## S2.3. Typical polymerization procedures

### S2.3.1. Lactide polymerization

All lactide polymerizations (except low temperature polymerization) were conducted in vials, in a nitrogen filled glove box, at room temperature. The polymerization vessels were charged with LA (0.288 g, 2 mmol) and dissolved in THF (1.5 mL). To this, the required volume, taken from stock solution, of catalyst (0.5 mL, 8 mM) was added such that the overall [LA] = 1 M and [In] = 2 mM.

Aliquots were withdrawn from the reaction mixture at predetermined times and quenched by exposure to air and by the addition of wet hexane (~ 1 mL). The crude products, after solvent evaporation, were analysed by  $^1\text{H}$  NMR ( $^1\text{H}\{^1\text{H}\}$  NMR, where applicable) spectroscopy and GPC. The tacticity ( $P_1$  or  $P_2$ ) was determined by the integration of the tetrads observed in the  $^1\text{H}\{^1\text{H}\}$  NMR spectrum and using Bernoullian statistics.<sup>11</sup> In some cases, the PLA was purified (see below) and analysed by DSC.

For low temperature LA polymerization, reactions were set-up in a nitrogen filled glove box maintaining the desired concentrations of LA and catalyst. The polymerization ampoules were sealed under nitrogen, removed from the glove box and cooled to 278 K (using a cooling bath). Aliquots were taken at specific times and analysed by  $^1\text{H}$  NMR spectroscopy and GPC.

### **S2.3.2. Typical polymerization procedure ( $\epsilon$ -caprolactone)**

In a glove box, a polymerization vessel was loaded with catalyst (0.5 mL from a stock solution at 5mM in THF, 2.5  $\mu\text{mol}$ ), THF (0.61 mL) and  $\epsilon$ -CL (0.14 mL, 1.25 mmol). The reaction vessel was sealed and allowed to stir at room temperature. At predetermined reaction times, aliquots were withdrawn and quenched by addition into wet  $\text{CDCl}_3$ . The crude products were characterised by NMR spectroscopy and GPC.

### **S2.3.3. Typical polymerization procedure ( $\beta$ -butyrolactone)**

In a glove box, a polymerization vessel was charged with catalyst (0.55 mL taken from a stock solution at 5.45 mM in THF, 3  $\mu\text{mol}$ ) and  $\beta$ -BL (49  $\mu\text{L}$ , 0.6 mmol). The reaction vessel was sealed and allowed to stir at room temperature. At predetermined reaction times, aliquots were withdrawn and quenched by addition into wet  $\text{CDCl}_3$ . The crude products were then characterised by NMR spectroscopy and GPC.

### **S2.3.4. Typical polymerization procedure ( $\epsilon$ -decalactone)**

In a glove box, a polymerization vessel was loaded with catalyst (0.5 mL taken from a stock solution of 6 mM in THF, 3  $\mu\text{mol}$ ) and  $\epsilon$ -DL (105  $\mu\text{L}$ , 0.6 mmol). The reaction vessel was sealed and allowed to stir at room temperature. At predetermined reaction times, aliquots were withdrawn and quenched by addition into wet  $\text{CDCl}_3$ . The crude products were then analysed by NMR spectroscopy and GPC.

### **S2.3.5. Typical polymerization procedure ( $\delta$ -hexaactone)**

In a glove box, a polymerization vessel was charged with catalyst (0.11 mL taken from a stock solution at 22.7 mM in THF, 2.5  $\mu\text{mol}$ ) and  $\delta$ -HL (0.14 mL, 1.25 mmol). The reaction vessel was sealed and allowed to stir at room temperature. At predetermined reaction times, aliquots were withdrawn and quenched by addition into wet  $\text{CDCl}_3$ . The crude products were then characterised by NMR spectroscopy and GPC.

## **S2.4. Polymer purification**

The crude polymer mixture was dissolved in  $\text{CHCl}_3$  (~5 mL) and dropwise added into a solution of methanol (~40 mL) to precipitate it. The polymer precipitate was filtered and dried. It was then dissolved in  $\text{CHCl}_3$  (~5 mL) and rapidly filtered through a small pad of silica. It was precipitated into methanol a further three times and finally dried in a 40 °C vacuum oven.

## S2.5. Determination of PLA tacticity

PLA tacticity was determined from its  $^1\text{H}\{^1\text{H}\}$  NMR spectrum (Figs. S72–S78). The spectra were deconvoluted using MestReNova v.11.0.2. The  $P_i$  values, the probability of isotactic enchainment, were calculated from each of tetrad integrals using Bernoulian statistical equations as shown below.<sup>11</sup>

$$[iii] = P_i^2 + P_iP_s/2 \quad (1)$$

$$[iis] = P_sP_i/2 \quad (2)$$

$$[sii] = P_sP_i/2 \quad (3)$$

$$[sis] = P_s^2/2 \quad (4)$$

$$[isi] = (P_s^2 + P_sP_i)/2 \quad (5)$$

## S2.6. Spectral characterization data for ligands $\text{H}_2\text{L}^1$ – $\text{H}_2\text{L}^4$

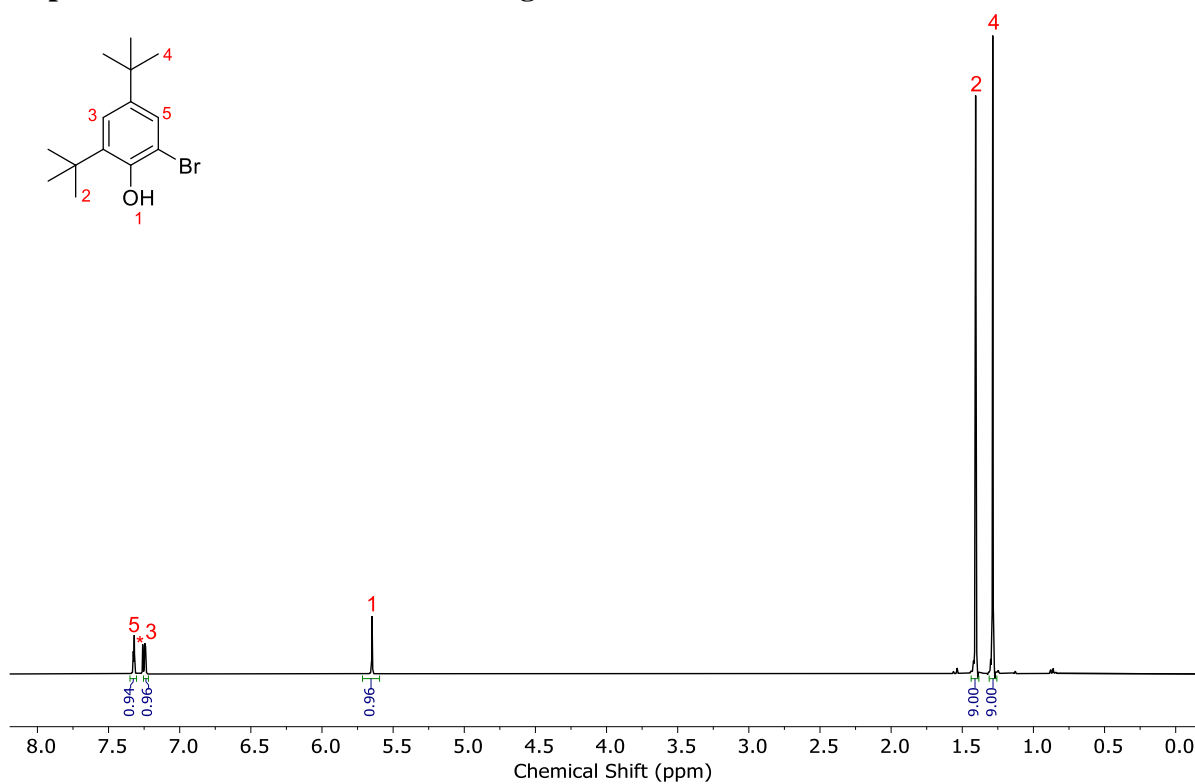


**Figure S1.**  $^1\text{H}$  NMR spectrum of compound **R1** in  $\text{CDCl}_3$ .

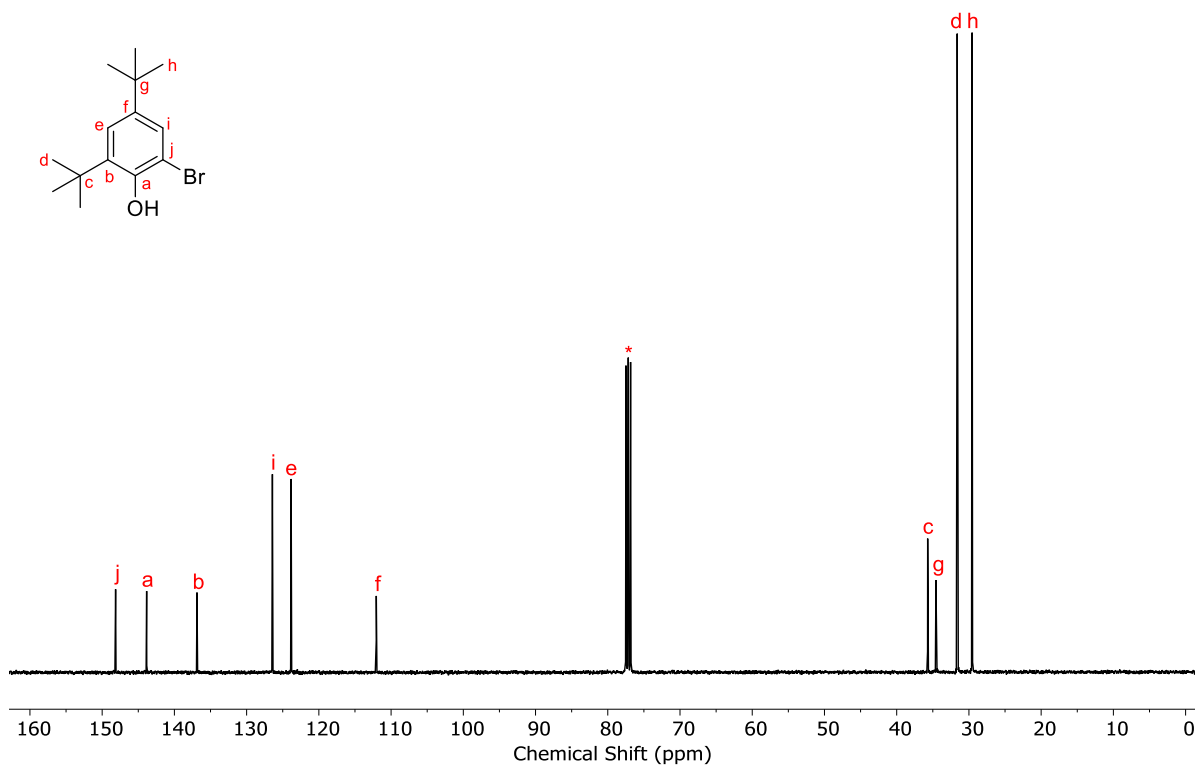


**Figure S2.**  $^{13}\text{C}\{^1\text{H}\}$  NMR spectrum of compound **R1** in  $\text{CDCl}_3$ .

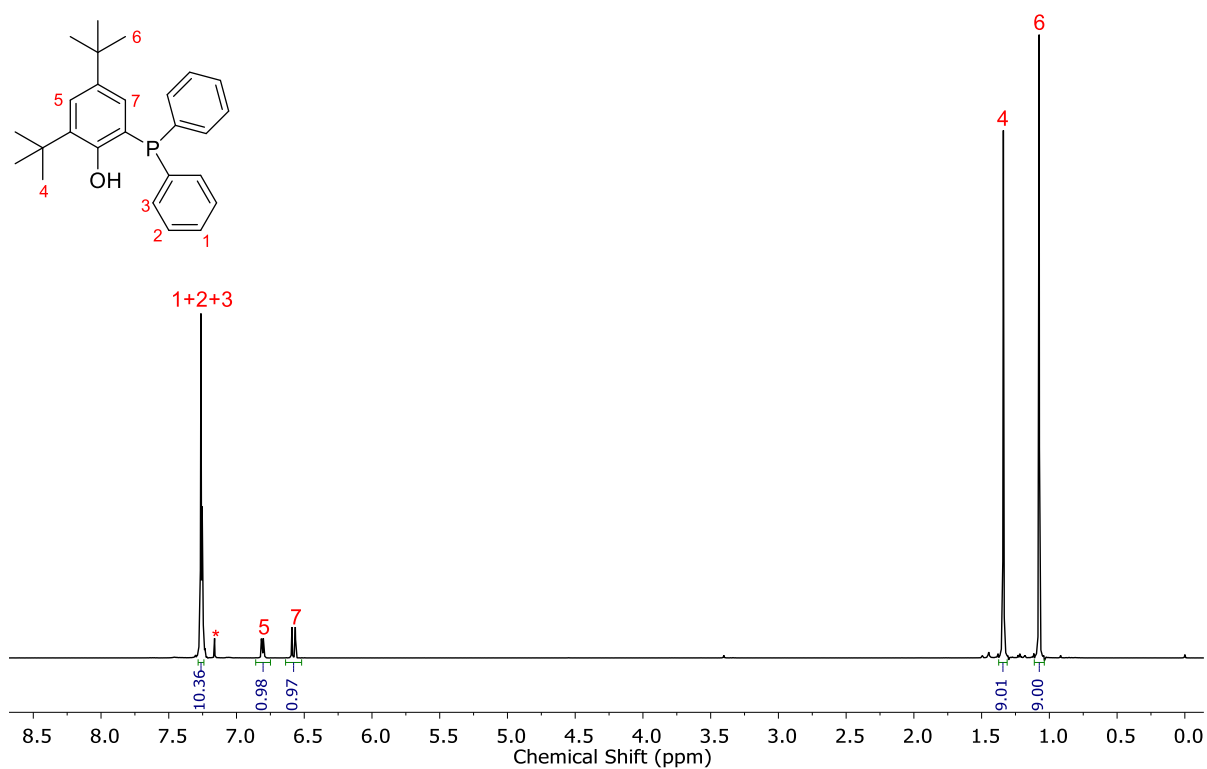


**Figure S3.**  $^1\text{H}$  NMR spectrum of compound **R2** in  $\text{CDCl}_3$ .

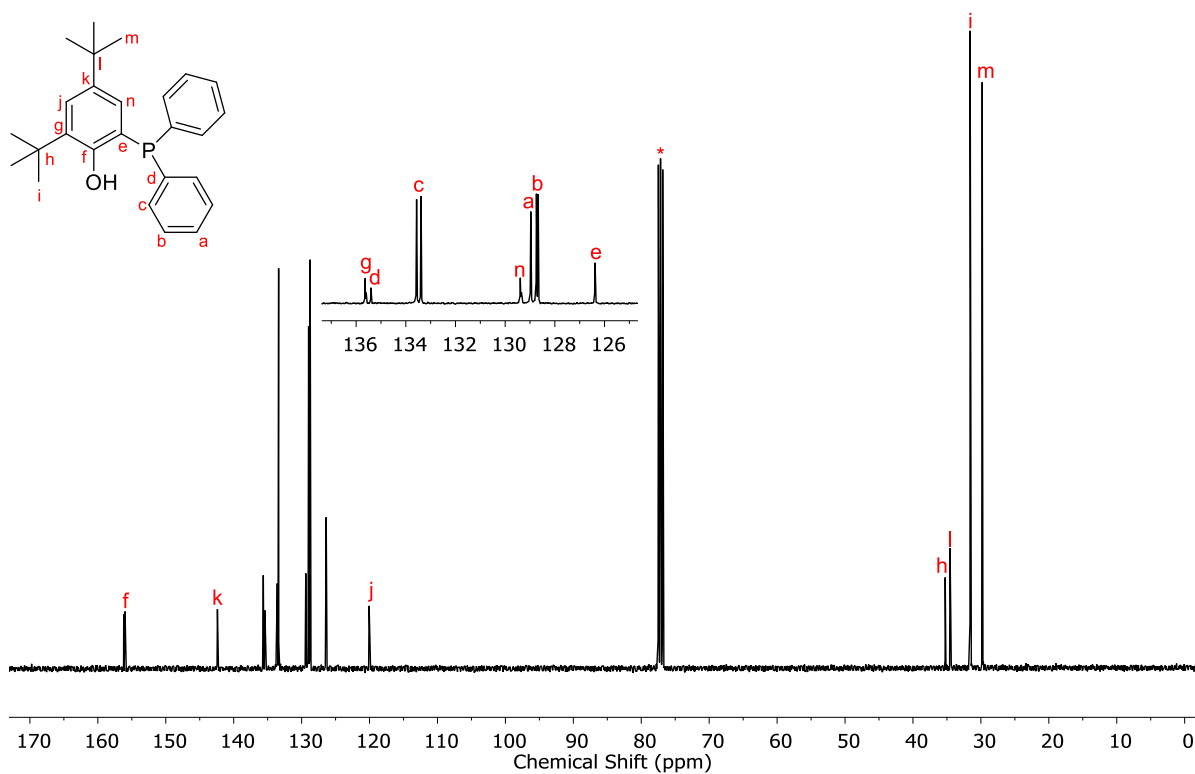


**Figure S4.**  $^{13}\text{C}\{^1\text{H}\}$  NMR spectrum of compound **R2** in  $\text{CDCl}_3$ .

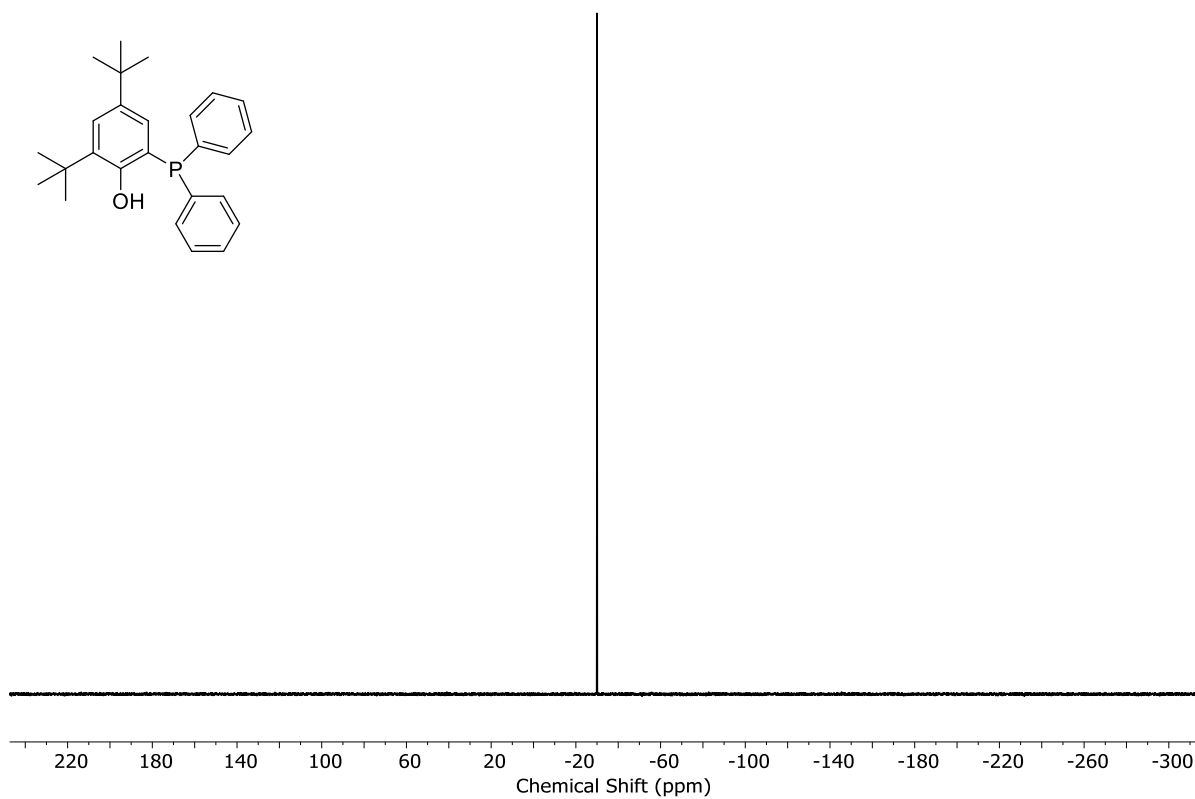


**Figure S5.**  $^{31}\text{P}\{^1\text{H}\}$  NMR spectrum of compound **R2** in  $\text{CDCl}_3$ .

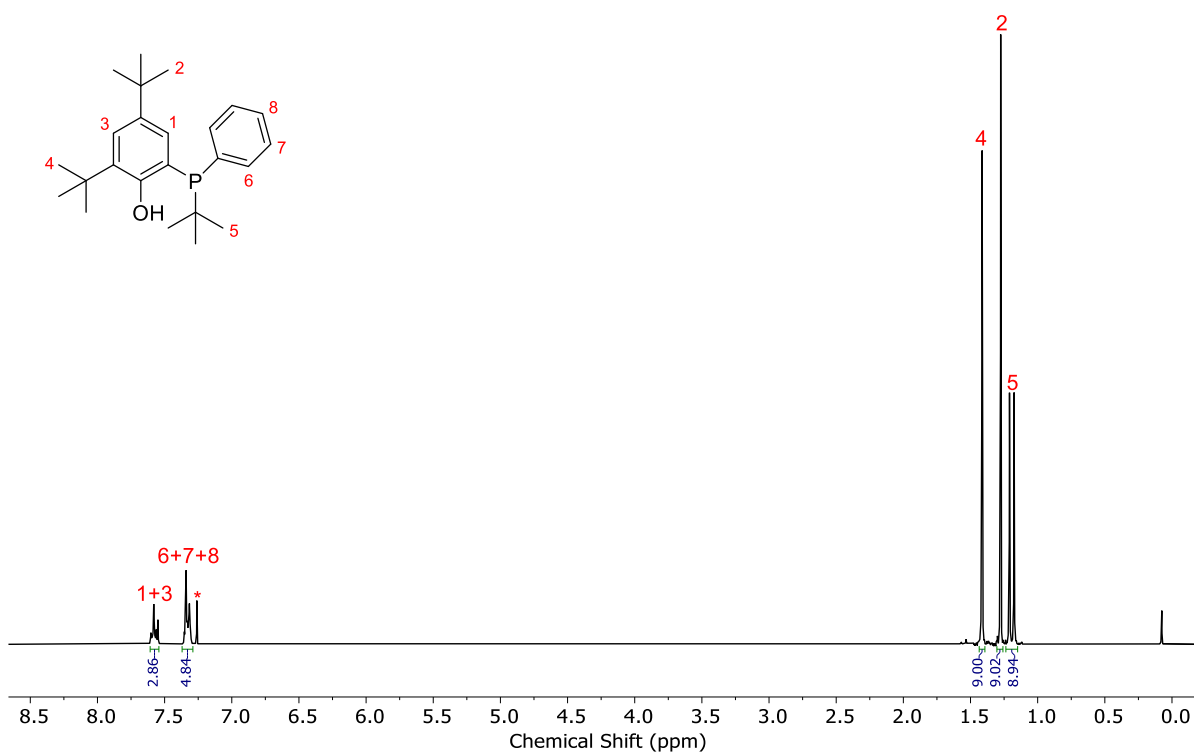


**Figure S6.**  $^1\text{H}$  NMR spectrum of compound **R3** in  $\text{CDCl}_3$ .

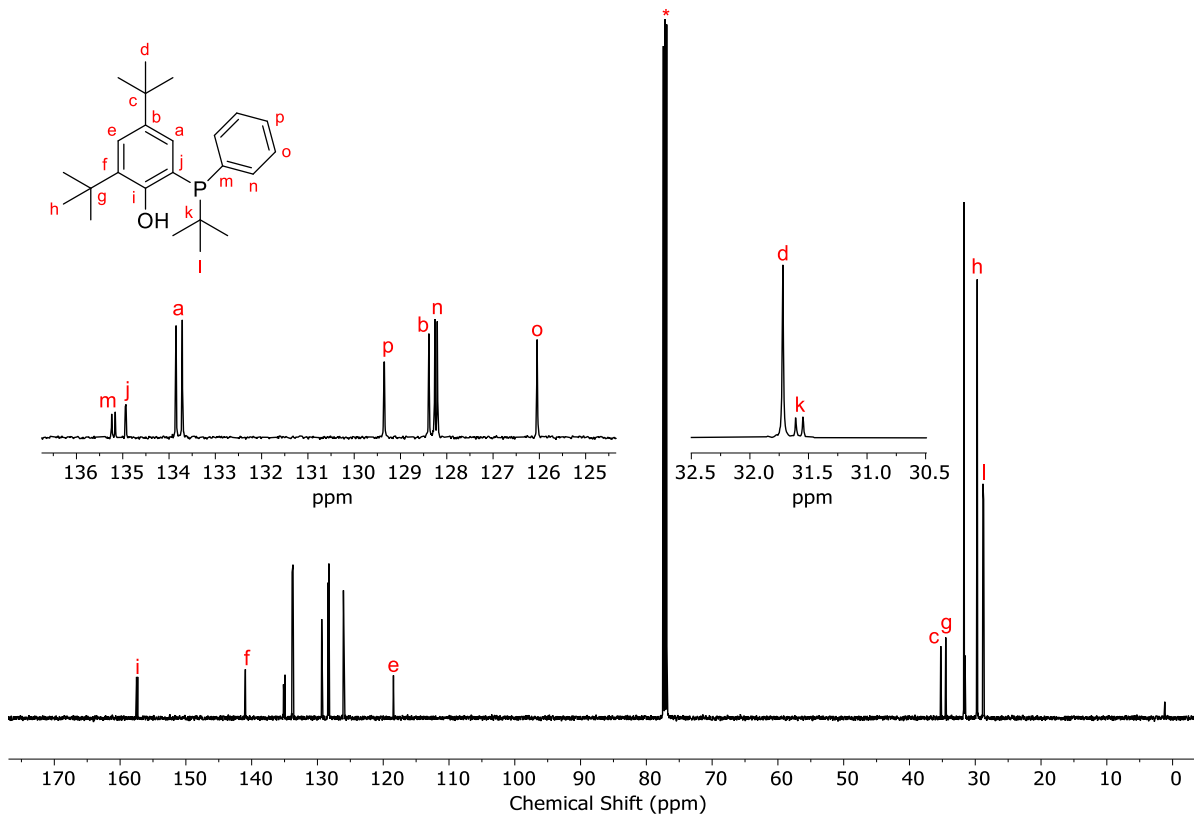


**Figure S7.**  $^{13}\text{C}\{^1\text{H}\}$  NMR spectrum of compound **R3** in  $\text{CDCl}_3$ .

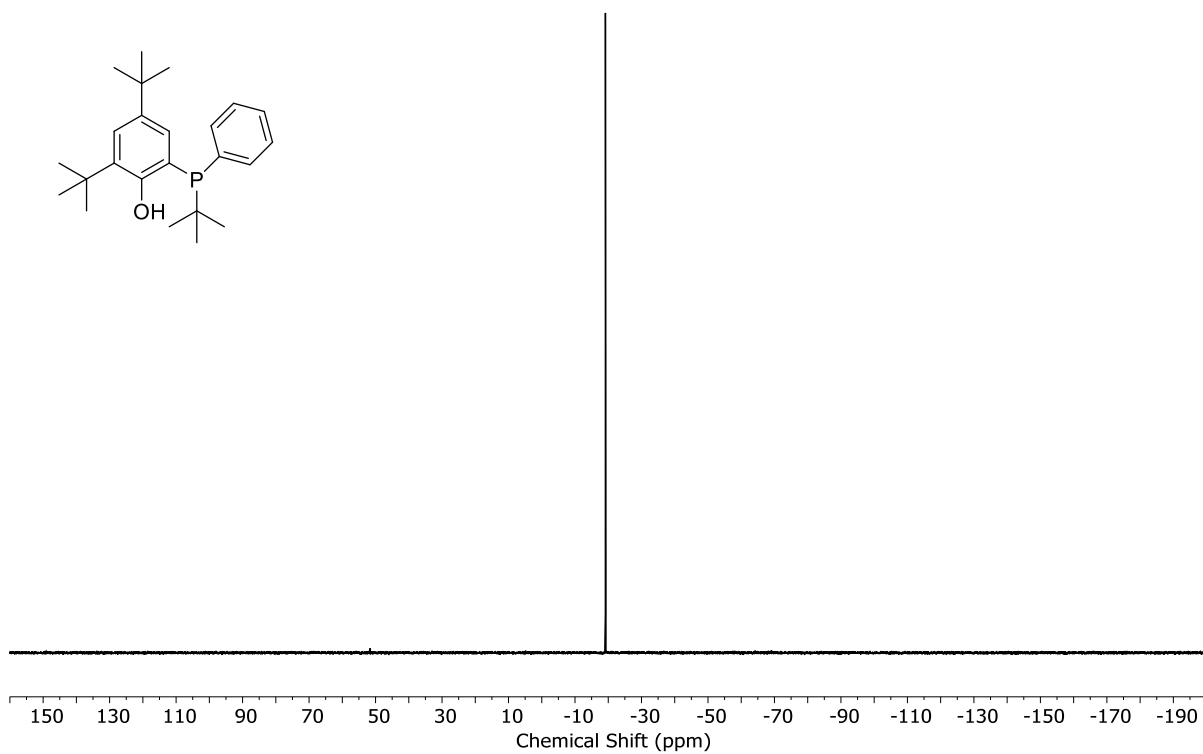


**Figure S8.**  $^{31}\text{P}\{^1\text{H}\}$  NMR spectrum of compound **R3** in  $\text{CDCl}_3$ .

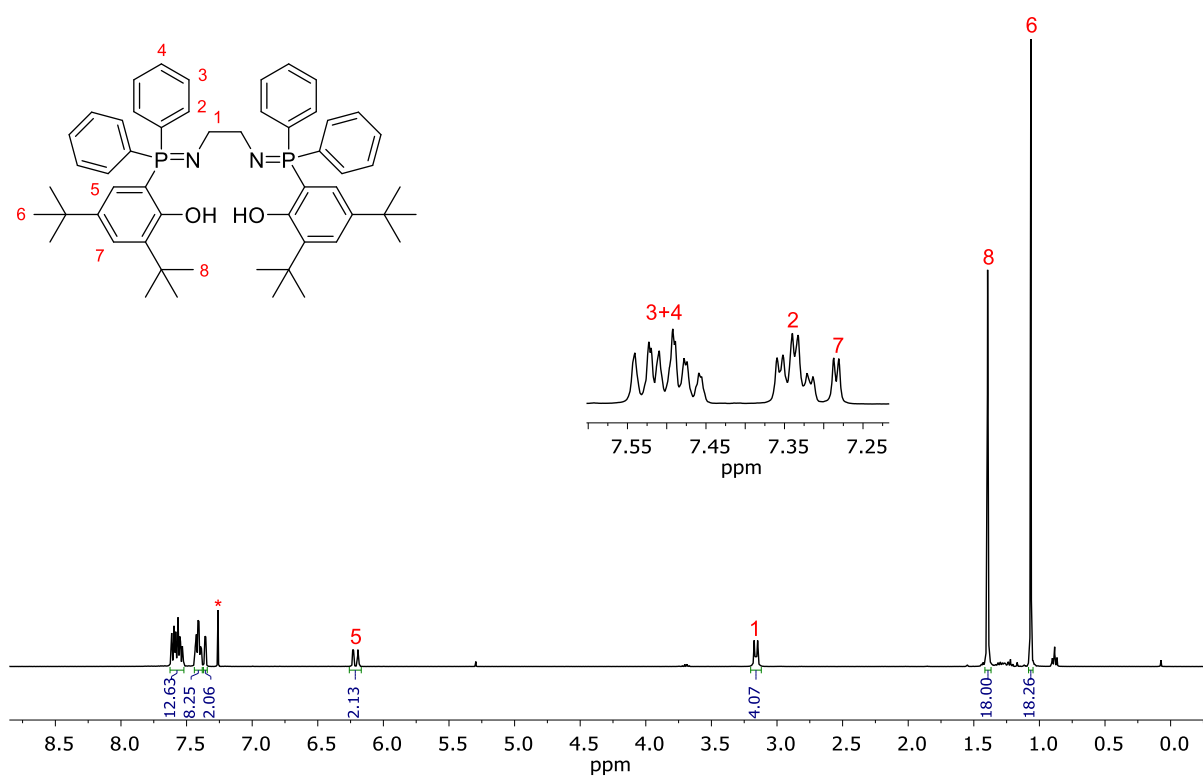


**Figure S9.**  $^1\text{H}$  NMR spectrum of ligand **H<sub>2</sub>L<sup>1</sup>** in  $\text{CDCl}_3$

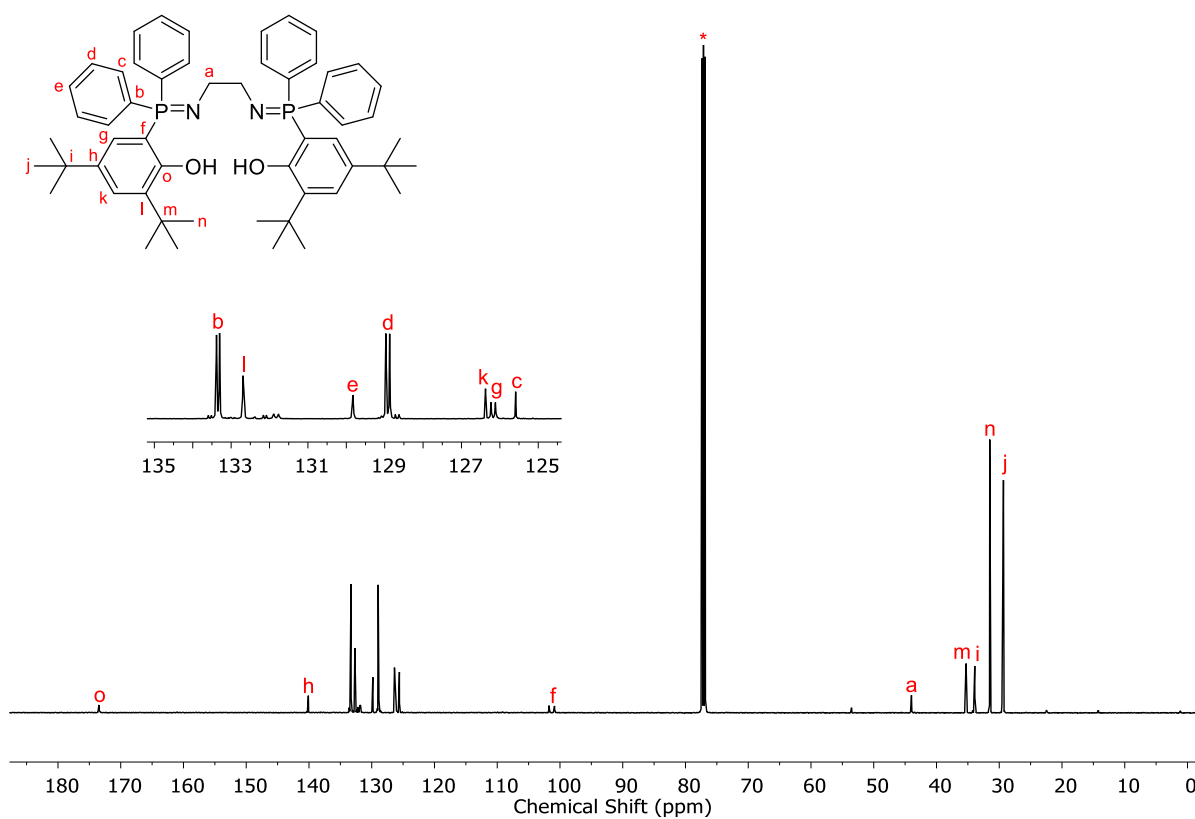


**Figure S10.**  $^{13}\text{C}\{^1\text{H}\}$  NMR spectrum of ligand  $\text{H}_2\text{L}^1$  in  $\text{CDCl}_3$ .

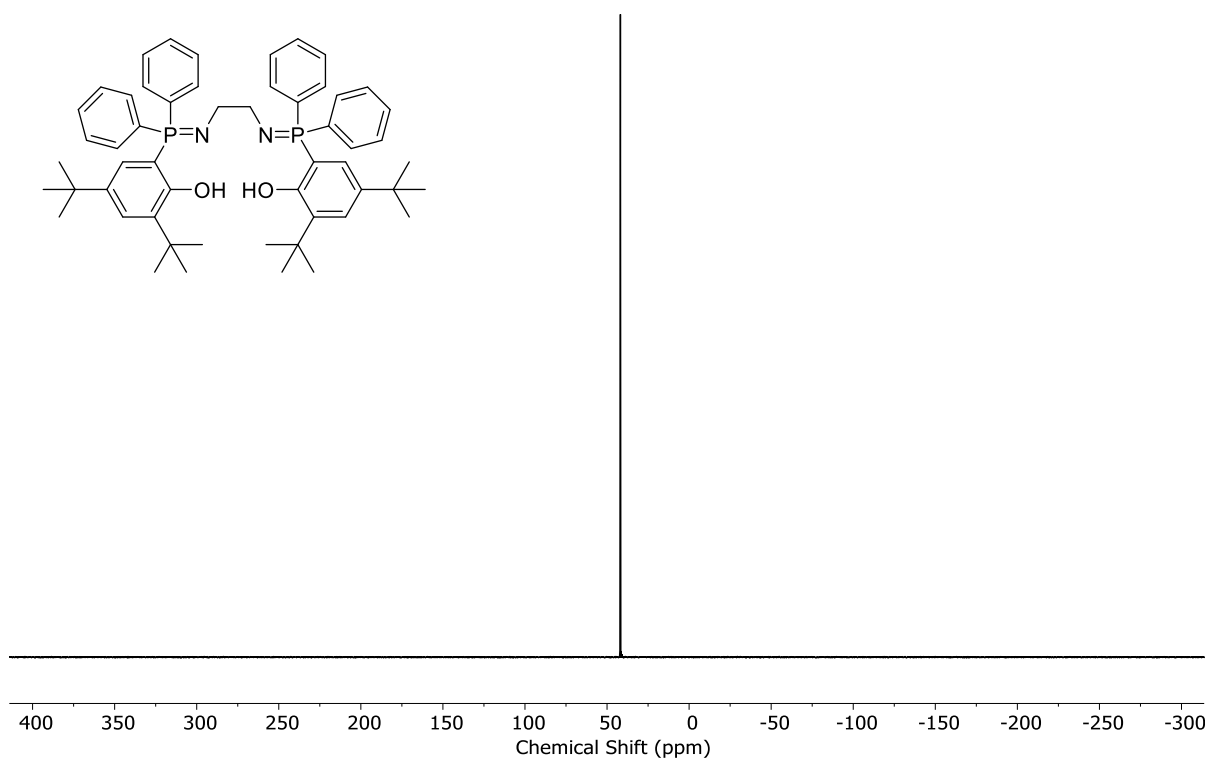


**Figure S11.**  $^{31}\text{P}\{^1\text{H}\}$  NMR spectrum of ligand  $\text{H}_2\text{L}^1$  in  $\text{CDCl}_3$ .

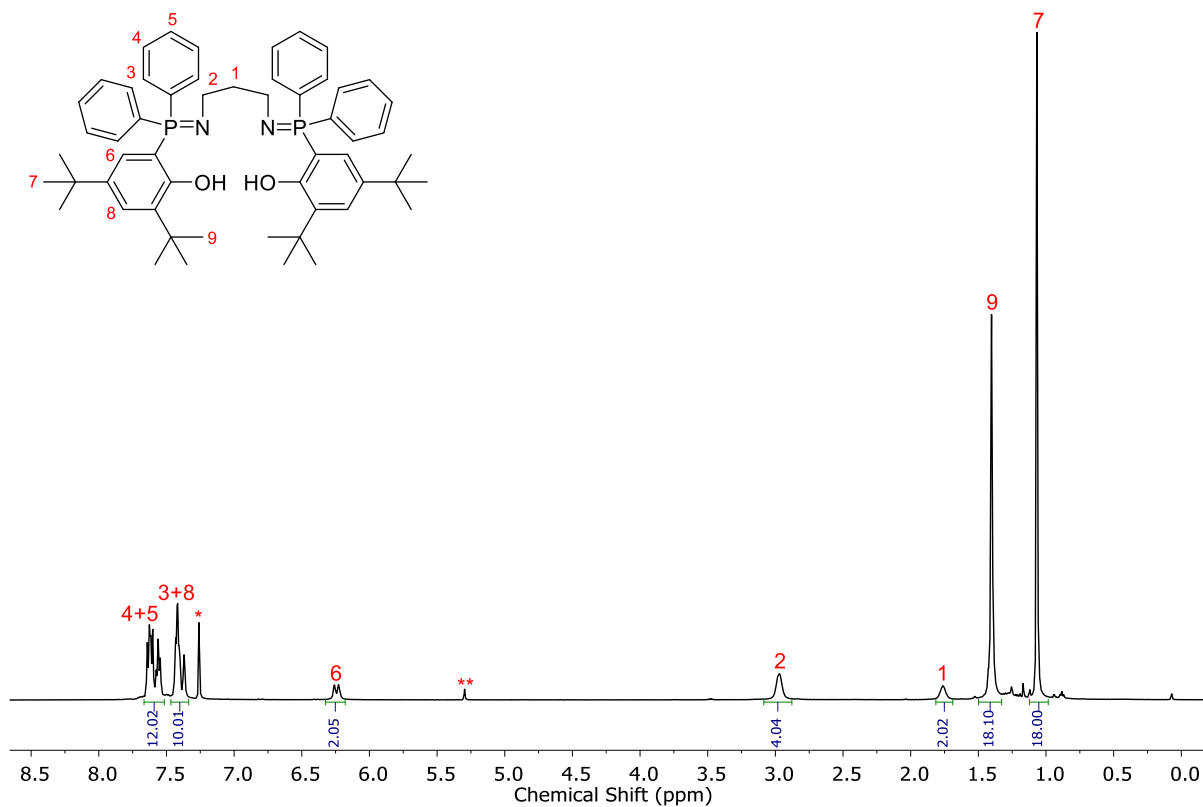


**Figure S12.**  $^1\text{H}$  NMR spectrum of ligand  $\text{H}_2\text{L}^2$  in  $\text{CDCl}_3$ .

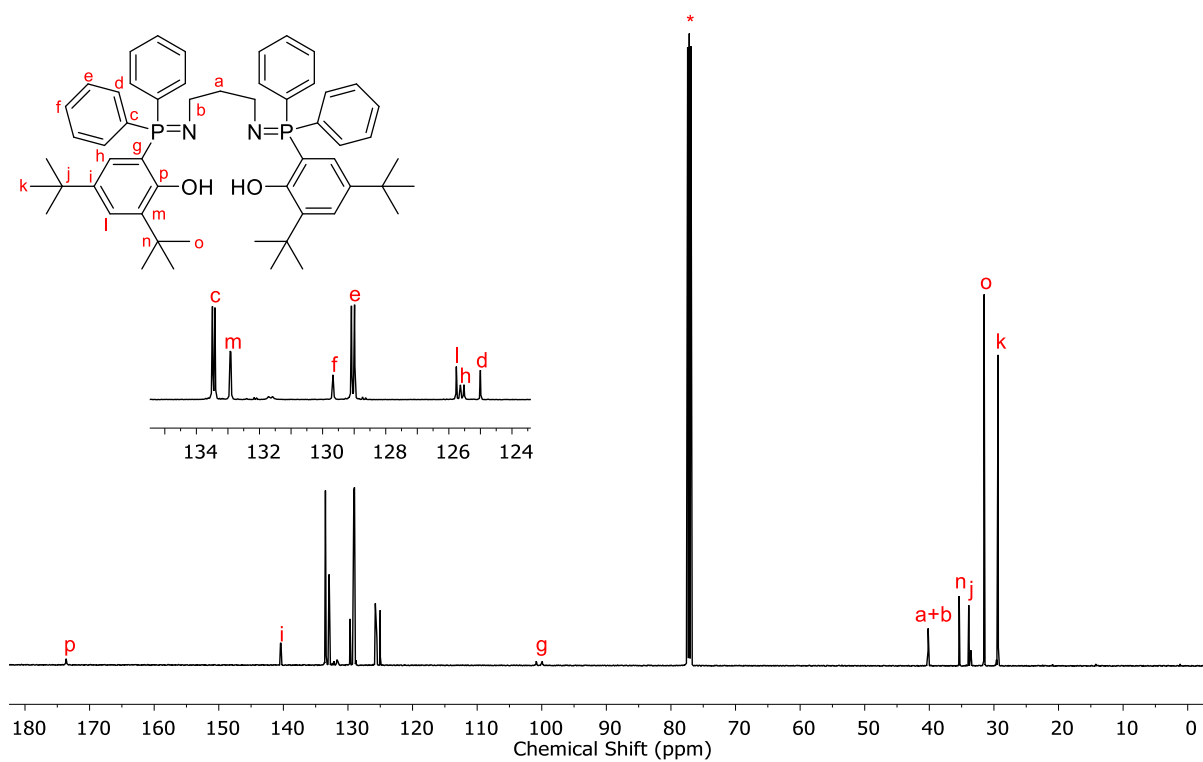


**Figure S13.**  $^{13}\text{C}\{^1\text{H}\}$  NMR spectrum of ligand  $\text{H}_2\text{L}^2$  in  $\text{CDCl}_3$ .

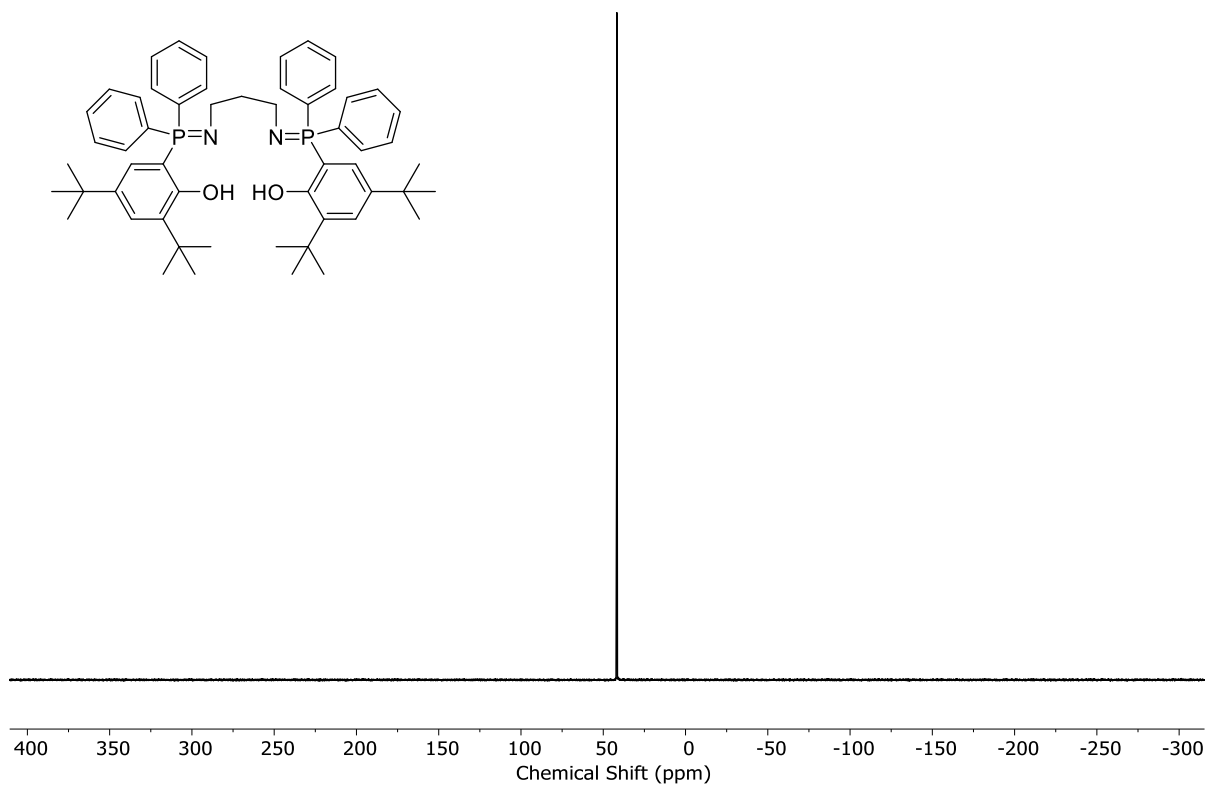


**Figure S14.**  $^{31}\text{P}\{^1\text{H}\}$  NMR spectrum of ligand  $\text{H}_2\text{L}^2$  in  $\text{CDCl}_3$ .

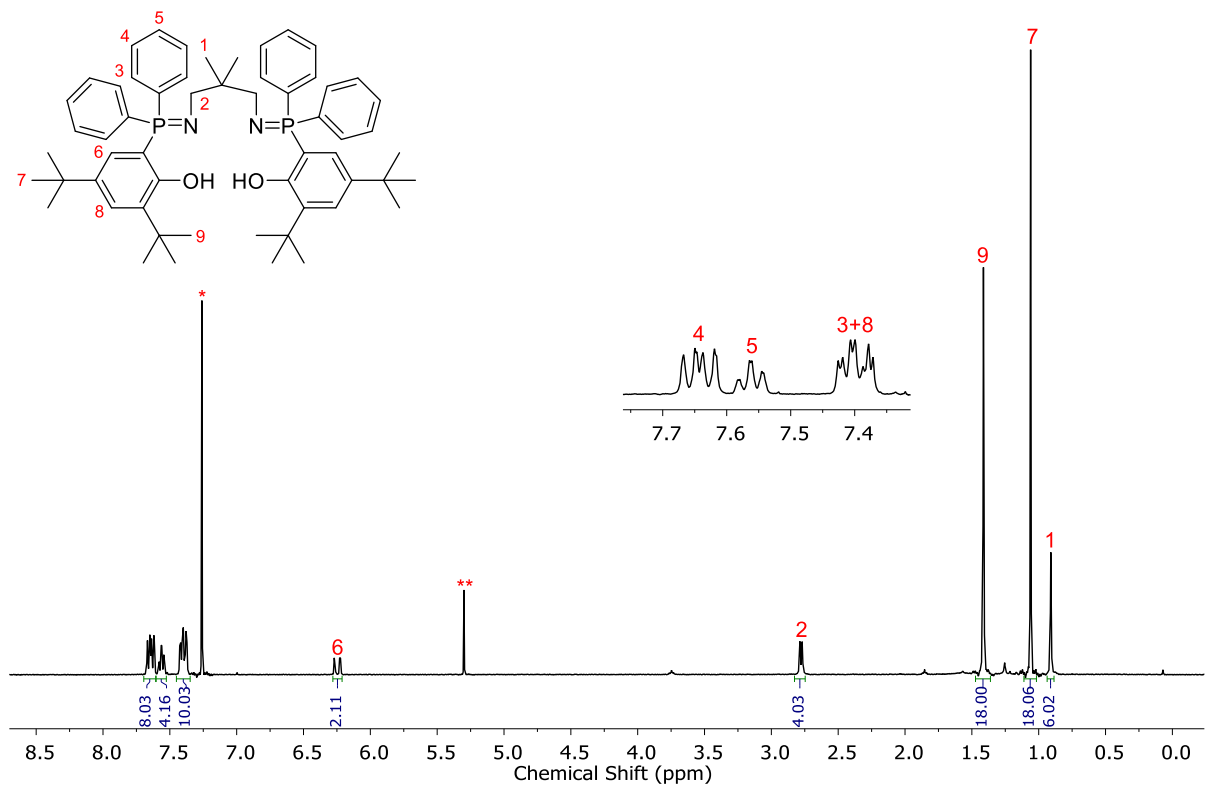


**Figure S15.**  $^1\text{H}$  NMR spectrum of ligand  $\text{H}_2\text{L}^3$  in  $\text{CDCl}_3$ .

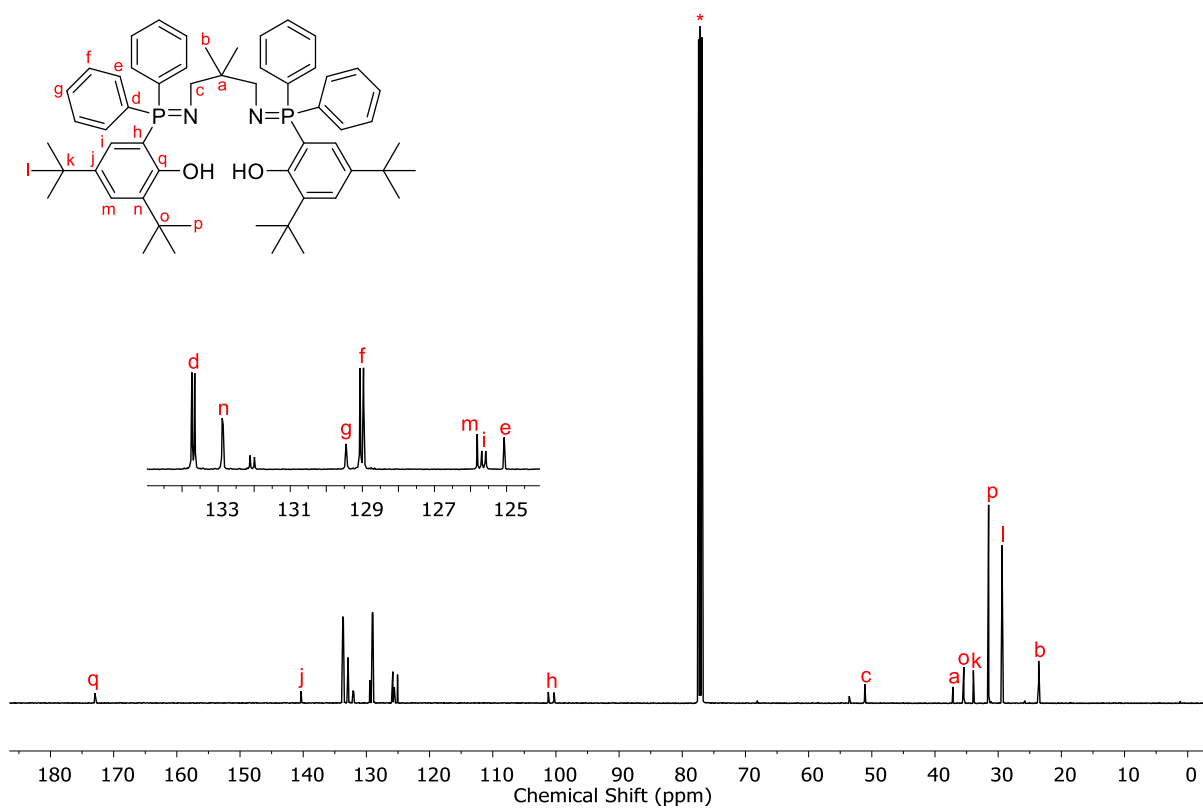


**Figure S16.**  $^{13}\text{C}\{^1\text{H}\}$  NMR spectrum of ligand  $\text{H}_2\text{L}^3$  in  $\text{CDCl}_3$ .

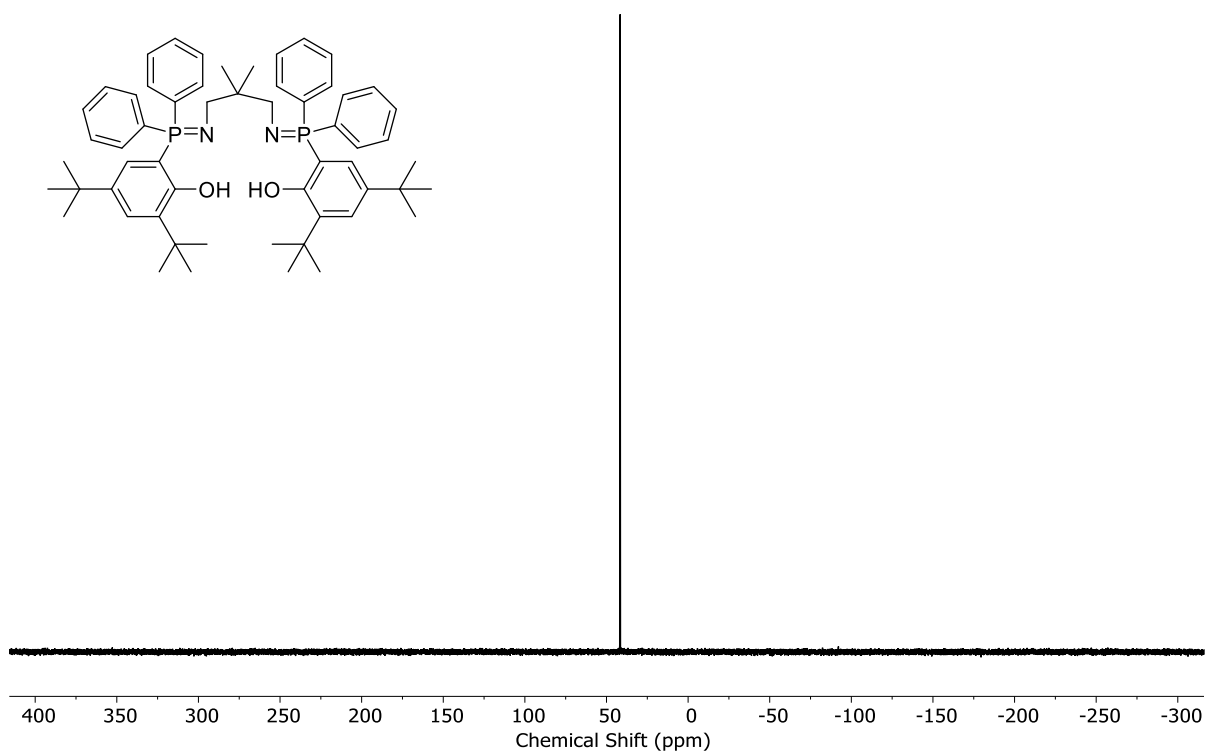


**Figure S17.**  $^{31}\text{P}\{^1\text{H}\}$  NMR spectrum of ligand  $\text{H}_2\text{L}^3$  in  $\text{CDCl}_3$ .

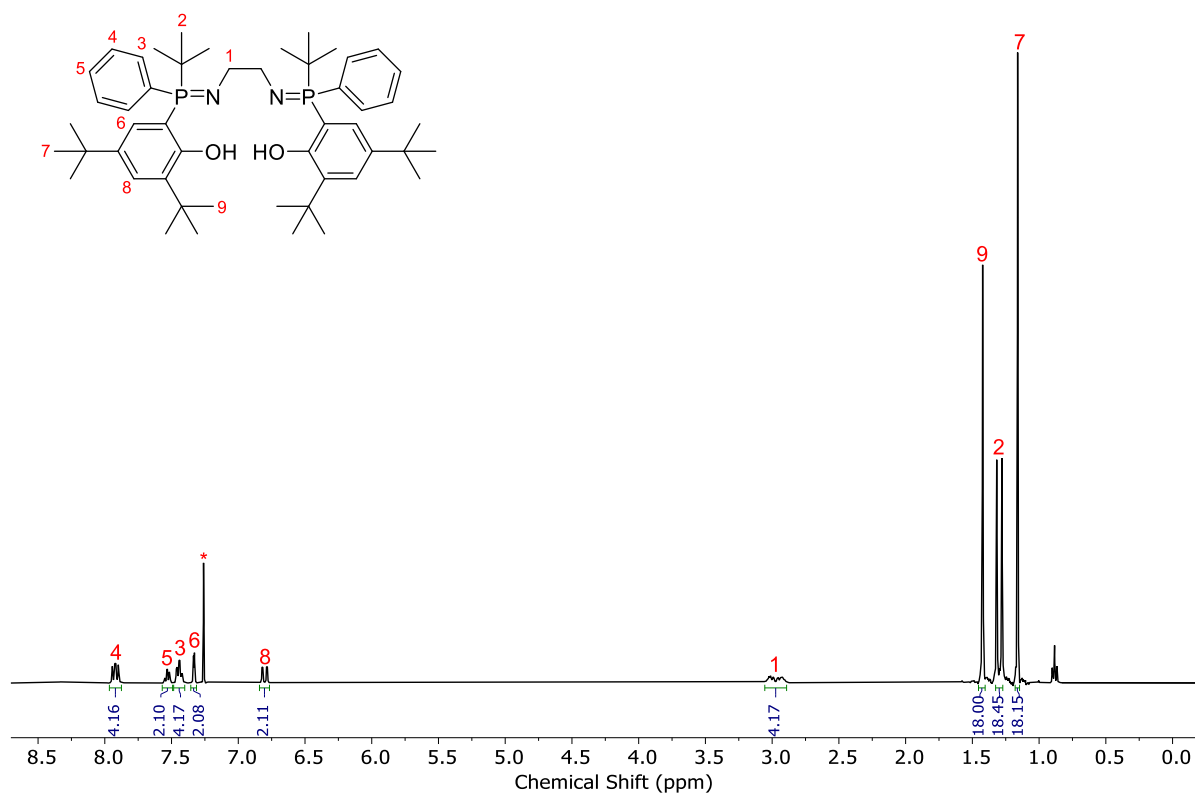


**Figure S18.** <sup>1</sup>H NMR spectrum of ligand **H<sub>2</sub>L<sup>4</sup>** in CDCl<sub>3</sub>.

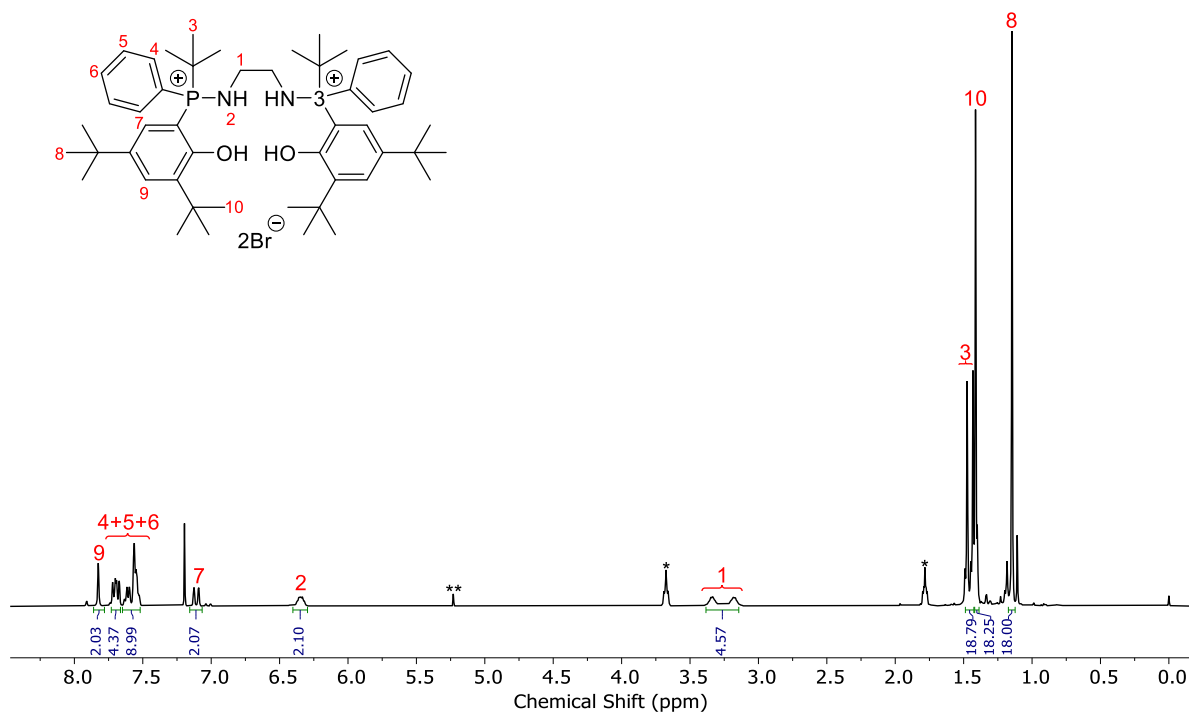


**Figure S19.** <sup>1</sup>H NMR spectrum of ligand **H<sub>2</sub>L<sup>4</sup>** in CDCl<sub>3</sub> (prior to purification by column chromatography).

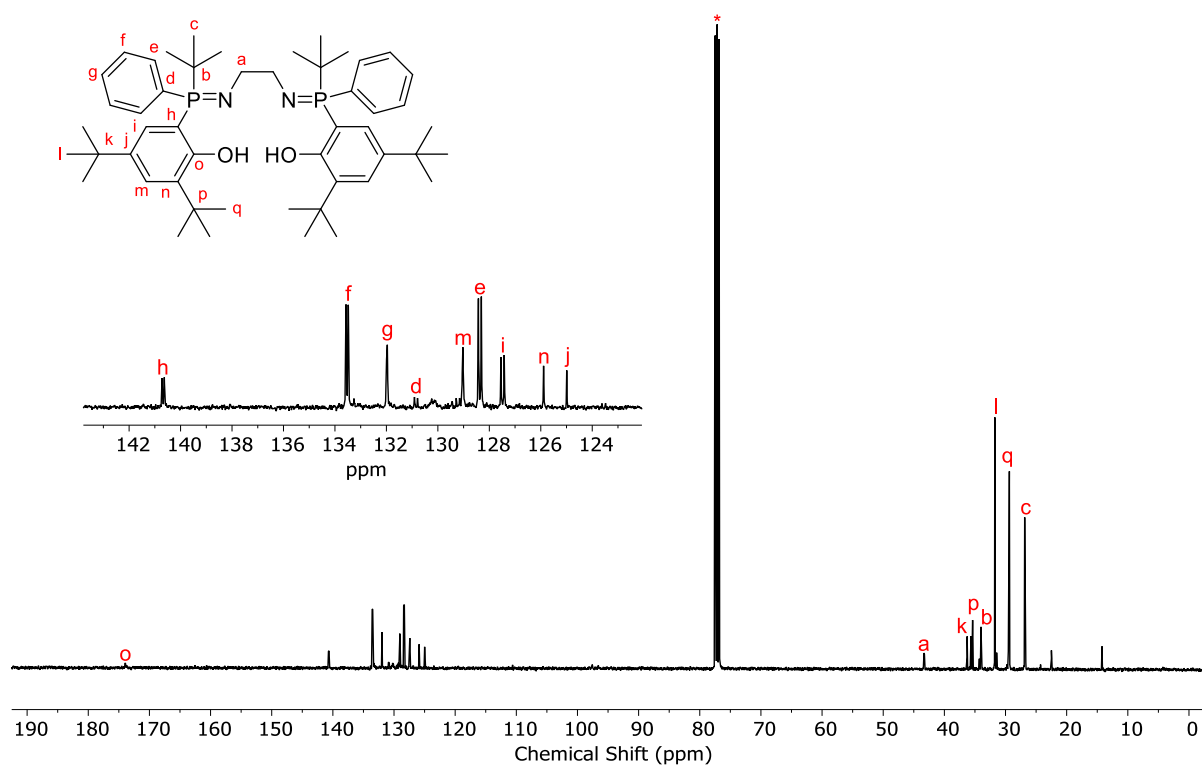


**Figure S20.**  $^{13}\text{C}\{^1\text{H}\}$  NMR spectrum of ligand  $\text{H}_2\text{L}^4$  in  $\text{CDCl}_3$ .

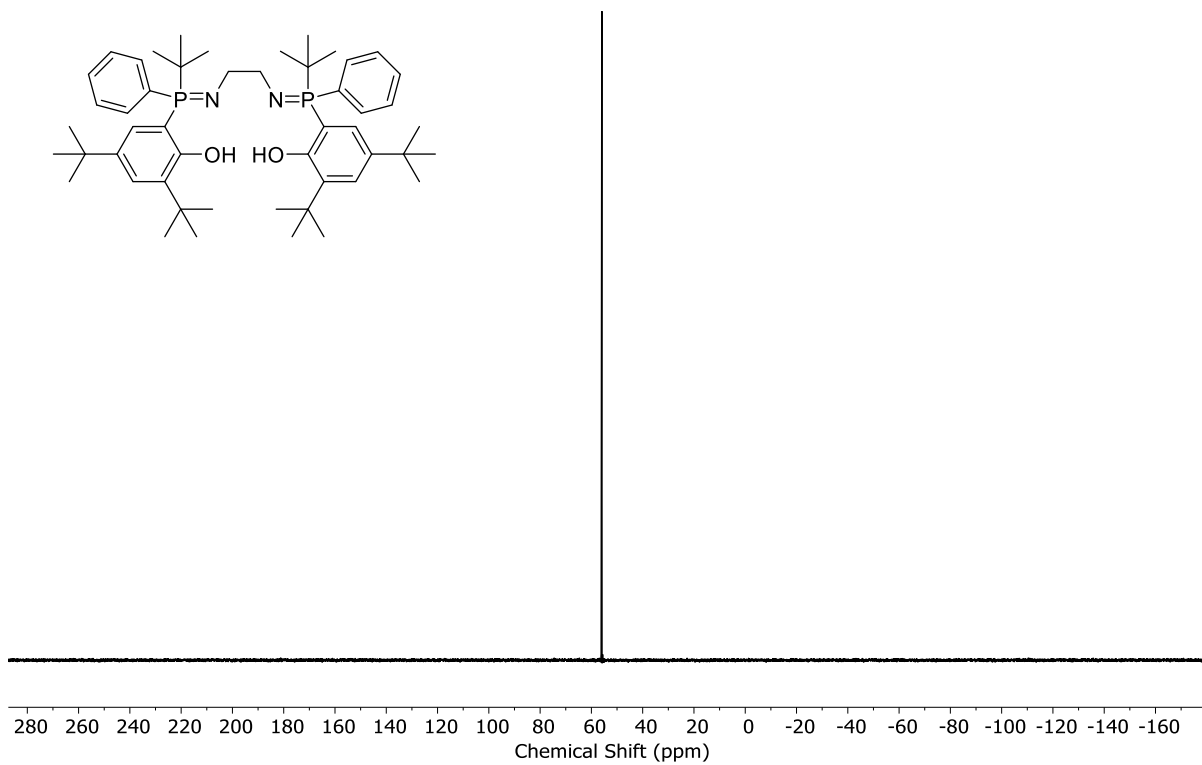


**Figure S21.**  $^{31}\text{P}\{^1\text{H}\}$  NMR spectrum of ligand  $\text{H}_2\text{L}^4$  in  $\text{CDCl}_3$ .

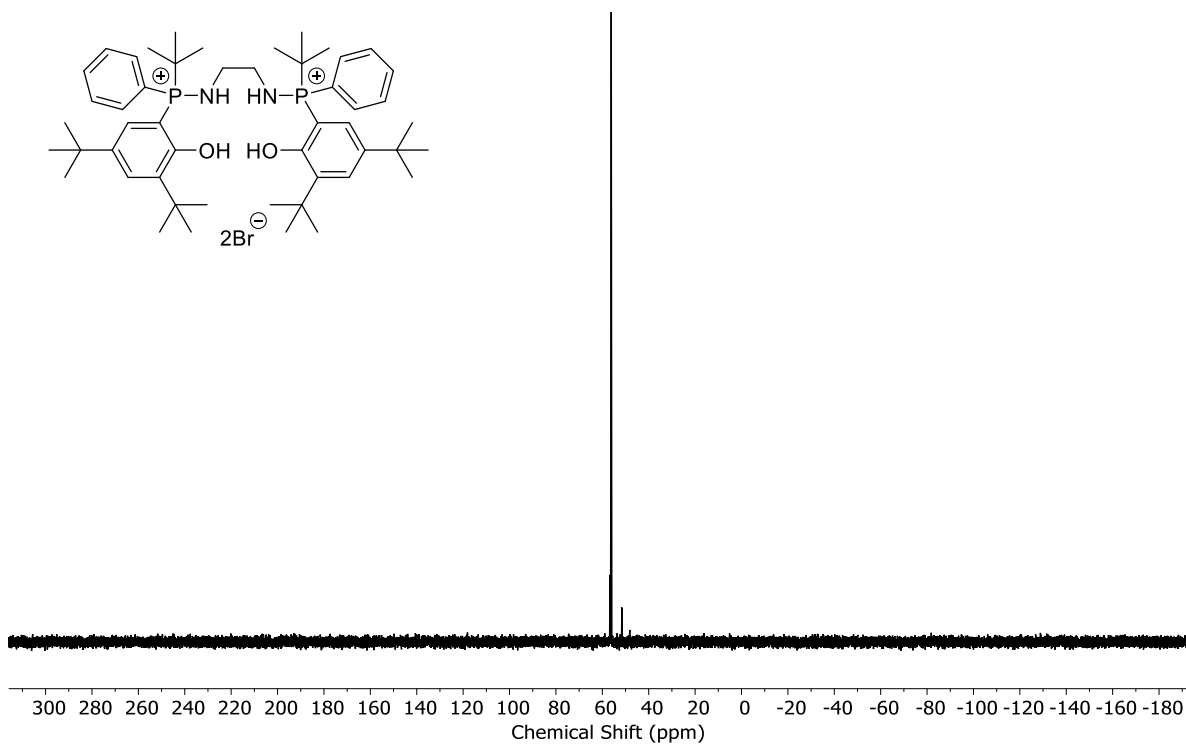


**Figure S22.**  $^{31}\text{P}\{^1\text{H}\}$  NMR spectrum of ligand  $\text{H}_2\text{L}^4$  in  $\text{CDCl}_3$  (prior to purification by column chromatography).

### S2.7. Spectral characterization data of indium complexes 1–5

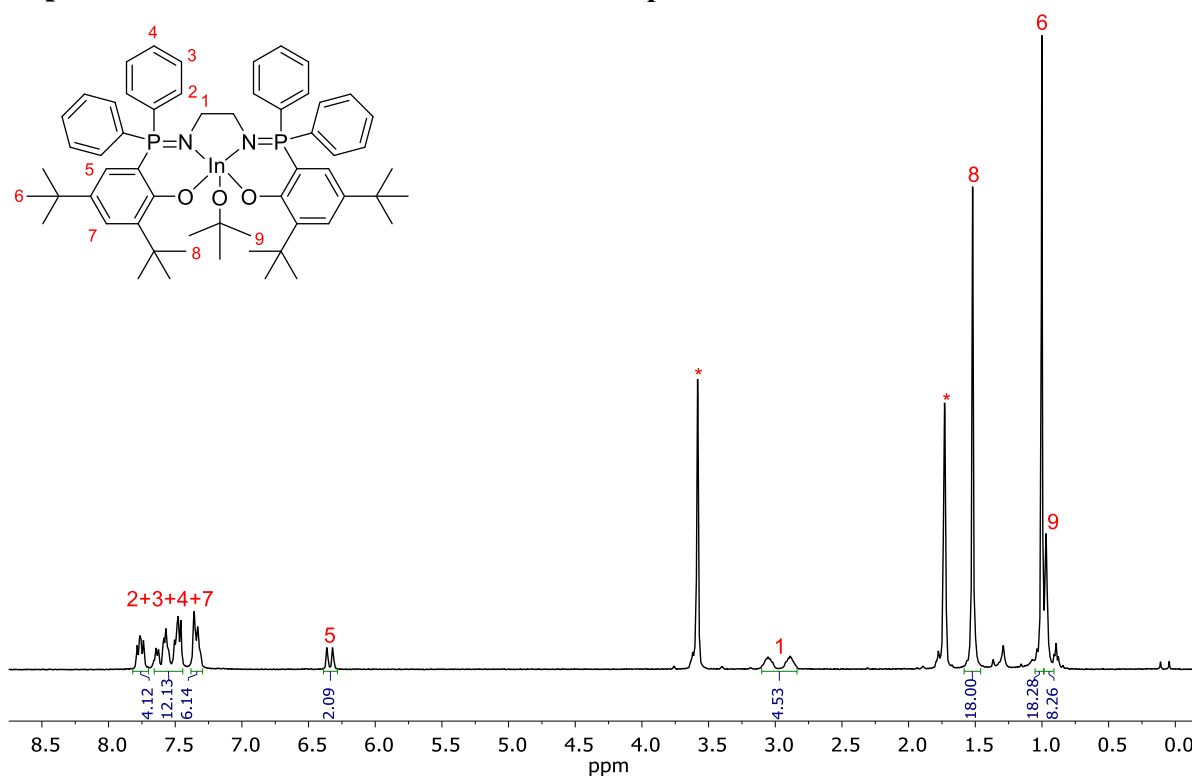


**Figure S23.**  $^1\text{H}$  NMR spectrum of complex **1** in  $\text{THF-}d_8$ .

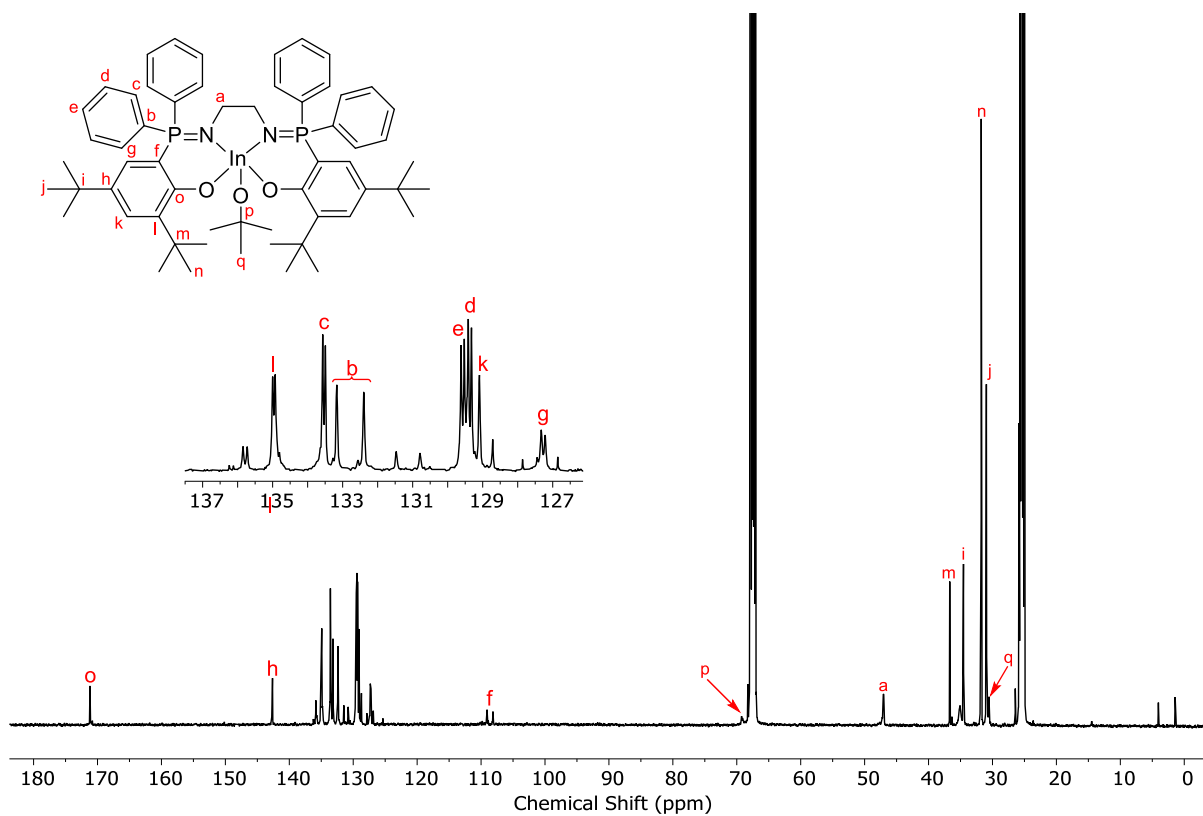


**Figure S24.**  $^{13}\text{C}\{^1\text{H}\}$  NMR spectrum of complex **1** in  $\text{THF-}d_8$ .

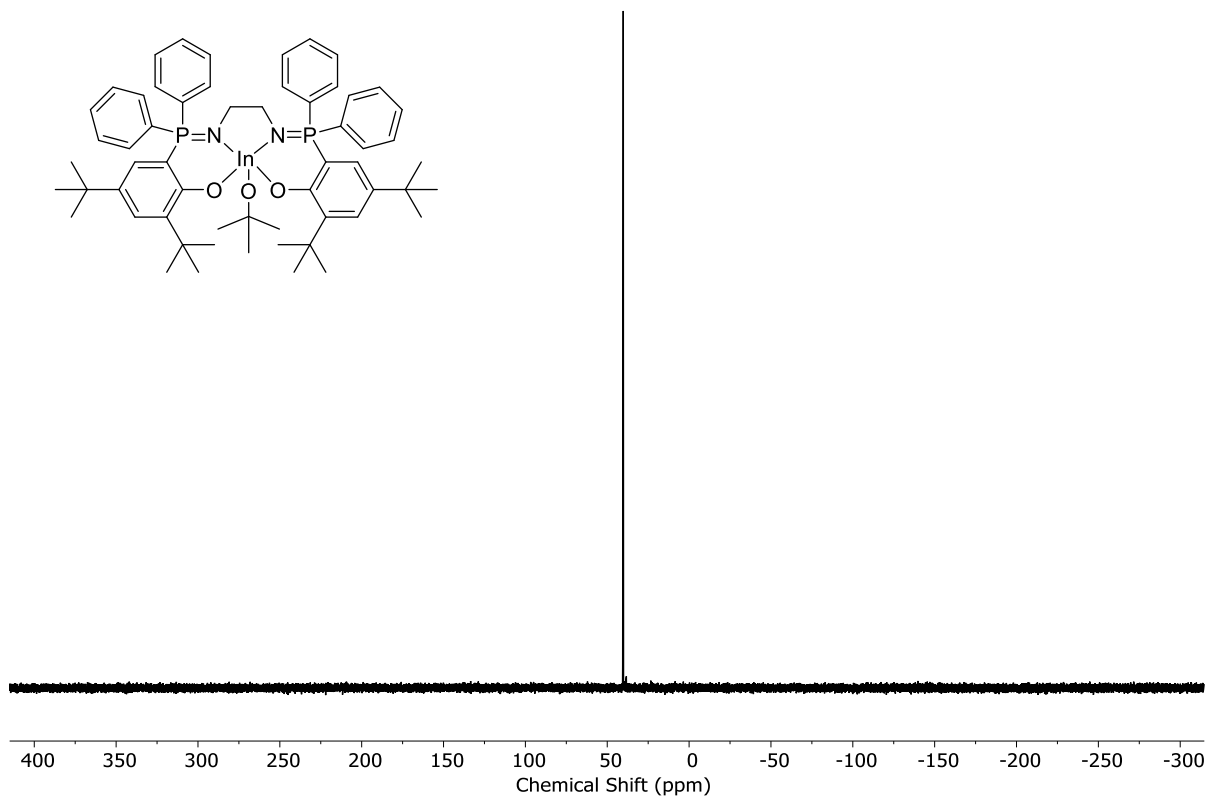


**Figure S25.**  $^{31}\text{P}\{^1\text{H}\}$  NMR spectrum of complex **1** in  $\text{THF-}d_8$ .

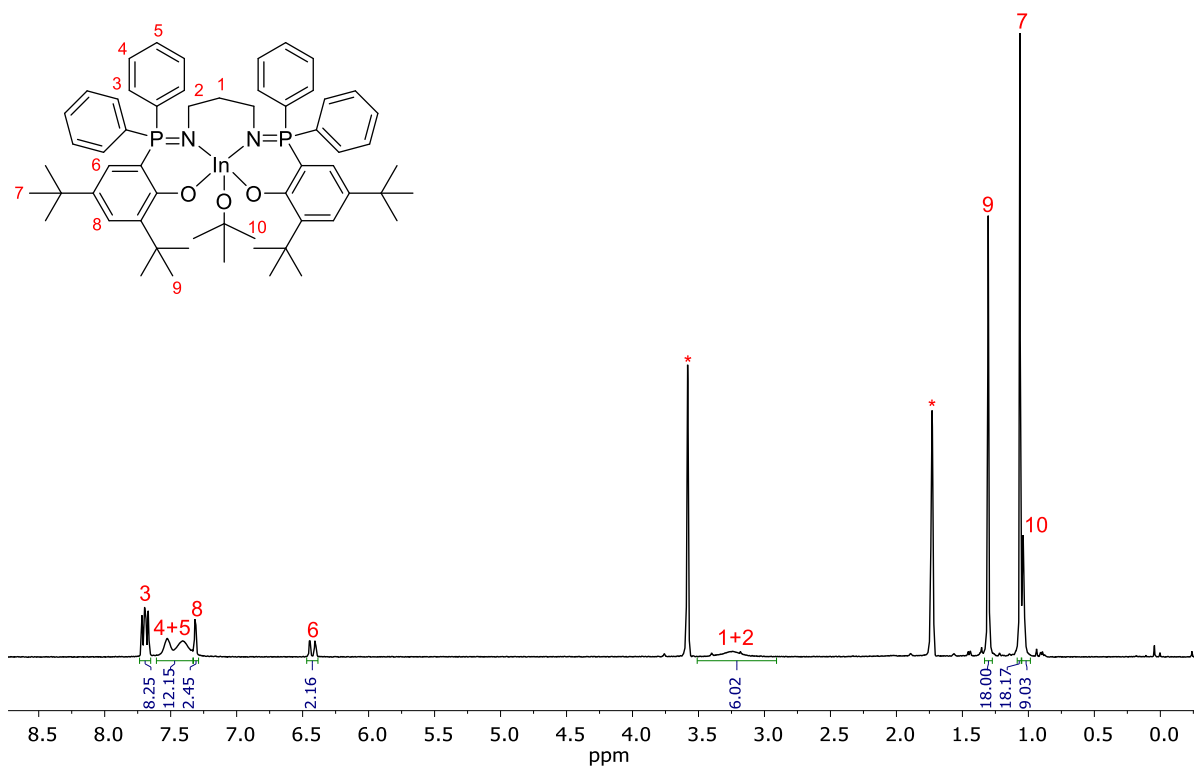


**Figure S26.**  $^1\text{H}$  NMR spectrum of complex **2** in  $\text{THF-}d_8$ .

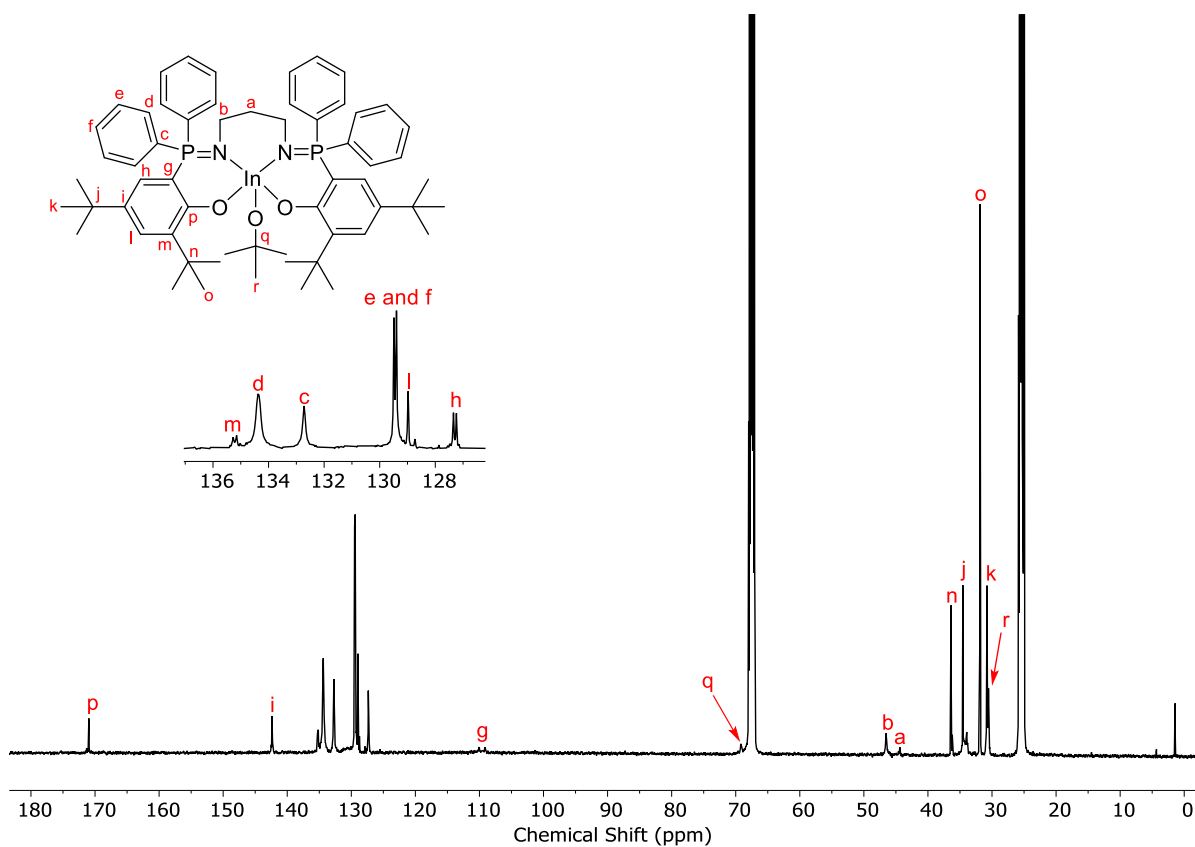


**Figure S27.**  $^{13}\text{C}\{^1\text{H}\}$  NMR spectrum of complex **2** in  $\text{THF-}d_8$ .

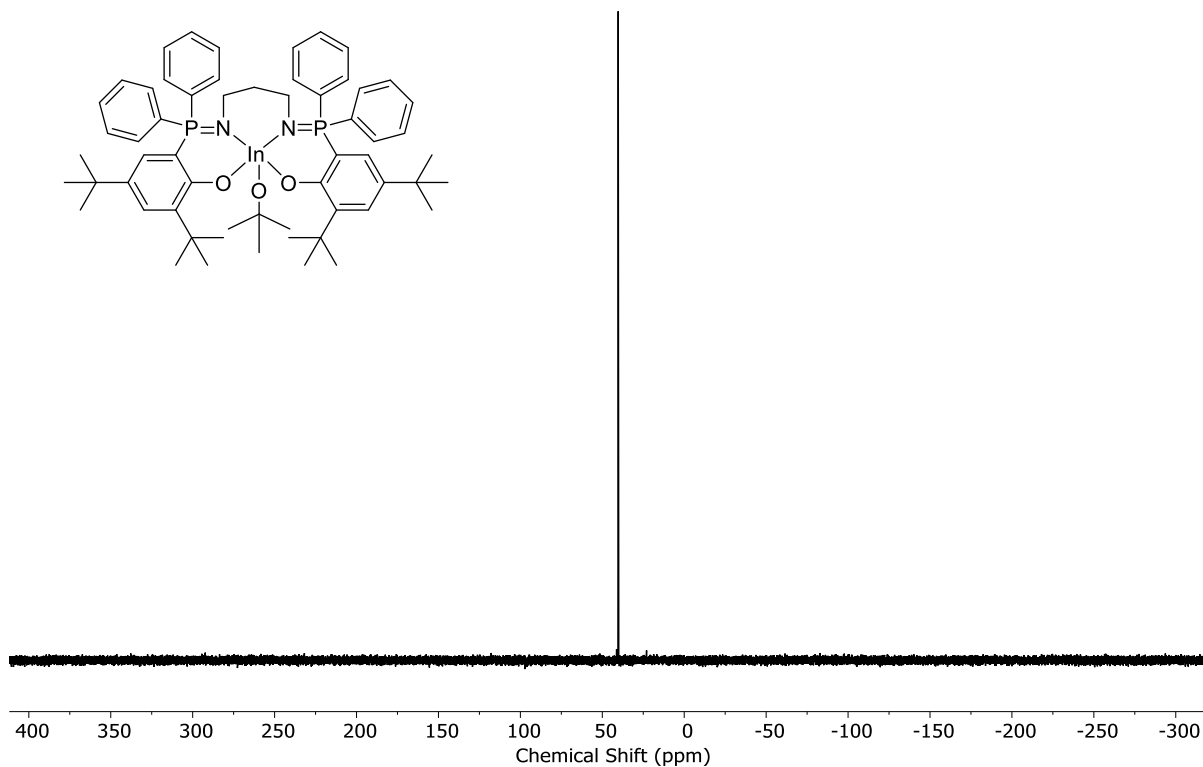


**Figure S28.**  $^{31}\text{P}\{^1\text{H}\}$  NMR spectrum of complex **2** in  $\text{THF-}d_8$ .

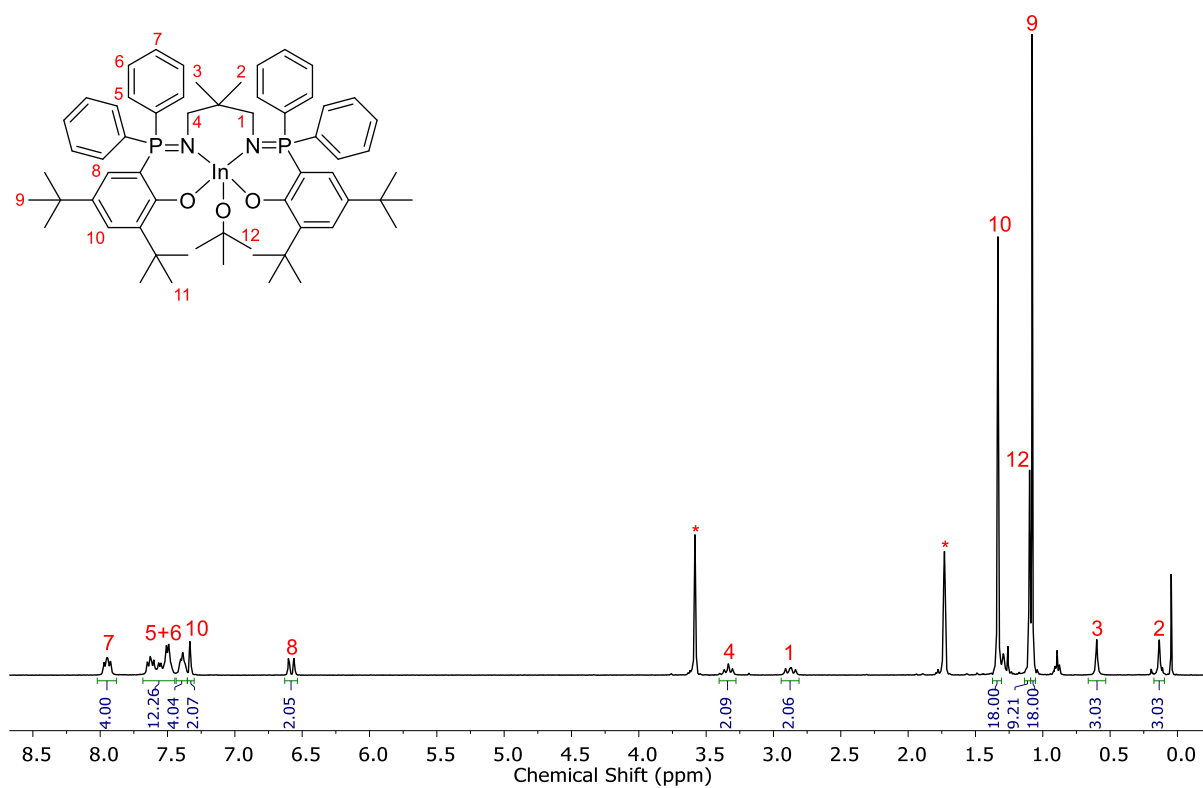


**Figure S29.**  $^1\text{H}$  NMR spectrum of complex **3** in  $\text{THF-}d_8$ .

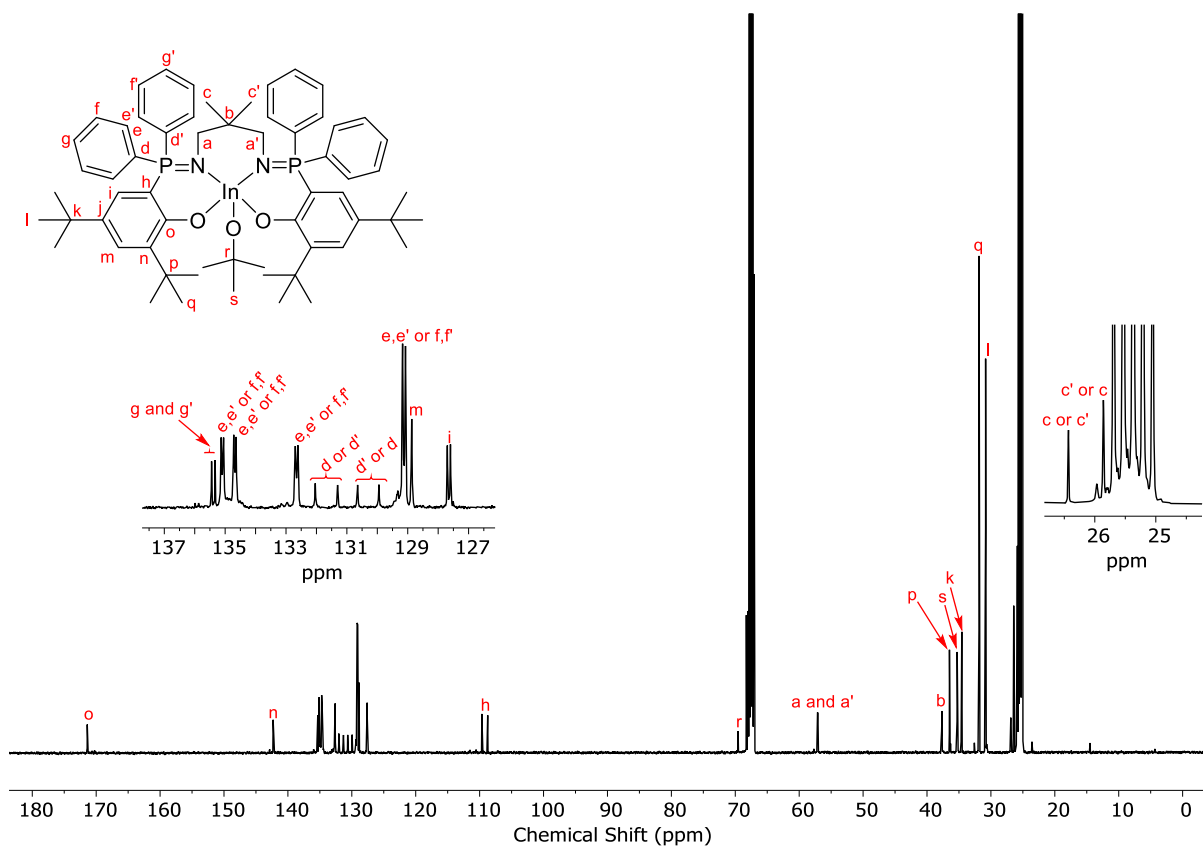


**Figure S30.**  $^{13}\text{C}\{^1\text{H}\}$  NMR spectrum of complex 3 in  $\text{THF-}d_8$ .

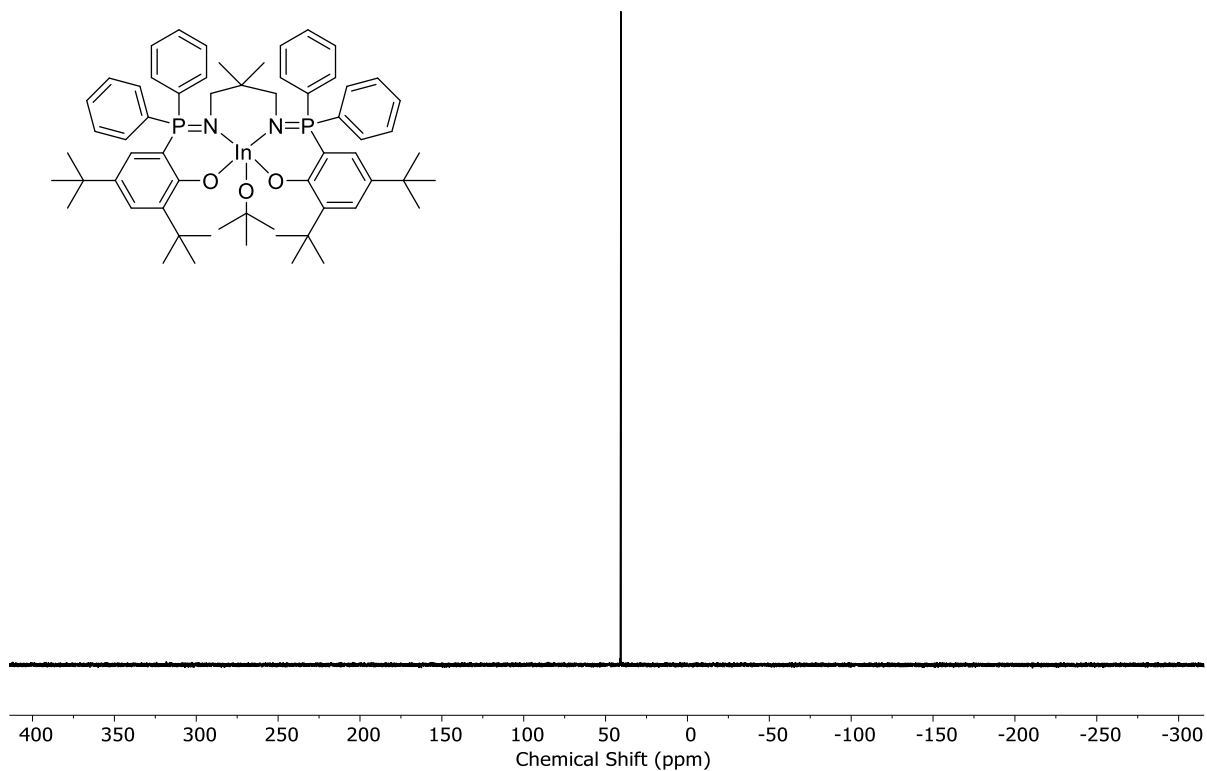


**Figure S31.**  $^{31}\text{P}\{^1\text{H}\}$  NMR spectrum of complex 3 in  $\text{THF-}d_8$ .

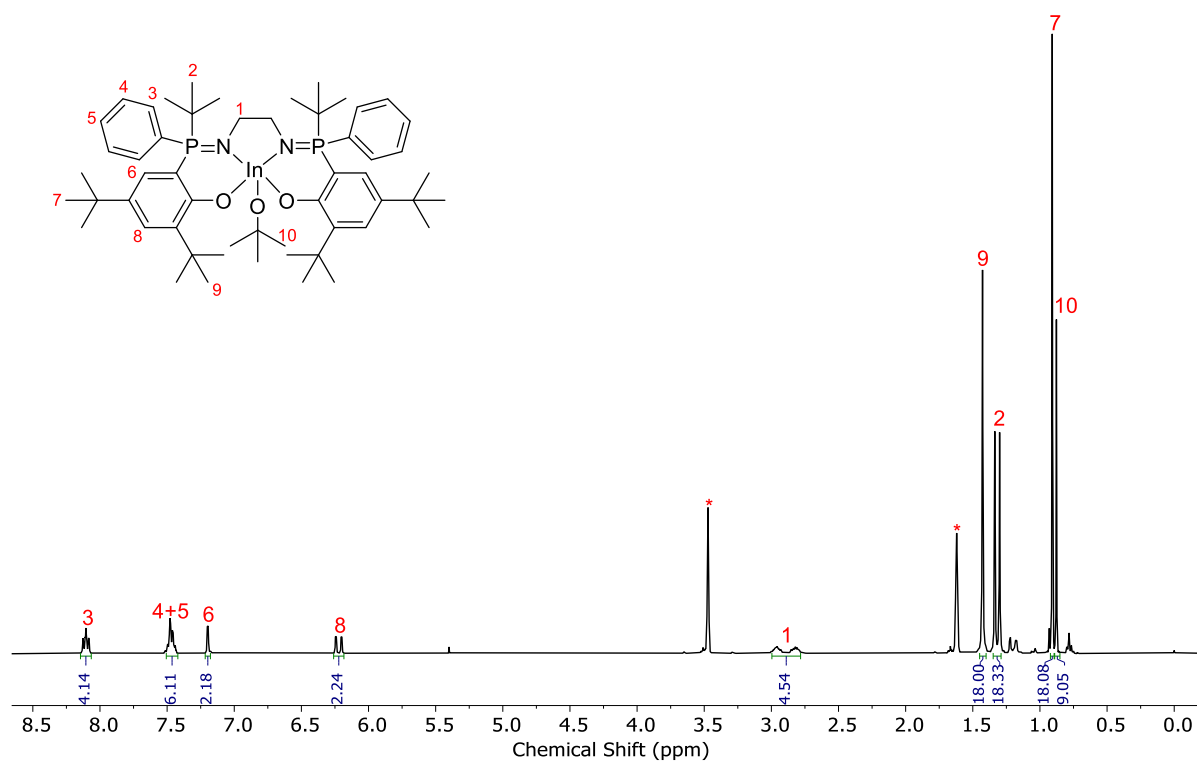


**Figure S32.**  $^1\text{H}$  NMR spectrum of indium complex **4** in  $\text{THF-}d_8$ .

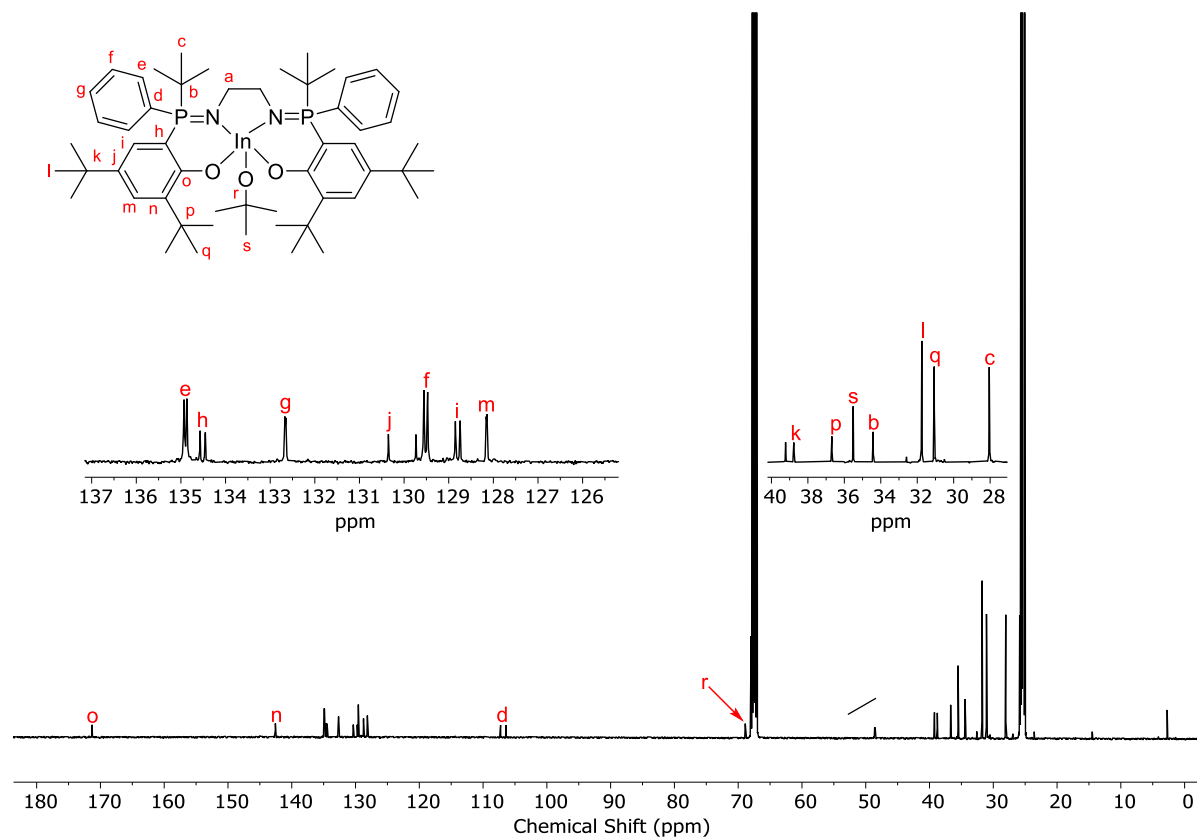


**Figure S33.**  $^{13}\text{C}\{^1\text{H}\}$  NMR spectrum of indium complex **4** in  $\text{THF-}d_8$ .

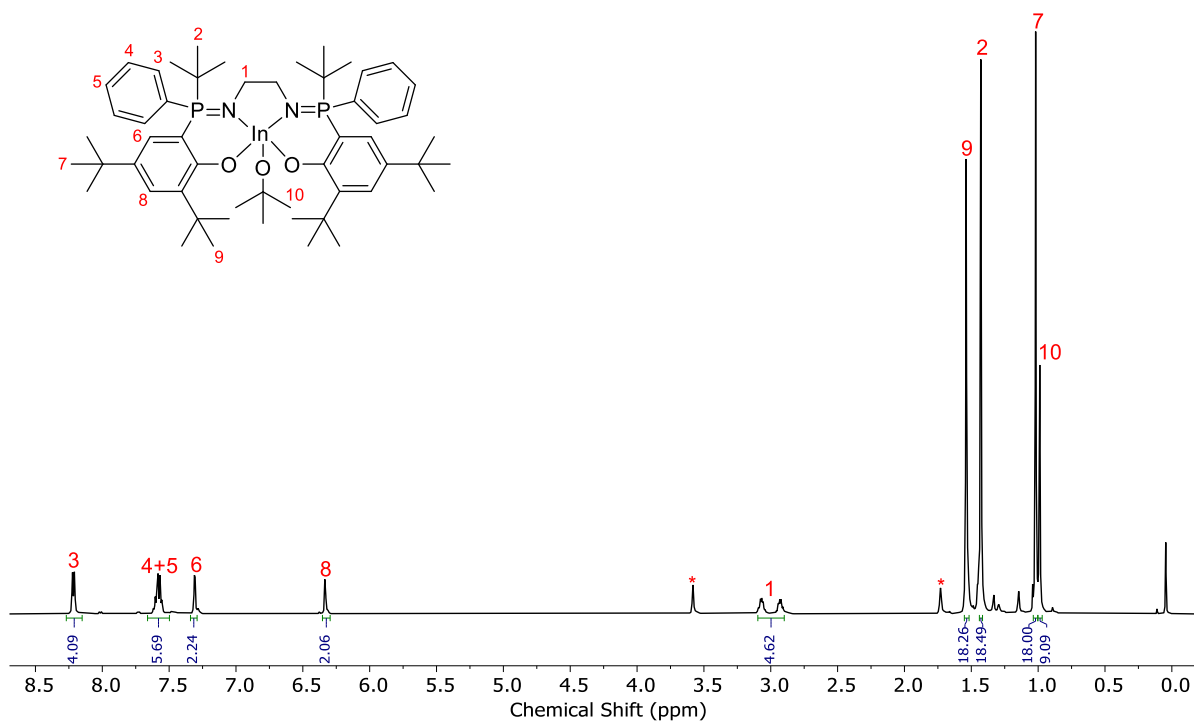


**Figure S34.**  $^1\text{H}\{^{31}\text{P}\}$  NMR spectrum of complex **4** in  $\text{THF-}d_8$ .

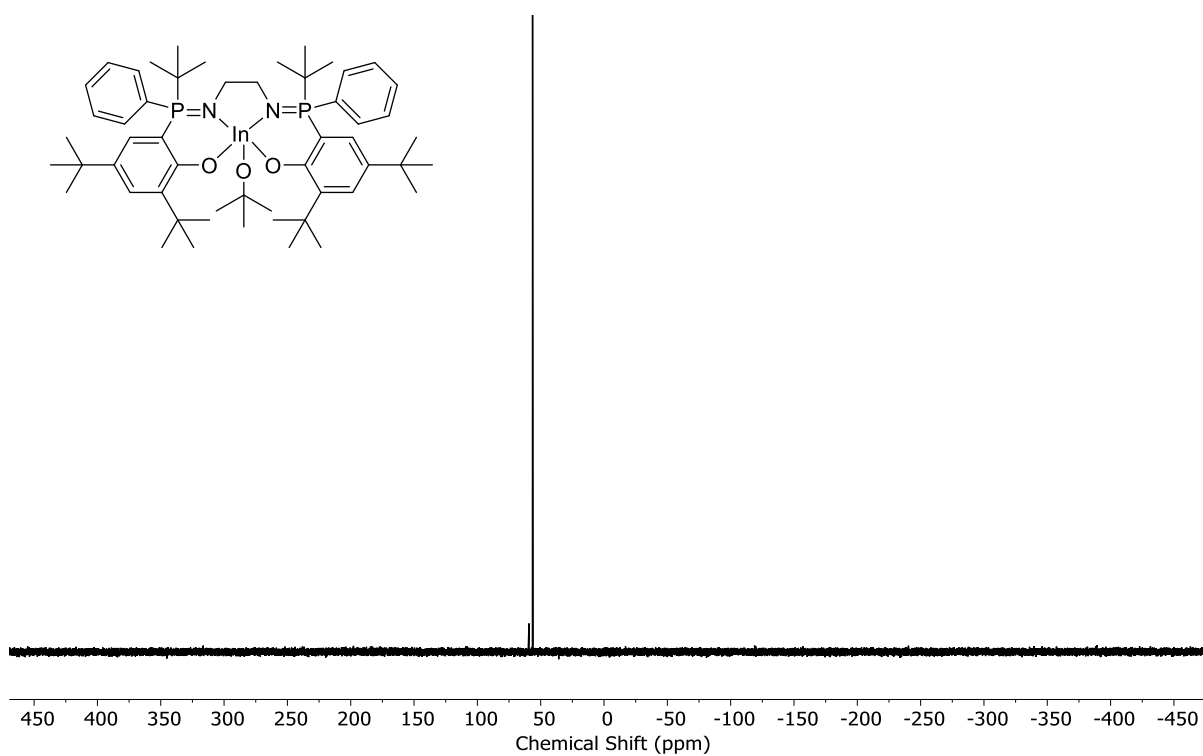


**Figure S35.**  $^{31}\text{P}\{^1\text{H}\}$  NMR spectrum of indium complex **4** in  $\text{THF-}d_8$ .

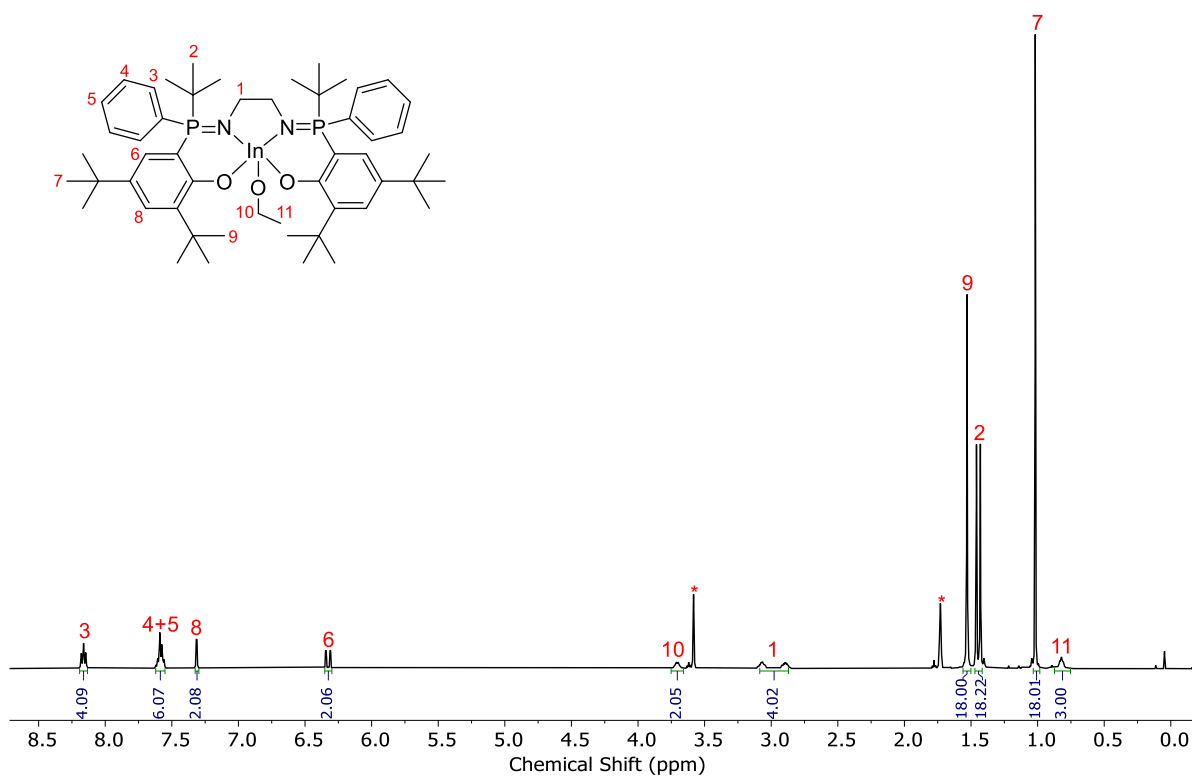


**Figure S36.**  $^1\text{H}$  NMR spectrum of indium complex **5** in  $\text{THF-}d_8$ .

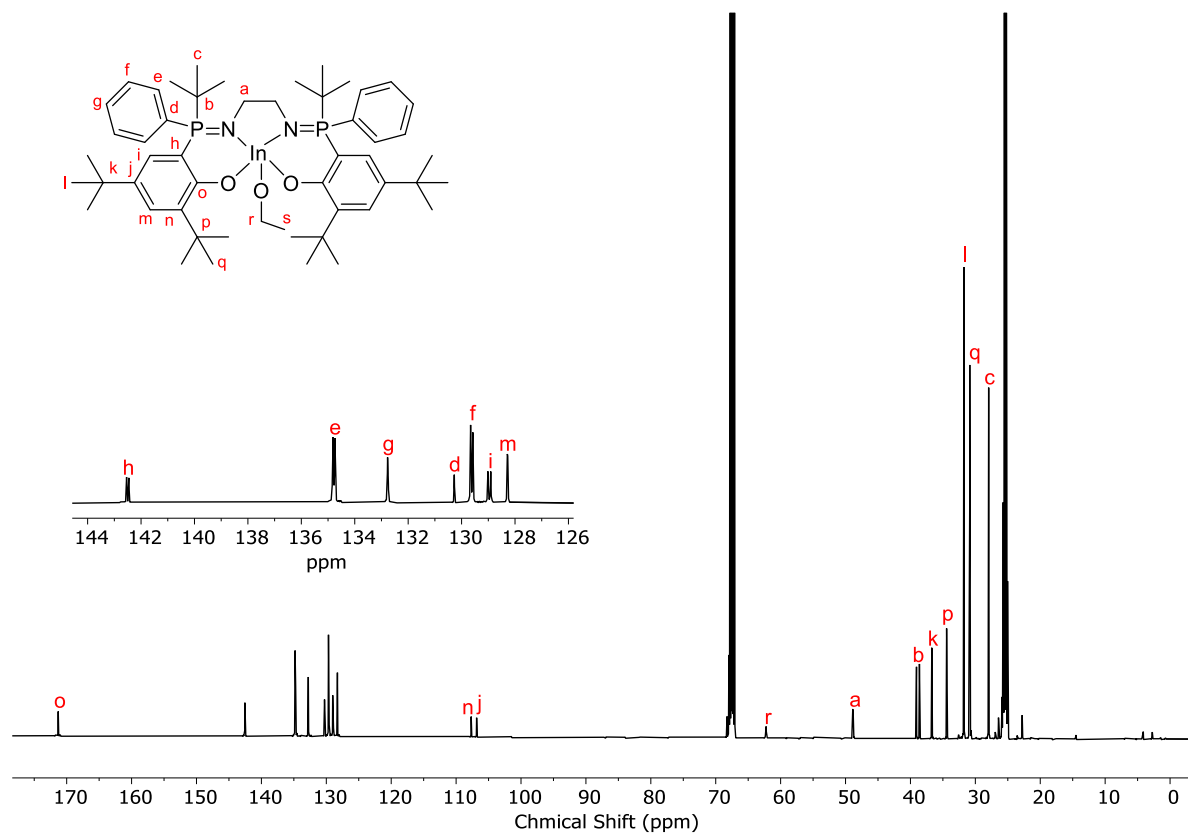


**Figure S37.**  $^{13}\text{C}\{^1\text{H}\}$  NMR spectrum of indium complex **5** in  $\text{THF-}d_8$ .

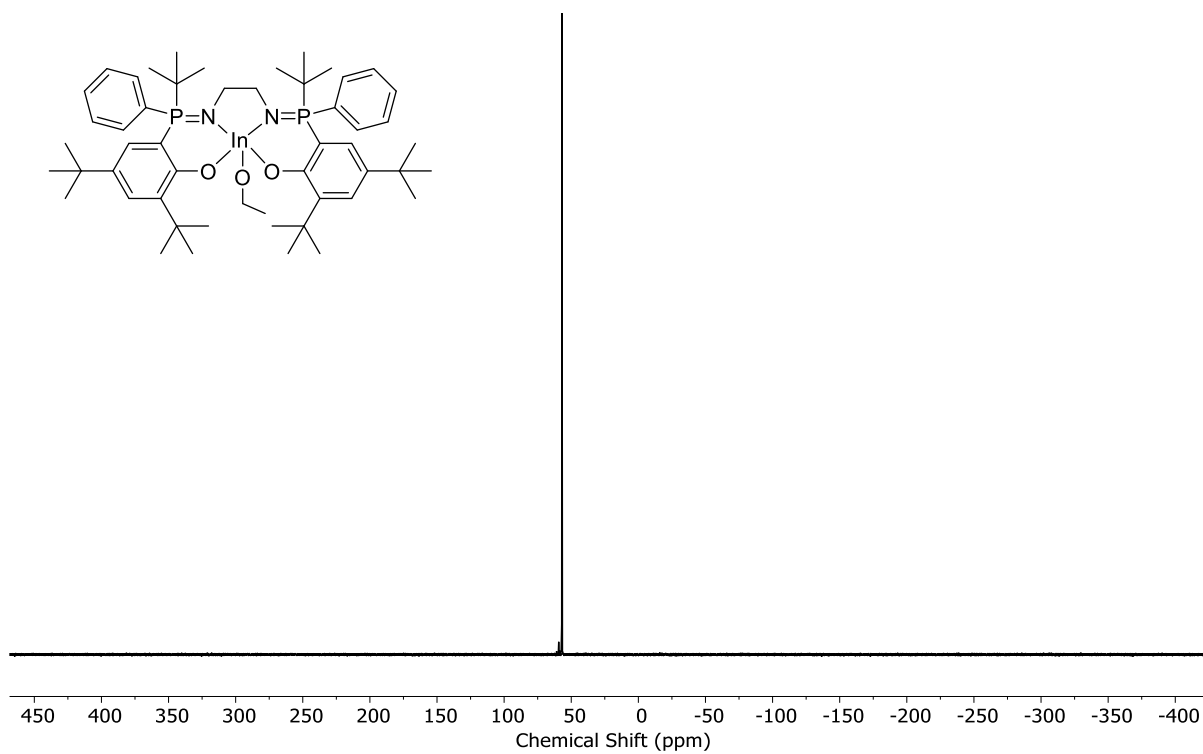


**Figure S38.**  $^{31}\text{P}\{^1\text{H}\}$  NMR spectrum of indium complex **5** in  $\text{THF-}d_8$ .

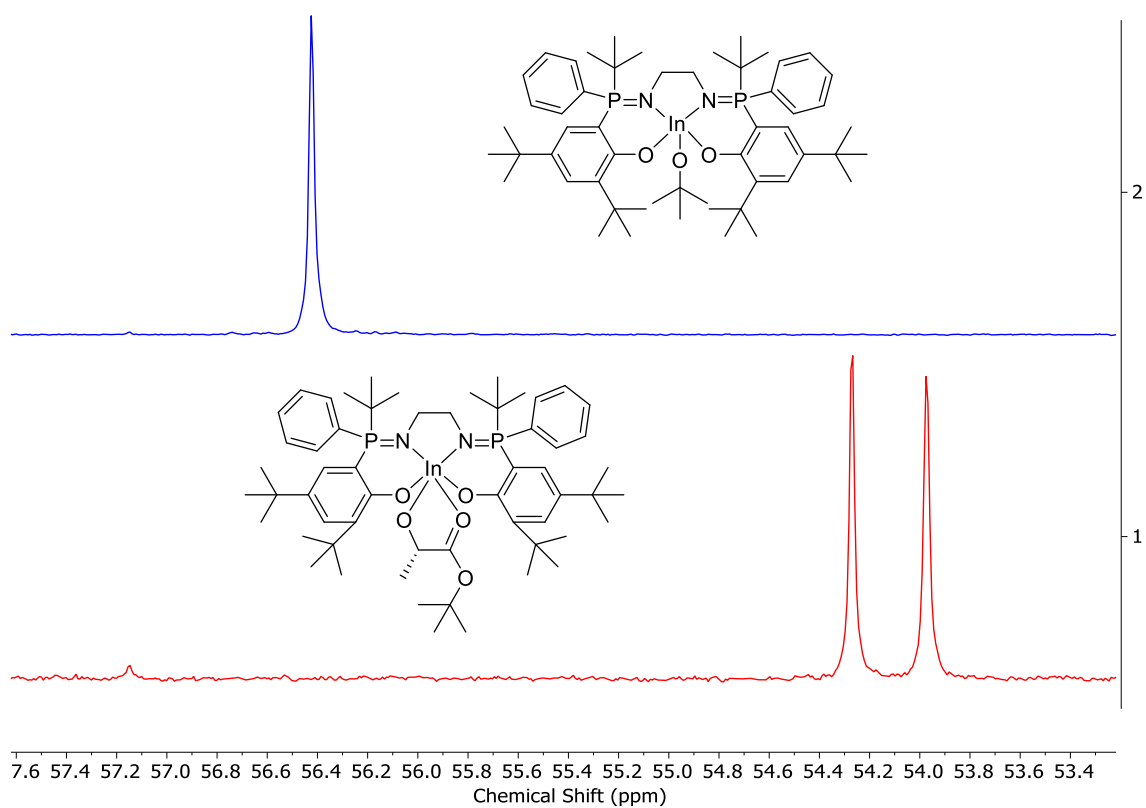
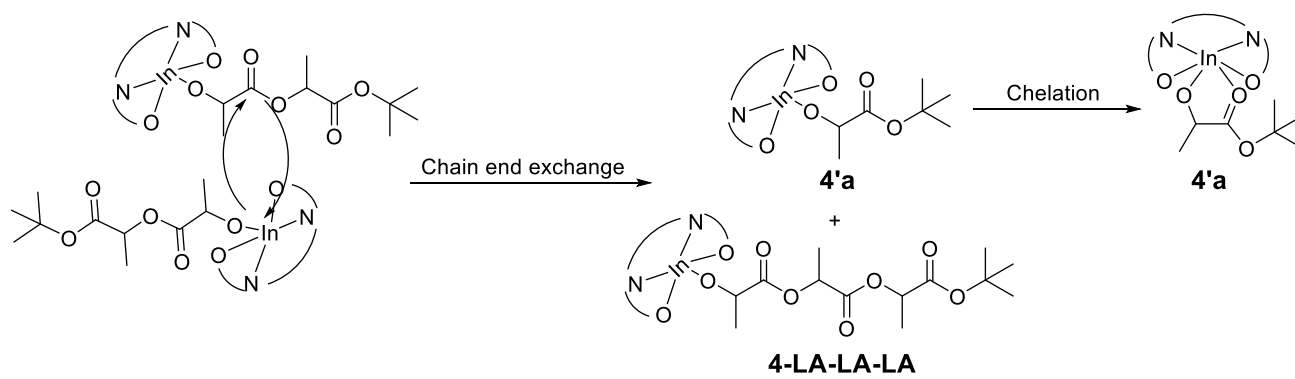


**Figure S39.** Stacked  $^{31}\text{P}\{^1\text{H}\}$  NMR spectra of indium complexes **4** and **4'a** in  $\text{THF-}d_8$ .



**Scheme S3.** Proposed mechanism for the formation of intermediate **4'a**.

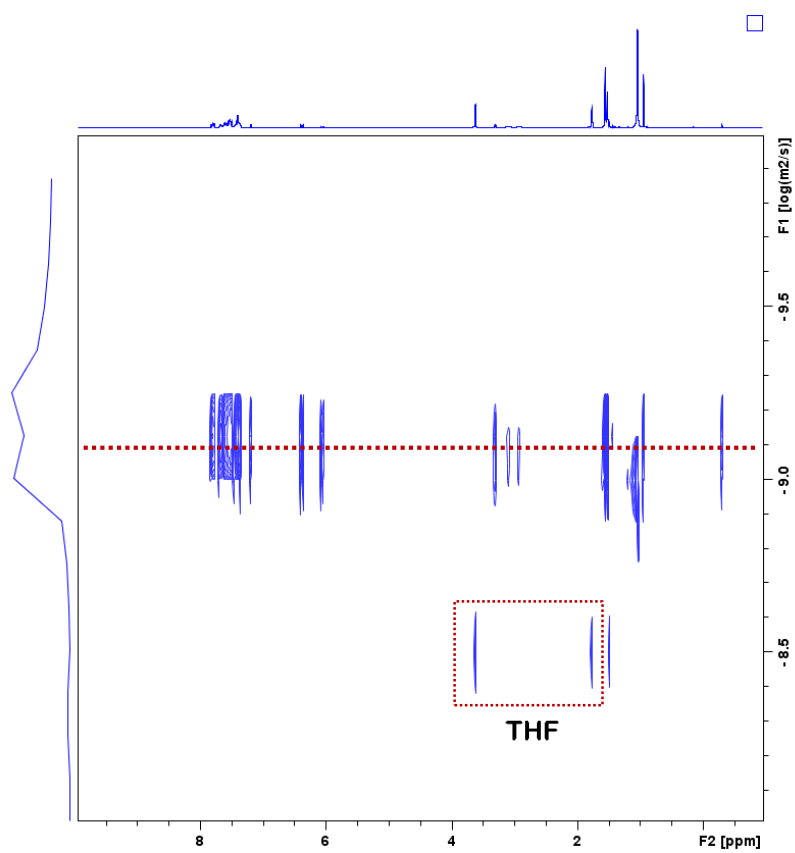


**Figure S40.** <sup>1</sup>H DOSY NMR spectrum of complex **1** in THF-*d*<sub>8</sub>.

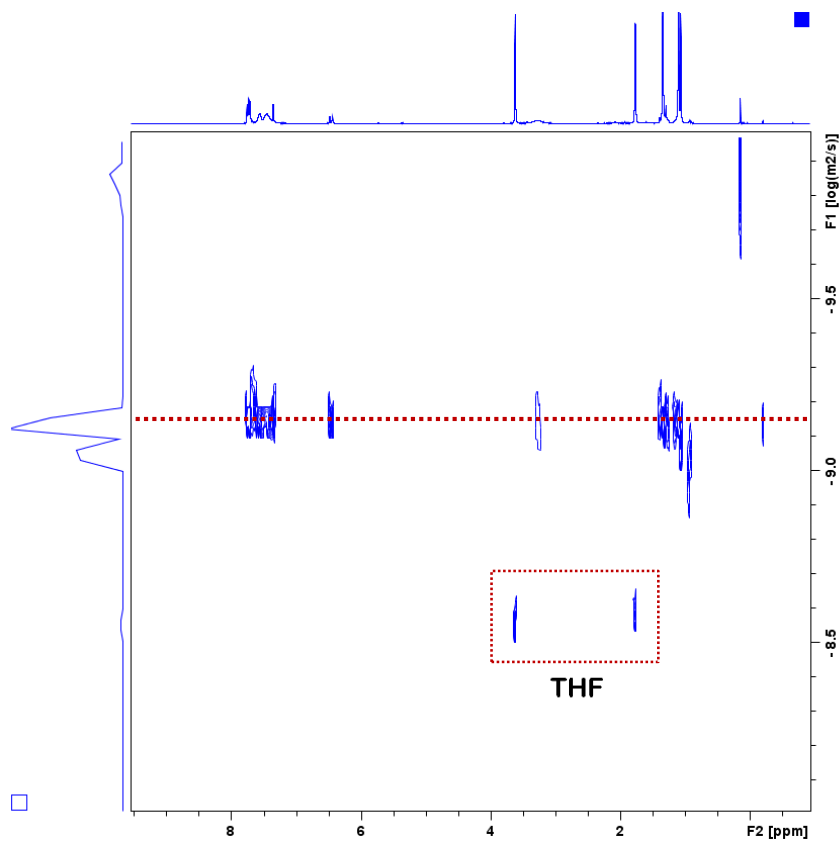


**Figure S41.**  $^1\text{H}$  DOSY NMR spectrum of complex **2** in  $\text{THF-}d_8$ .

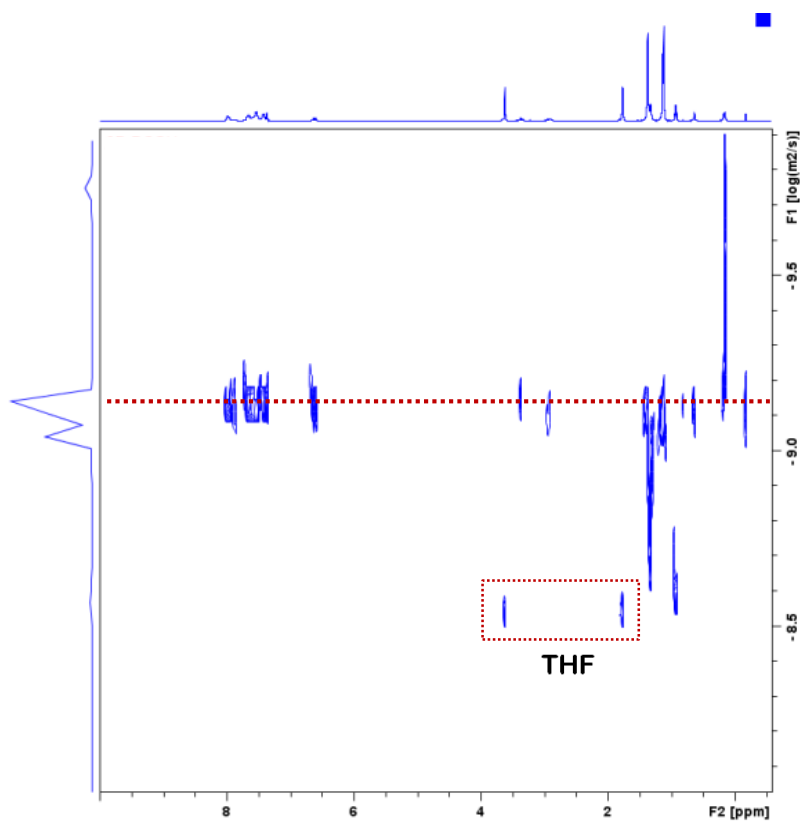


**Figure S42.**  $^1\text{H}$  DOSY NMR spectrum of indium complex **3** in  $\text{THF-}d_8$ .

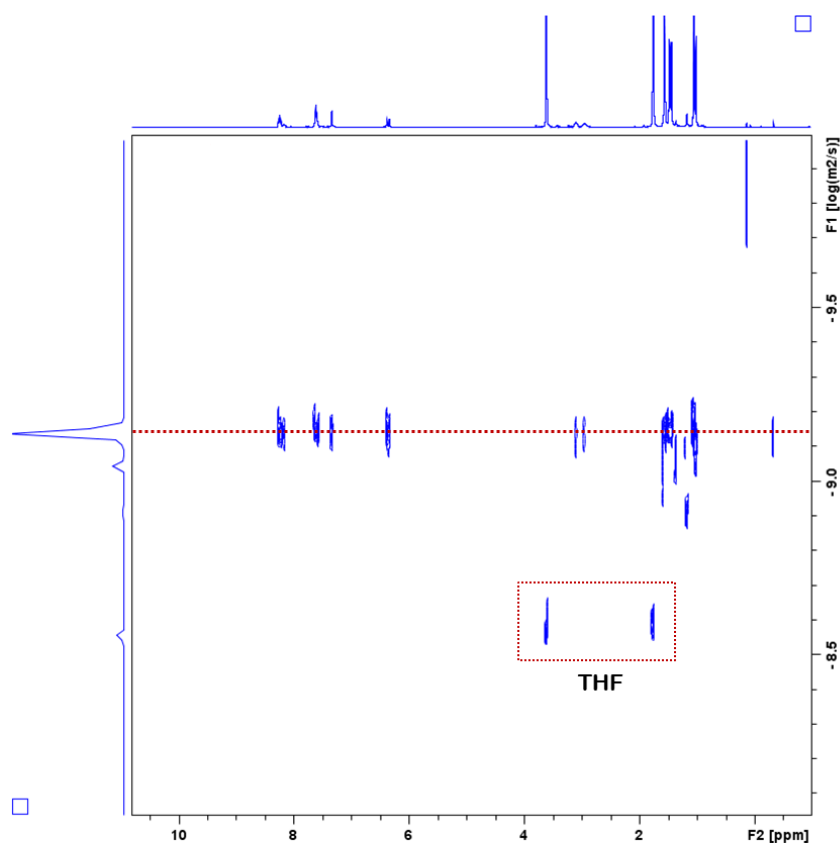


**Figure S43.** <sup>1</sup>H DOSY NMR spectrum of indium complex **4** in THF-*d*<sub>8</sub>.

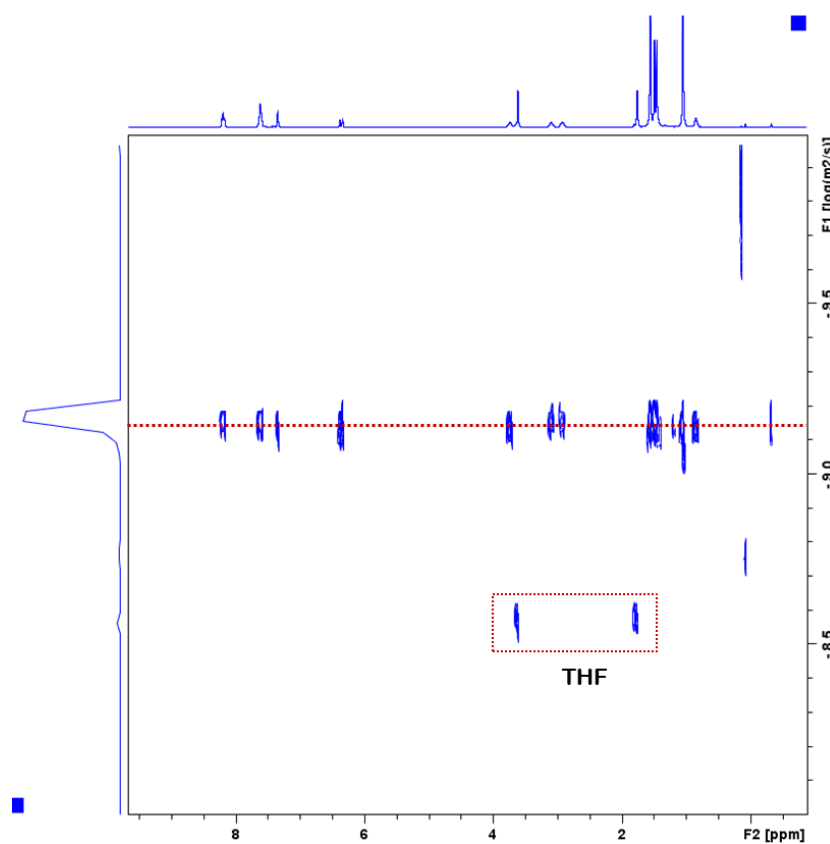


**Figure S44.** <sup>1</sup>H DOSY NMR spectrum of indium complex **5** in THF-*d*<sub>8</sub>.

## S2.8. Additional crystallographic data for ligand H<sub>2</sub>L<sup>4</sup>

### Structure of phosphasalen ligand H<sub>2</sub>L<sup>4</sup>

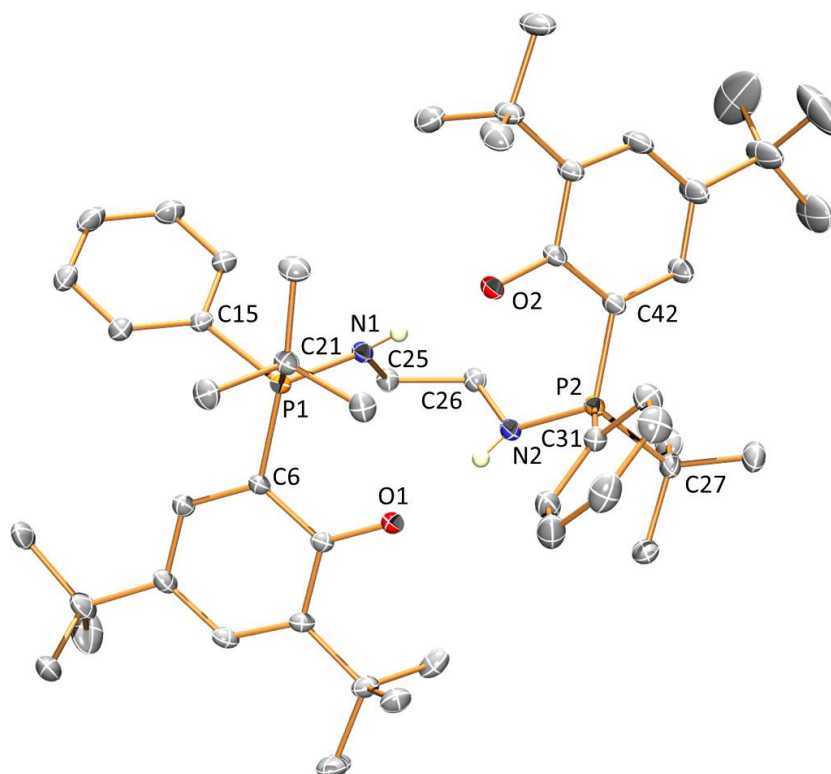


**Figure S45.** Representation of the molecular structure of ligand H<sub>2</sub>L<sup>4</sup>.

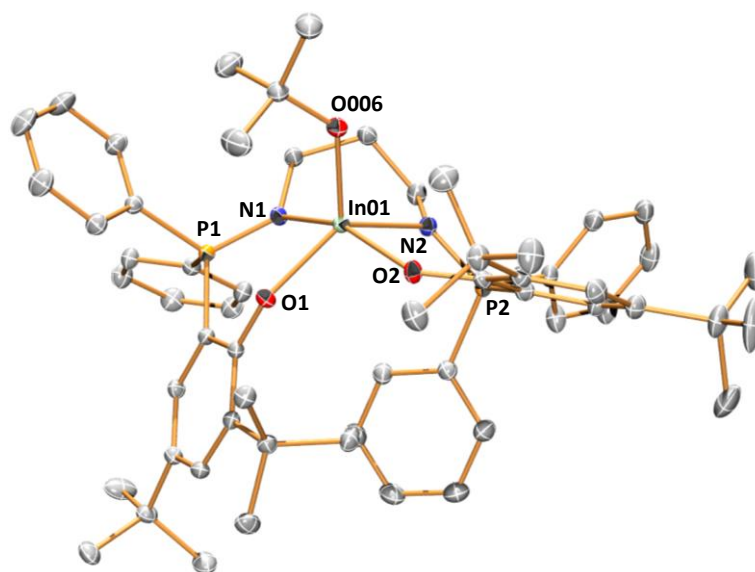
**Table S1.** Selected bond lengths (Å) of ligand H<sub>2</sub>L<sup>4</sup>.

H <sub>2</sub> L <sup>4</sup> Bond length (Å)	
P(1)-N(1)	1.629(1)
P(1)-C(6)	1.783(1)
P(1)-C(15)	1.826(1)
P(1)-C(21)	1.849(2)
P(2)-N(2)	1.639(1)
P(2)-C(27)	1.856(2)
P(2)-C(31)	1.803(2)
P(2)-C(42)	1.766(1)
N(1)-C(25)	1.466(2)
N(2)-C(26)	1.464(2)

**Table S2.** Summary of crystallographic refinement data for ligand **H<sub>2</sub>L<sup>4</sup>**.

<b>Compound</b>	<b>Complex H<sub>2</sub>L<sup>4</sup></b>
<b>Empirical Formula</b>	C <sub>50</sub> H <sub>74</sub> N <sub>2</sub> O <sub>2</sub> P <sub>2</sub>
<b>Formula weight (gmol<sup>-1</sup>)</b>	797.05
<b>Crystal system</b>	Triclinic
<b>a (Å)</b>	11.4385(4)
<b>b (Å)</b>	15.3688(5)
<b>c (Å)</b>	15.4343(5)
<b>α (°)</b>	84.413(3)
<b>β (°)</b>	78.850(3)
<b>γ (°)</b>	78.526(3)
<b>Unit cell volume (Å<sup>3</sup>)</b>	2600.66(16)
<b>No. of formula units per unit cell</b>	2
<b>Space group</b>	P-1
<b>Density (calculated) (Mg m<sup>-3</sup>)</b>	1.018
<b>Diffraction wavelength (Å)</b>	1.54184
<b>Temperature (K)</b>	150(2)
<b>Absorption coefficient (mm<sup>-1</sup>)</b>	1.020
<b>No. of reflections collected</b>	27304
<b>No. of unique reflections</b>	10793
<b>R<sub>int</sub></b>	0.0301
<b>Final R<sub>1</sub> values (I &gt; 2σI)</b>	0.0451
<b>Final wR<sub>2</sub> values (I &gt; 2σI)</b>	0.1199
<b>R<sub>1</sub> values (all data)</b>	0.0548
<b>wR<sub>2</sub> values (all data)</b>	0.1289
<b>Goodness of fit on F<sup>2</sup></b>	1.027

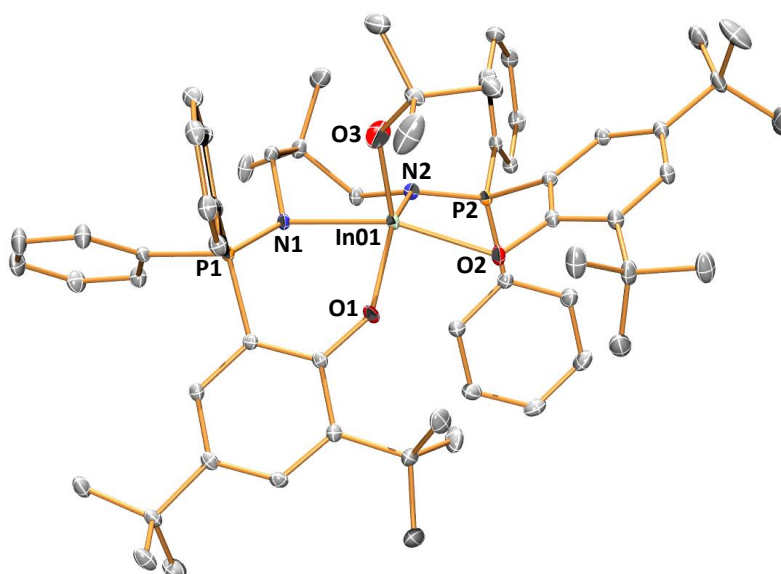
## S2.9. Additional crystallographic data for indium complexes 2–5 and intermediate 4'a



**Figure S46.** Representation of the molecular structure of complex 2.

**Table S3.** Selected bond lengths (Å) and angles (°) of complex 2.

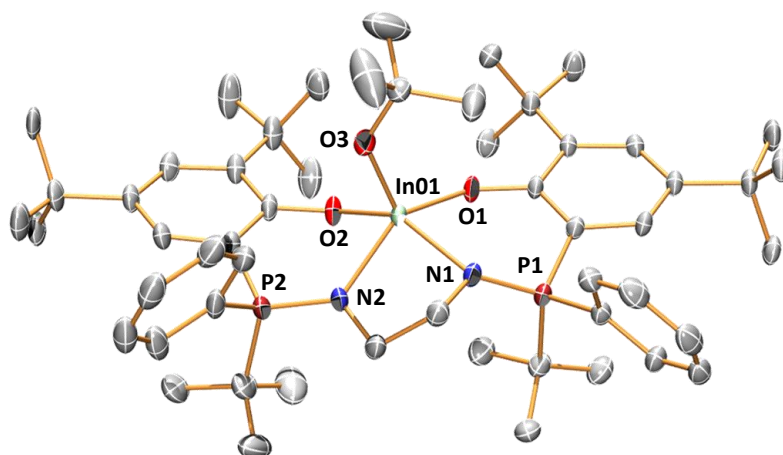
Bond length (Å)		Angle (°)			
In(01)-N(1)	2.218(1)	N(1)-In(01)-N(2)	84.64(5)	N(2)-In(01)-O(2)	85.25(5)
In(01)-N(2)	2.176(1)	N(1)-In(01)-O(1)	86.41(5)	N(2)-In(01)-O(006)	109.12(5)
In(01)-O(1)	2.106(1)	N(1)-In(01)-O(2)	157.09(5)	O(1)-In(01)-O(2)	86.43(5)
In(01)-O(2)	2.127(1)	N(1)-In(01)-O(3)	106.54(5)	O(1)-In(01)-O(006)	115.38(5)
In(01)-O(006)	2.025(1)	N(2)-In(01)-O(1)	135.34(5)	O(2)-In(01)-O(006)	96.18(5)



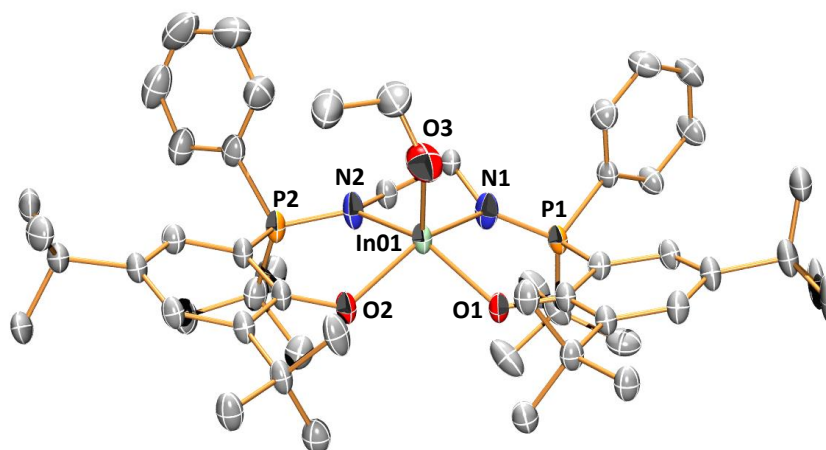
**Figure S47.** Representation of the molecular structure of complex 3.

**Table S4.** Selected bond lengths (Å) and angles (°) of complex **3**.

Bond length (Å)		Angle (°)			
In(01)-N(1)	2.250(3)	N(1)-In(01)-N(2)	83.2(1)	N(2)-In(01)-O(2)	88.0(1)
In(01)-N(2)	2.168(3)	N(1)-In(01)-O(1)	87.4(1)	N(2)-In(01)-O(3)	107.1(1)
In(01)-O(1)	2.090(3)	N(1)-In(01)-O(2)	157.0(1)	O(1)-In(01)-O(2)	84.7(1)
In(01)-O(2)	2.152(2)	N(1)-In(01)-O(3)	91.5(1)	O(1)-In(01)-O(3)	115.0(1)
In(01)-O(3)	2.002(4)	N(2)-In(01)-O(1)	137.1(1)	O(2)-In(01)-O(3)	111.4(1)

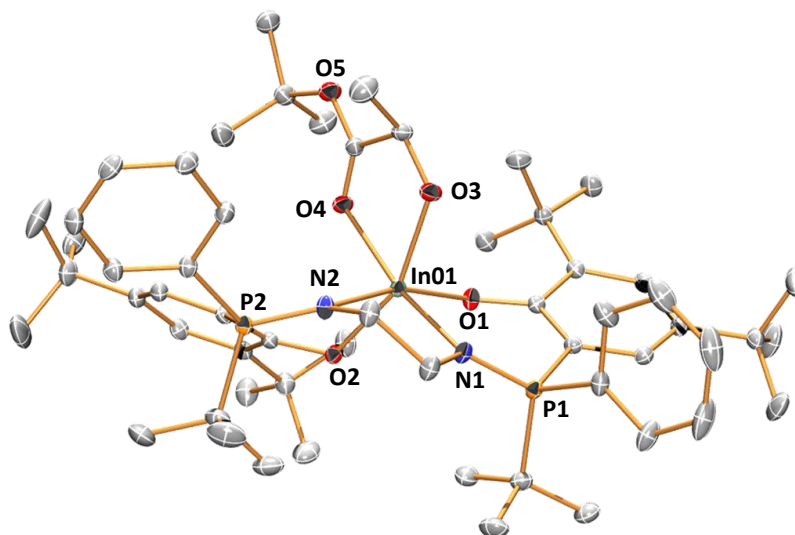
**Figure S48.** Representation of the molecular structure of complex **4**.**Table S5.** Selected bond lengths (Å) and angles (°) of complex **4**.

Bond length (Å)		Angle (°)			
In(01)-N(1)	2.178(4)	N(1)-In(01)-N(2)	77.2(1)	N(2)-In(01)-O(2)	85.9(1)
In(01)-N(2)	2.190(4)	N(1)-In(01)-O(1)	88.4(1)	N(2)-In(01)-O(3)	99.8(1)
In(01)-O(1)	2.100(3)	N(1)-In(01)-O(2)	146.5(1)	O(1)-In(01)-O(2)	90.2(1)
In(01)-O(2)	2.094(3)	N(1)-In(01)-O(3)	108.2(1)	O(1)-In(01)-O(3)	117.2(1)
In(01)-O(3)	2.025(4)	N(2)-In(01)-O(1)	142.9(1)	O(2)-In(01)-O(3)	103.0(1)

**Figure S49.** Representation of the molecular structure of complex **5**.

**Table S6.** Selected bond lengths (Å) and angles (°) of complex **5**.

Bond length (Å)		Angle (°)			
In(01)-N(1)	2.173(5)	N(1)-In(01)-N(2)	76.9(2)	N(2)-In(01)-O(2)	86.6(2)
In(01)-N(2)	2.171(4)	N(1)-In(01)-O(1)	87.2(2)	N(2)-In(01)-O(3)	109.2(2)
In(01)-O(1)	2.111(3)	N(1)-In(01)-O(2)	145.5(2)	O(1)-In(01)-O(2)	90.2(2)
In(01)-O(2)	2.116(4)	N(1)-In(01)-O(3)	109.2(2)	O(1)-In(01)-O(3)	104.4(2)
In(01)-O(3)	2.051(6)	N(2)-In(01)-O(1)	146.0(1)	O(2)-In(01)-O(3)	104.7(2)

**Figure S50.** Representation of the molecular structure of intermediate **4'a**.**Table S7.** Selected bond lengths (Å) and angles (°) of intermediate **4'a**.

Bond length (Å)		Angle (°)			
In(01)-N(1)	2.184(2)	N(1)-In(01)-N(2)	78.93(9)	N(2)-In(01)-O(4)	103.19(9)
In(01)-N(2)	2.179(2)	N(1)-In(01)-O(1)	89.14(9)	O(1)-In(01)-O(2)	89.03(8)
In(01)-O(1)	2.101(2)	N(1)-In(01)-O(2)	107.42(9)	O(1)-In(01)-O(3)	98.91(9)
In(01)-O(2)	2.125(2)	N(1)-In(01)-O(3)	95.7(1)	O(1)-In(01)-O(4)	90.51(8)
In(01)-O(3)	2.100(2)	N(1)-In(01)-O(4)	169.30(9)	O(2)-In(01)-O(3)	155.69(9)
In(01)-O(4)	2.355(2)	N(2)-In(01)-O(1)	164.01(9)	O(2)-In(01)-O(4)	83.27(8)
		N(2)-In(01)-O(2)	84.50(9)	O(3)-In(01)-O(4)	73.77(9)
		N(2)-In(01)-O(3)	92.9(1)		

**Table S8.** Summary of crystallographic refinement data for complexes **2**, **3**, and **5**.

<b>Compound</b>	<b>Complex 2</b>	<b>Complex 3</b>	<b>Complex 5</b>
<b>Empirical Formula</b>	C <sub>65</sub> H <sub>89</sub> InN <sub>2</sub> O <sub>3</sub> P <sub>2</sub>	C <sub>65</sub> H <sub>87</sub> InN <sub>2</sub> O <sub>4</sub> P <sub>2</sub>	C <sub>52</sub> H <sub>77</sub> InN <sub>2</sub> O <sub>3</sub> P <sub>2</sub>
<b>Formula weight (g mol<sup>-1</sup>)</b>	1123.14	1137.12	954.91
<b>Crystal system</b>	Monoclinic	Orthorhombic	Triclinic
<b>a (Å)</b>	15.1464(2)	20.6809(2)	14.2993(6)
<b>b (Å)</b>	16.9612(2)	18.5748(2)	14.3196(6)
<b>c (Å)</b>	26.1549(2)	15.7154(2)	17.8201(6)
<b>α (°)</b>	90	90	105.160(4)
<b>β (°)</b>	103.9430(10)	90	107.065(4)
<b>γ (°)</b>	90	90	96.826(4)
<b>Unit cell volume</b>	6521.25(13)	6036.97(12)	3290.3(2)
<b>No. of formula units per unit cell</b>	4	4	2
<b>Space group</b>	P2 <sub>1</sub> /c	Pna2 <sub>1</sub>	P-1
<b>Density (calculated) (Mg m<sup>-3</sup>)</b>	1.144	1.251	0.964
<b>Diffractometer wavelength</b>	1.54184	1.54184	1.54184
<b>Temperature (K)</b>	150(2)	150(2)	150(2)
<b>Absorption coefficient (mm<sup>-1</sup>)</b>	3.675	3.990	3.571
<b>No. of reflections collected</b>	77110	36488	36127
<b>No. of unique reflections</b>	13587	11541	13579
<b>R<sub>int</sub></b>	0.0327	0.0311	0.0892
<b>Final R<sub>1</sub> values (I &gt; 2σI)</b>	0.0275	0.0270	0.0671
<b>Final wR<sub>2</sub> values (I &gt; 2σI)</b>	0.0699	0.0692	0.1656
<b>R<sub>1</sub> values (all data)</b>	0.0312	0.0291	0.0887
<b>wR<sub>2</sub> values (all data)</b>	0.0722	0.0707	0.1842
<b>Goodness of fit on F<sup>2</sup></b>	1.025	1.067	0.987

**Table S9.** Summary of crystallographic refinement data for complex **4**, and intermediate **4'a**.

<b>Compound</b>	<b>Complex 4</b>	<b>Intermediate 4'a</b>
<b>Empirical Formula</b>	C <sub>63</sub> H <sub>102</sub> InN <sub>2</sub> O <sub>3</sub> P <sub>2</sub>	C <sub>57</sub> H <sub>85</sub> InN <sub>2</sub> O <sub>5</sub> P <sub>2</sub>
<b>Formula weight (g mol<sup>-1</sup>)</b>	1112.22	1055.02
<b>Crystal system</b>	Monoclinic	Orthorhombic
<b>a (Å)</b>	10.9894(2)	11.12800(10)
<b>b (Å)</b>	28.7519(10)	18.2363(2)
<b>c (Å)</b>	19.8100(4)	30.9376(4)
<b>α (°)</b>	90	90
<b>β (°)</b>	91.214(2)	90
<b>γ (°)</b>	90	90
<b>Unit cell volume (Å<sup>3</sup>)</b>	6257.9(3)	6278.28(12)
<b>No. of formula units per unit cell</b>	4	4
<b>Space group</b>	P2 <sub>1</sub> /n	P2 <sub>1</sub> 2 <sub>1</sub> 2 <sub>1</sub>
<b>Density (calculated) (Mg m<sup>-3</sup>)</b>	1.181	1.116
<b>Diffractometer wavelength (Å)</b>	1.54184	1.54184
<b>Temperature (K)</b>	150(2)	150(2)
<b>Absorption coefficient (mm<sup>-1</sup>)</b>	3.819	3.810
<b>No. of reflections collected</b>	52665	39863
<b>No. of unique reflections</b>	12991	13004
<b>R<sub>int</sub></b>	0.0633	0.0396
<b>Final R<sub>1</sub> values (I &gt; 2σI)</b>	0.0584	0.0255
<b>Final wR<sub>2</sub> values (I &gt; 2σI)</b>	0.1442	0.0615
<b>R<sub>1</sub> values (all data)</b>	0.0803	0.0281
<b>wR<sub>2</sub> values (all data)</b>	0.1581	0.0628
<b>Goodness of fit on F<sup>2</sup></b>	1.026	1.031

### S3. Additional polymerization data

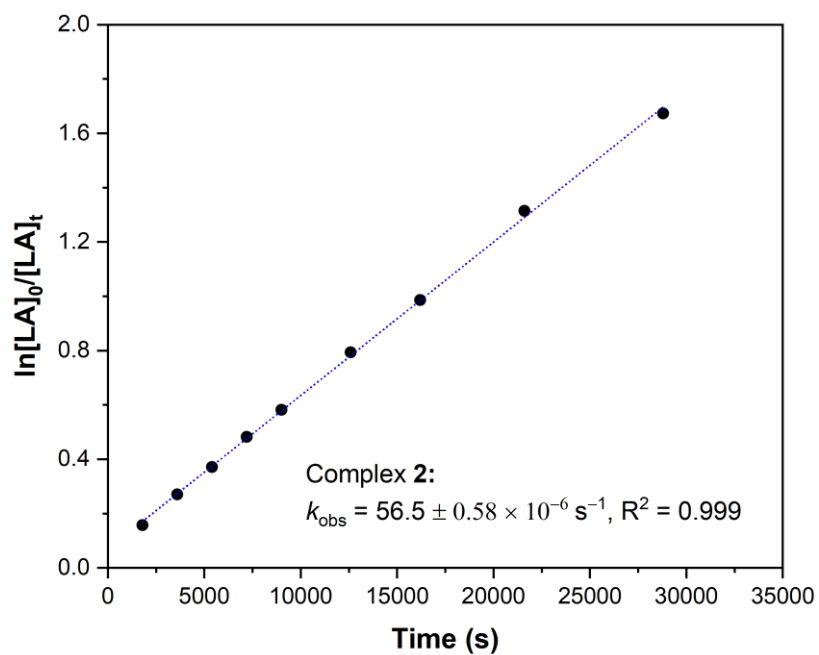


Figure S51. Semi-logarithmic plot for the polymerization of *rac*-LA using complex 2.

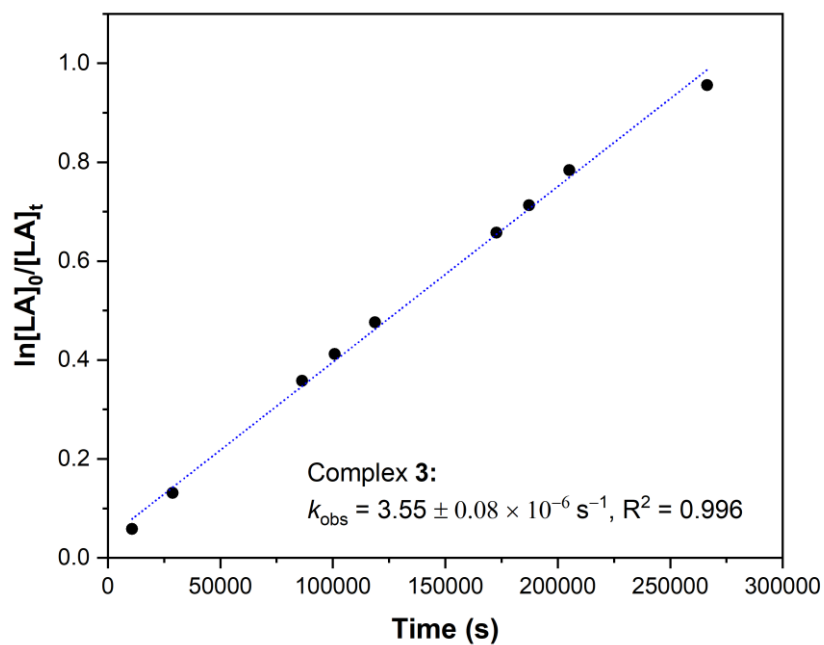
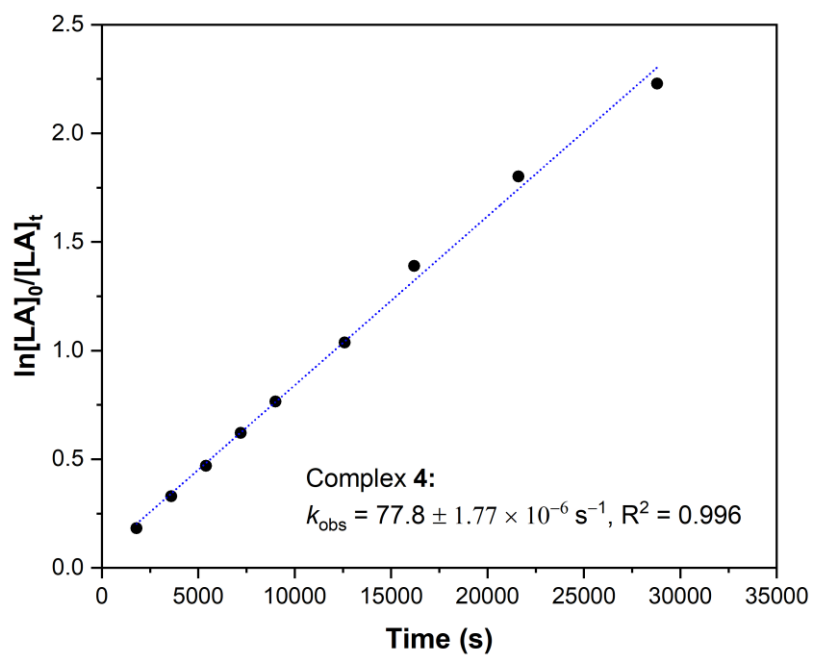
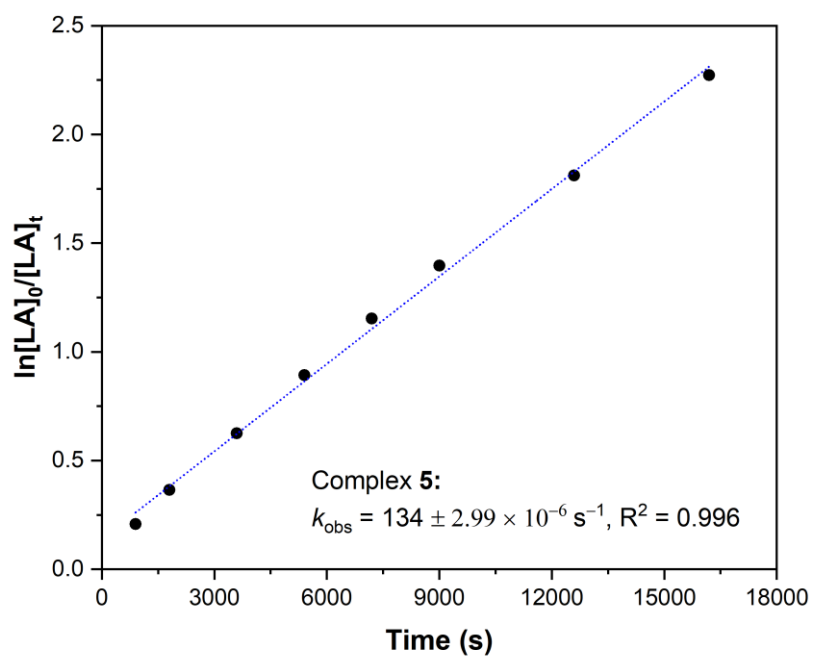


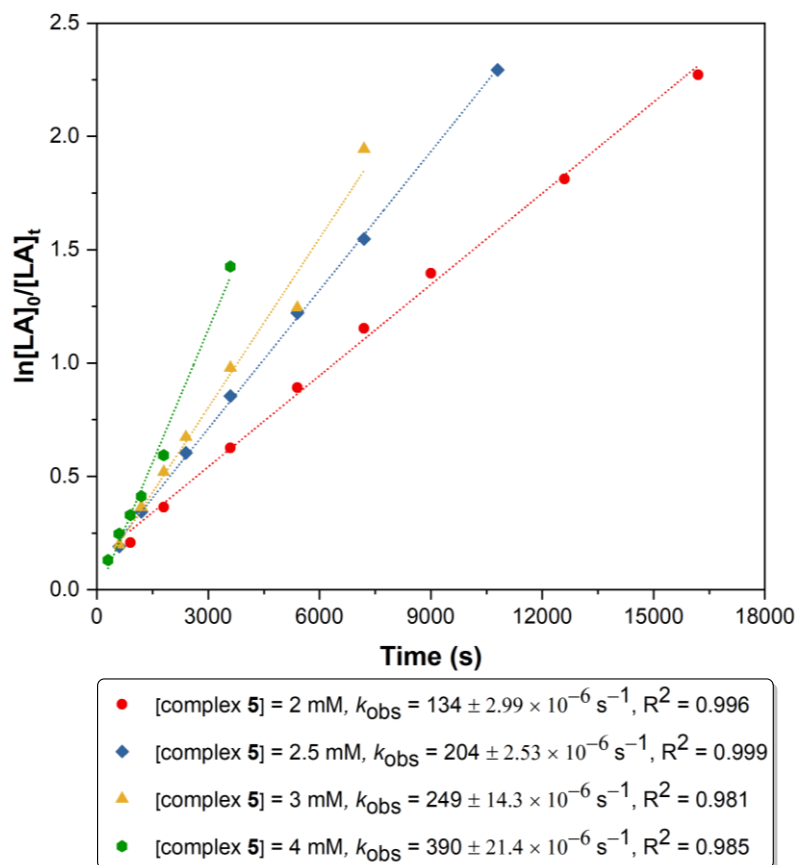
Figure S52. Semi-logarithmic plot for the polymerization of *rac*-LA using complex 3.



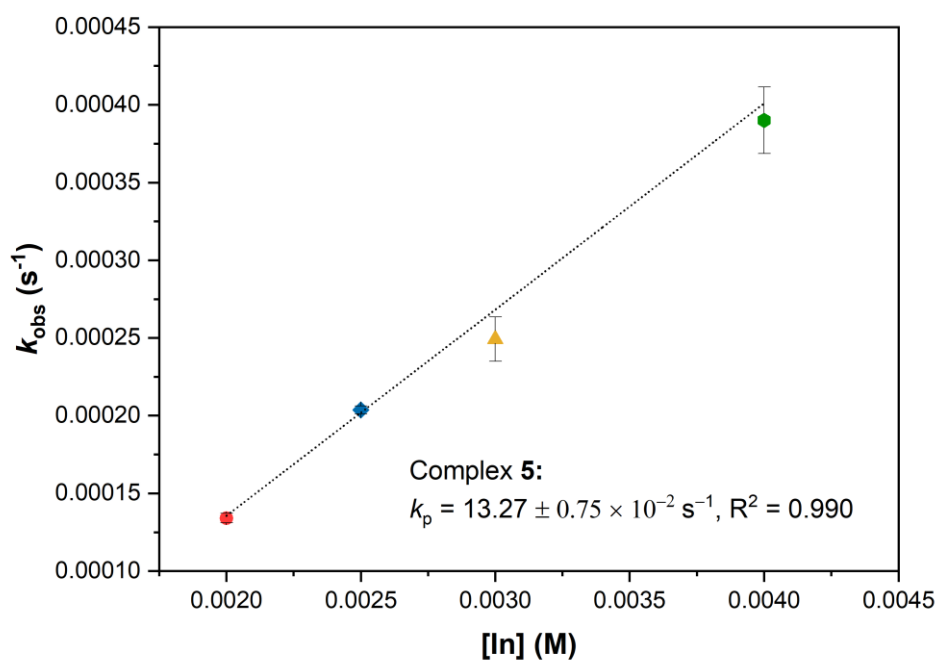
**Figure S53.** Semi-logarithmic plot for the polymerization of *rac*-LA using complex **4**.



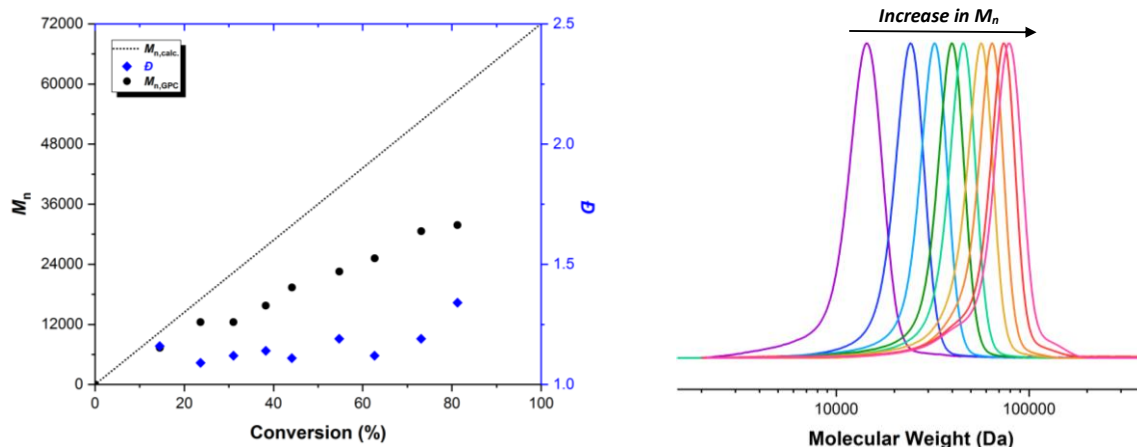
**Figure S54.** Semi-logarithmic plot for the polymerization of *rac*-LA using complex **5**.



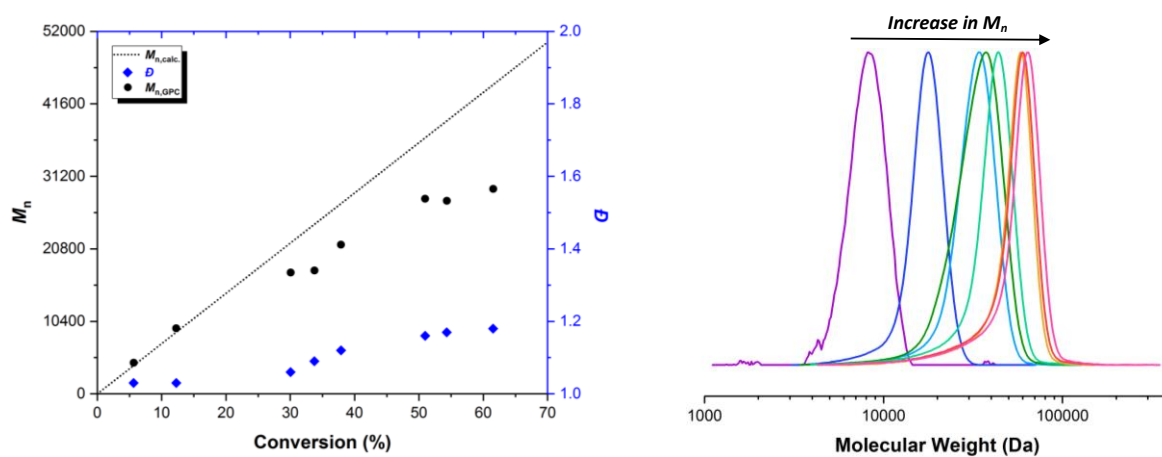
**Figure S55.** Semi-logarithmic plot for the polymerization of *rac*-LA using complex 5.



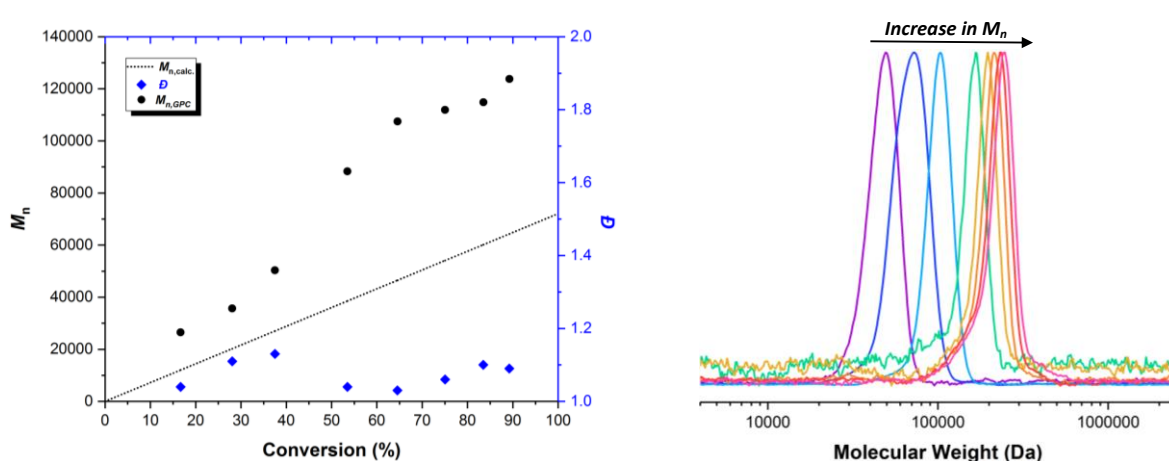
**Figure S56.** Plot of  $k_{\text{obs}}$  against [In] for the polymerization of *rac*-LA using complex 5.



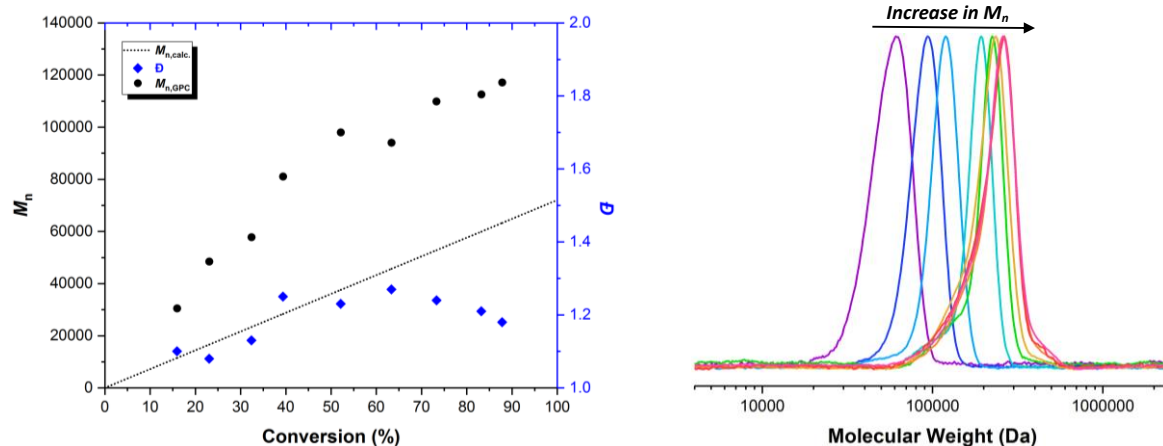
**Figure S57.** Plots of  $M_n$  (●), theoretical  $M_n$  (...) and  $D$  (◆) against percentage conversion (left) and overlay of GPC traces for the polymerization of *rac*-lactide initiated by complex **2** (right).



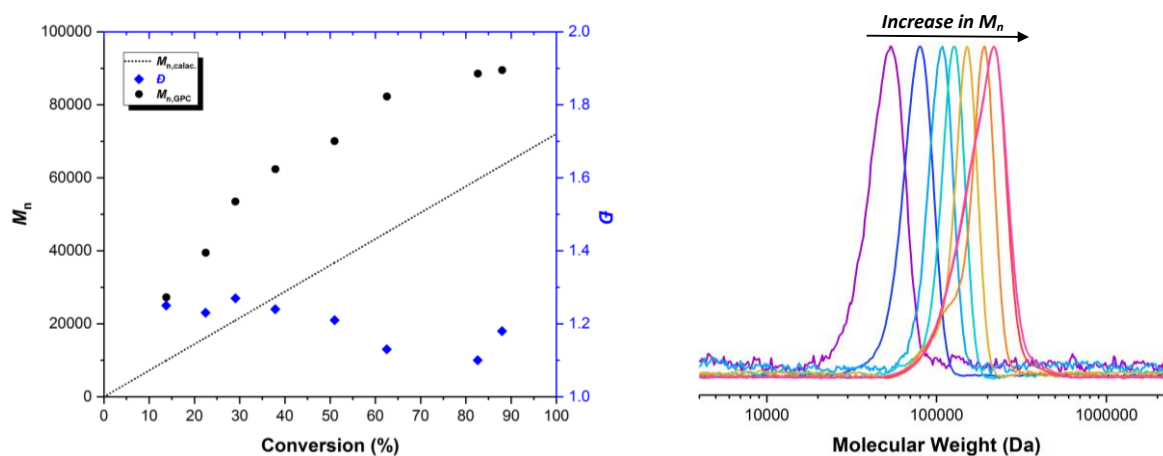
**Figure S58.** Plots of  $M_n$  (●), theoretical  $M_n$  (...) and  $D$  (◆) against percentage conversion (left) and overlay of GPC traces for the polymerization of *rac*-lactide initiated by complex **3** (right).



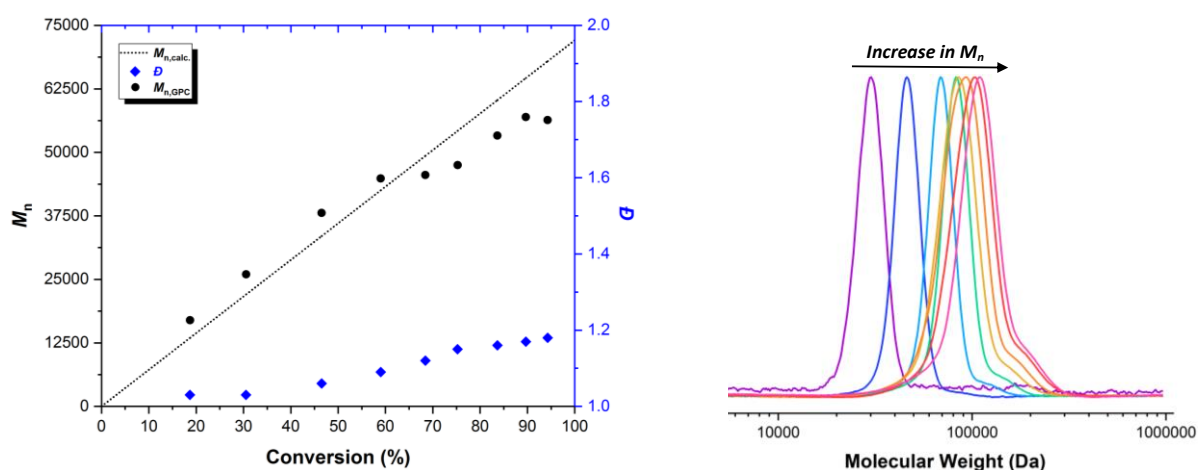
**Figure S59.** Plots of  $M_n$  (●), theoretical  $M_n$  (...) and  $D$  (◆) against percentage conversion (left) and overlay of GPC traces for the polymerization of *rac*-lactide initiated by complex **4** (right).



**Figure S60.** Plots of  $M_n$  (●), theoretical  $M_n$  (...) and  $D$  (◆) against percentage conversion (left) and overlay of GPC traces for the polymerization of *D*-lactide initiated by complex 4 (right).



**Figure S61.** Plots of  $M_n$  (●), theoretical  $M_n$  (...) and  $D$  (◆) against percentage conversion (left) and overlay of GPC traces for the polymerization of *L*-lactide initiated by complex 4 (right).

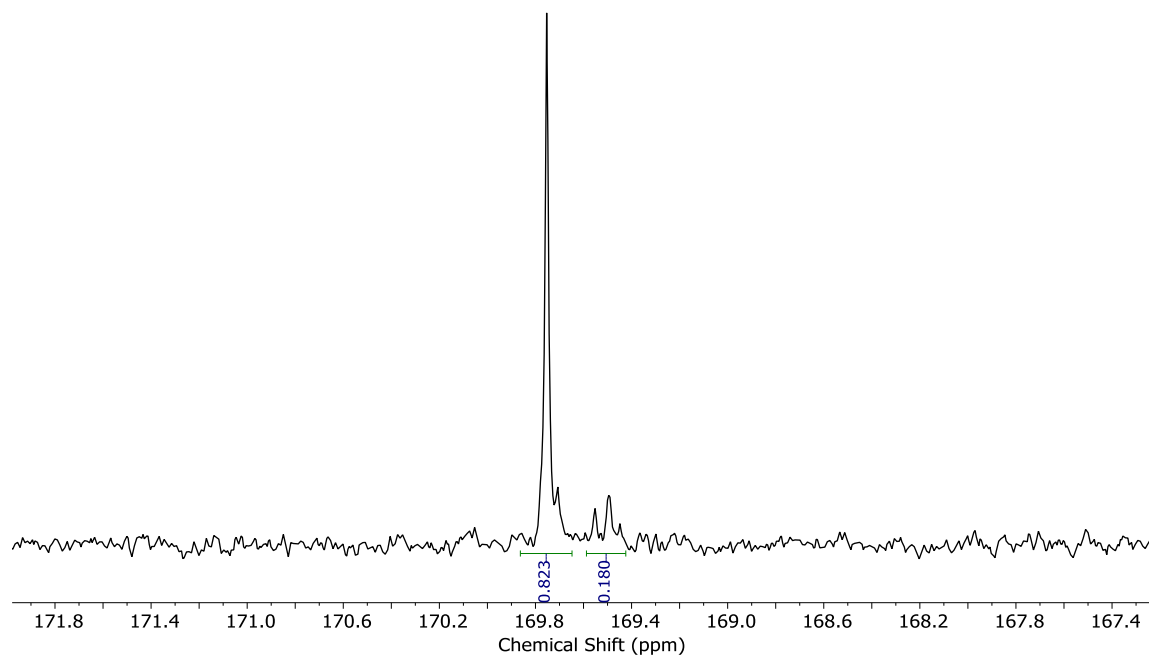


**Figure S62.** Plots of  $M_n$  (●), theoretical  $M_n$  (...) and  $D$  (◆) against percentage conversion (left) and overlay of GPC traces for the polymerization of *rac*-lactide initiated by complex 5 (right).

**Table S10.** PLA isotactic block length using complexes **4** and **5**.<sup>a</sup>

PLA Sample	Integral of the <i>iso</i> -hexad <sup>a</sup>	Integral of the <i>racemic</i> -hexad <sup>a</sup>	$P_i$ <sup>b</sup>	$P_s$ <sup>b</sup>	Average isotactic block length <sup>c</sup>
PLA1	0.8234	0.1766	0.9289	0.0711	14
PLA2	0.8796	0.1200	0.9582	0.0418	24
PLA3	0.8490	0.1486	0.9468	0.0531	19

<sup>a</sup> Determined from the normalised integral of the carbonyl signals in the  $^{13}\text{C}\{^1\text{H}\}$  NMR spectra at:  $\delta$  169.8 ppm for *iso*-hexad and  $\delta$  169.6–169.4 ppm for *racemic*-hexad.<sup>12</sup> <sup>b</sup> Calculated from the normalised integrals and using Bernoulian statistics, where  $P_i + P_s = 1$ .<sup>13</sup> <sup>c</sup> Identified from  $P_i$  and  $P_s$  values where the average isotactic polymer block length =  $1/P_s$ .<sup>13</sup>

**Figure S63.**  $^{13}\text{C}\{^1\text{H}\}$  NMR spectrum, showing the carbonyl region for PLA1 in  $\text{CDCl}_3$  (prepared by complex **5**,  $[\text{LA}]:[\mathbf{5}] = 500$ ,  $[\text{LA}] = 1 \text{ M}$ , THF, 298 K).

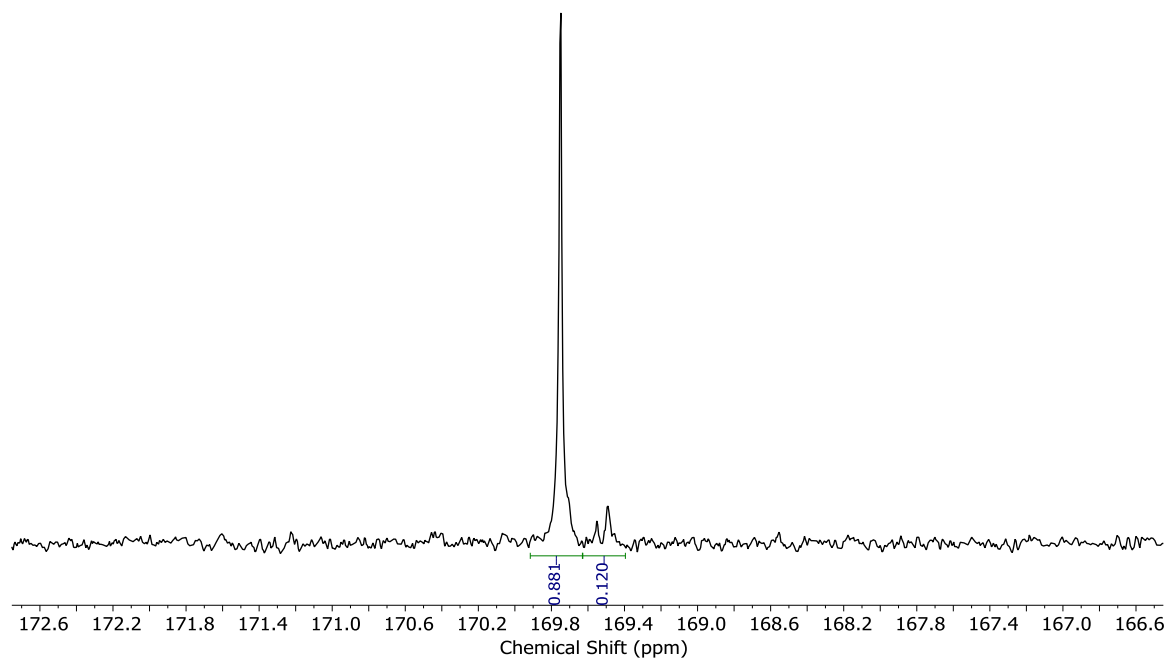


**Figure S64.**  $^{13}\text{C}\{^1\text{H}\}$  NMR spectrum, showing carbonyl region for PLA2 in  $\text{CDCl}_3$  (prepared by complex **4**,  $[\text{LA}]:[\mathbf{4}] = 500$ ,  $[\text{LA}] = 1 \text{ M}$ , THF, 278 K).

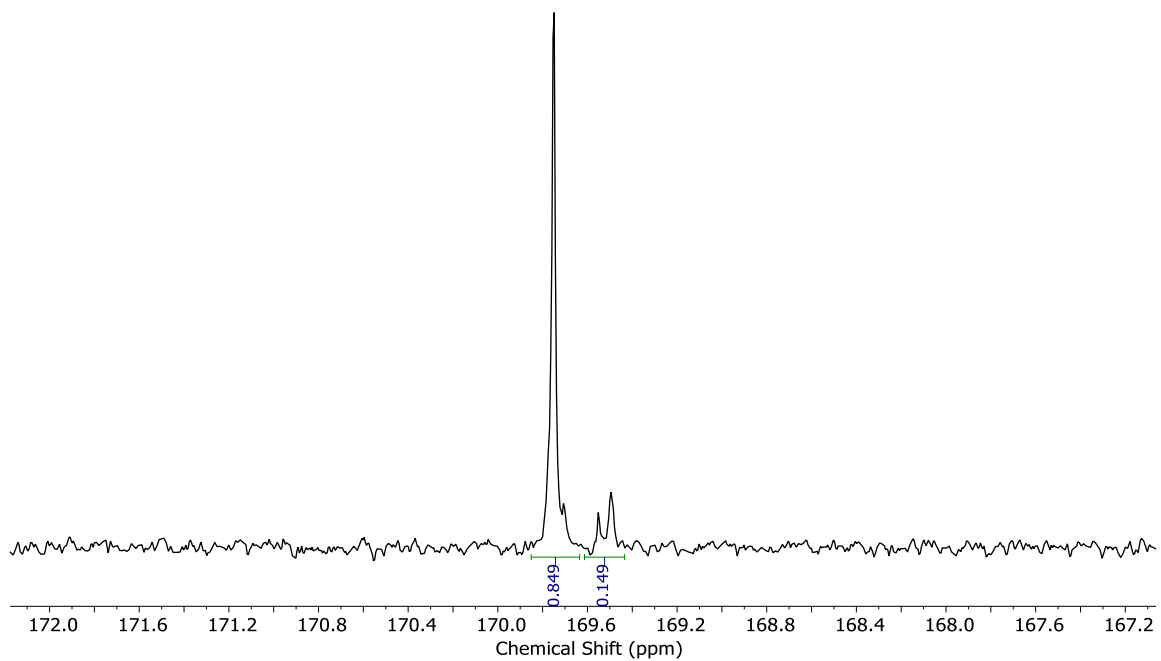


**Figure S65.**  $^{13}\text{C}\{^1\text{H}\}$  NMR spectrum, showing the carbonyl region for PLA3 in  $\text{CDCl}_3$  (prepared by complex **5**,  $[\text{LA}]:[\mathbf{5}] = 1500$ ,  $[\text{LA}] = 1 \text{ M}$ , THF, 298 K).

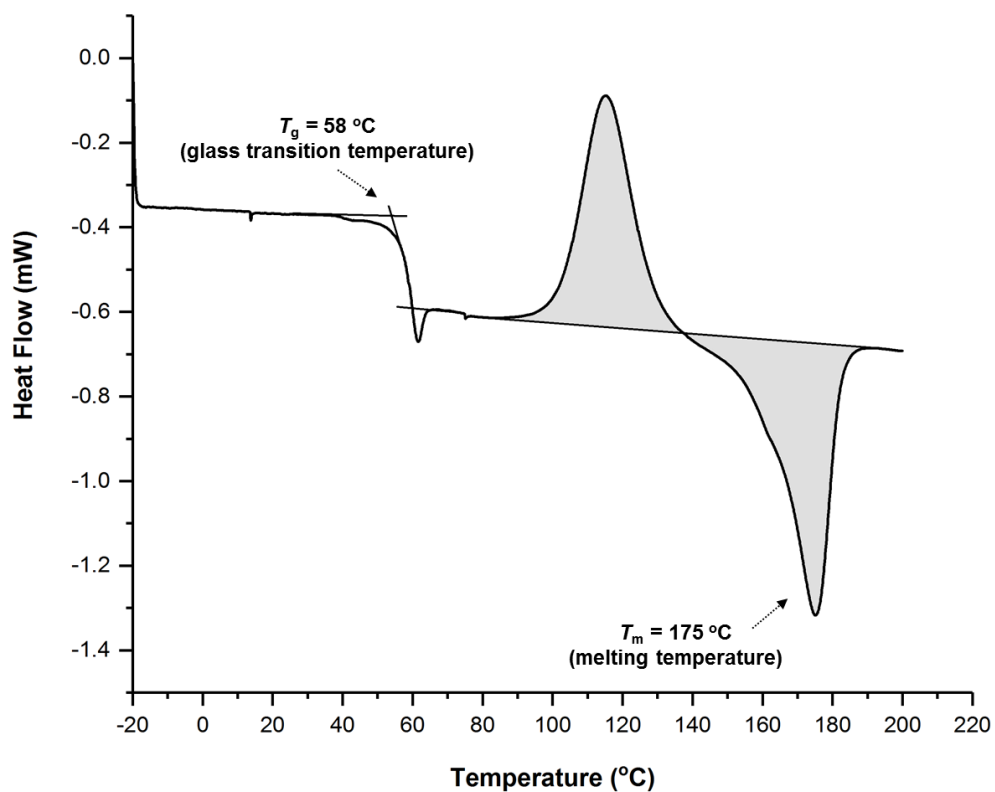


**Figure S66.** DSC thermogram of PLA prepared by complex 4 at 298 K.

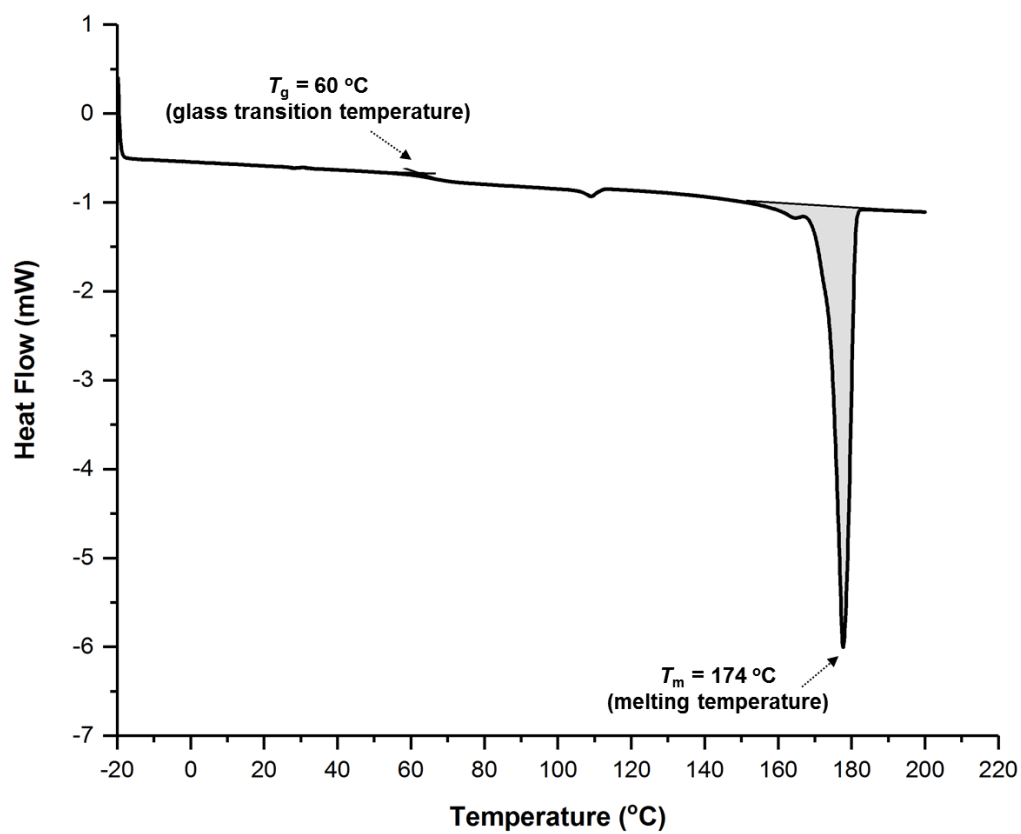


**Figure S67.** DSC thermogram of PDLA prepared by complex 4 at 298 K.

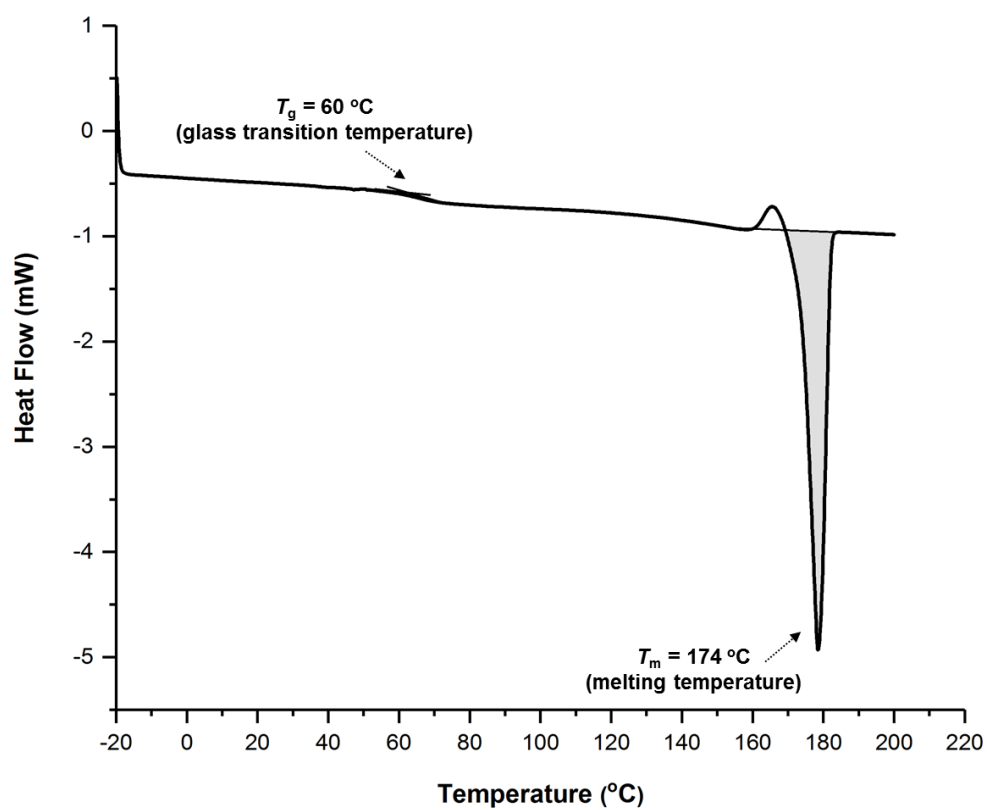


**Figure S68.** DSC thermogram of PLLA prepared by complex **4** at 298 K.

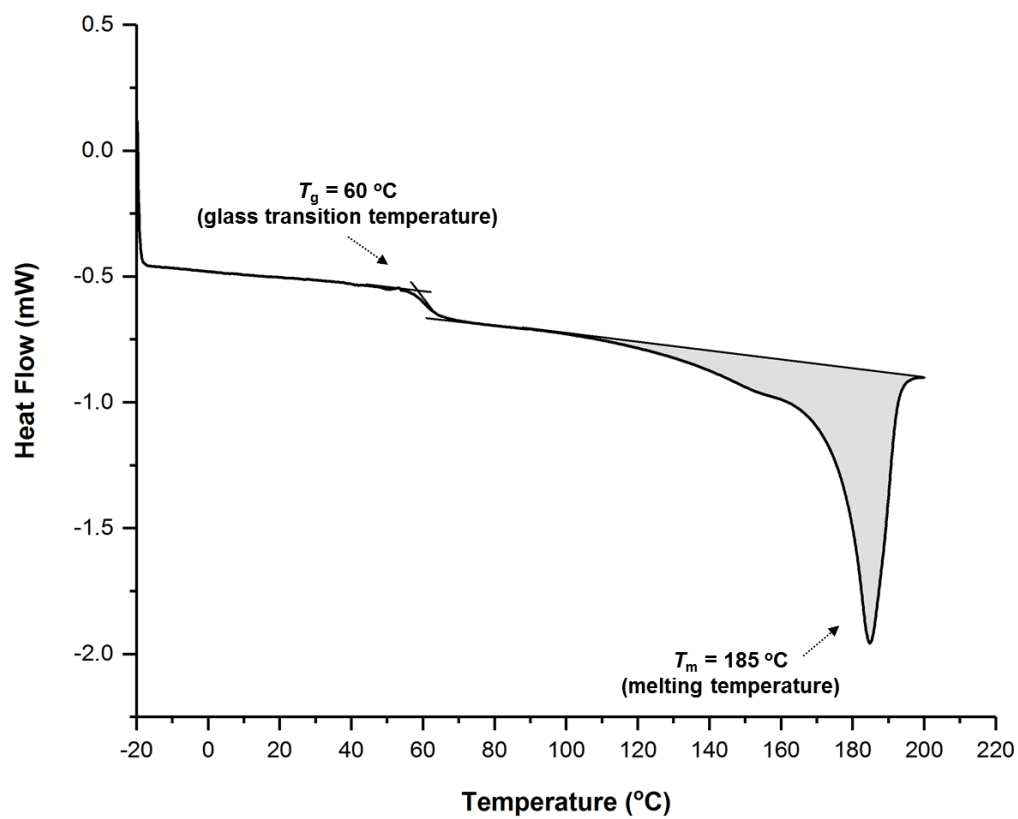


**Figure S69.** DSC thermogram of PLA prepared by complex **4** at 278 K.

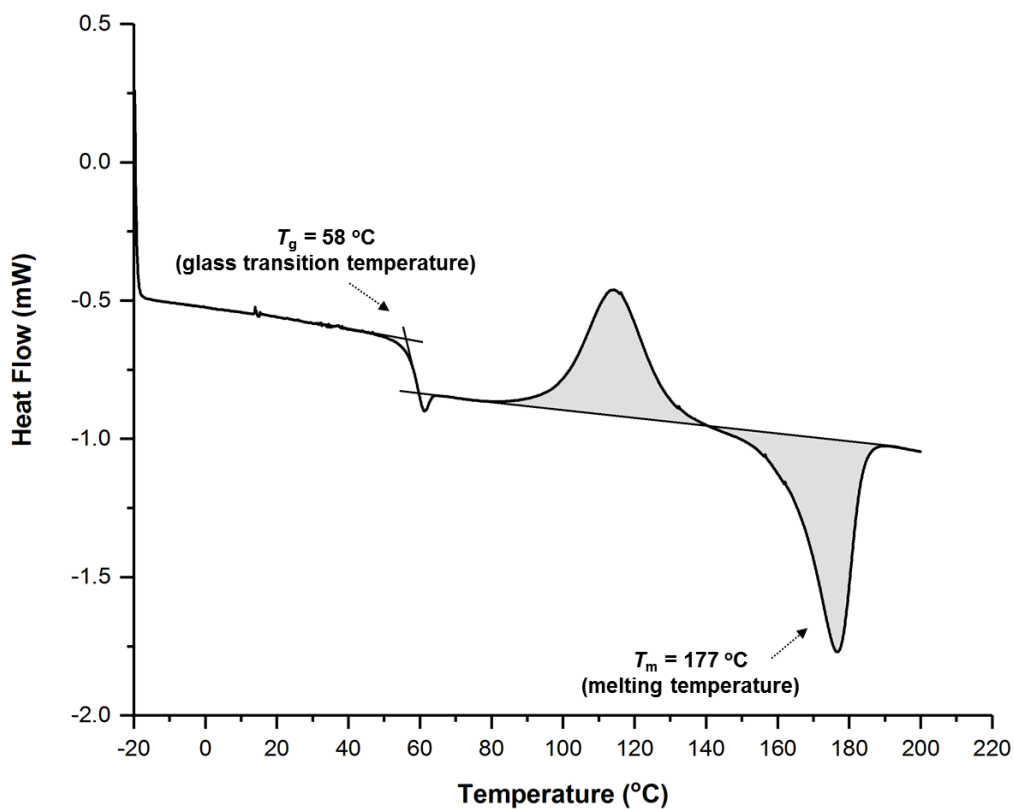


**Figure S70.** DSC thermogram of PLA prepared by complex **5** at 298 K.

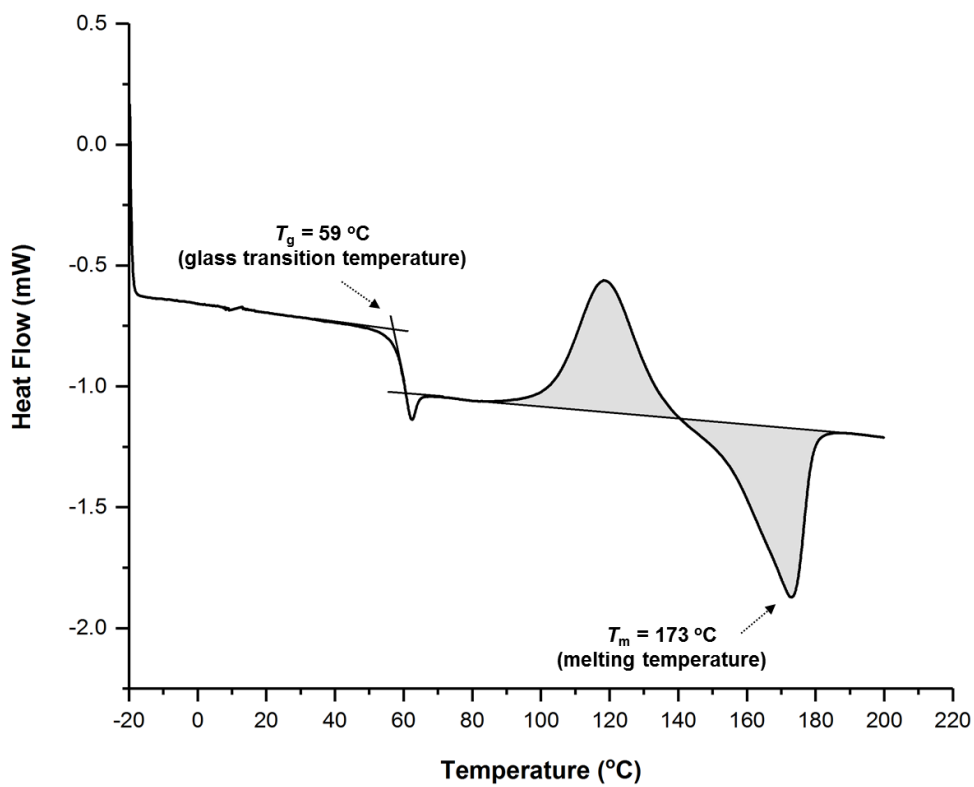


**Figure S71.** DSC thermogram of PLA prepared by complex **5** at 298 K using  $[5]:[rac-LA] = 1:1500$ .

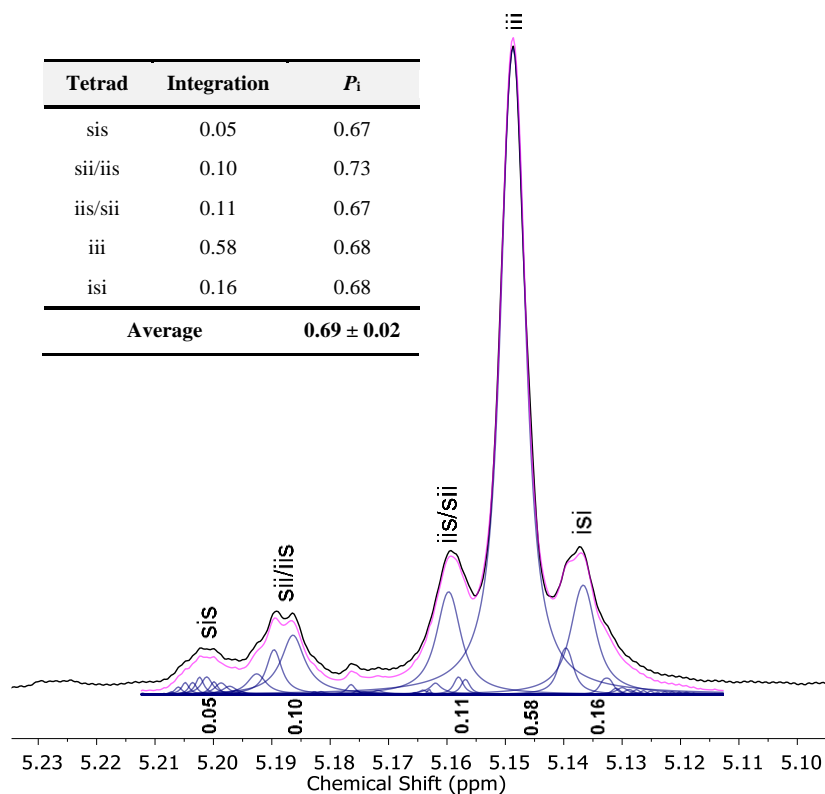


**Figure S72.**  $^1\text{H}\{^1\text{H}\}$  NMR spectrum of PLA prepared by complex **2**.  $[\text{LA}]:[\mathbf{2}] = 500$ ,  $[\text{LA}] = 1 \text{ M}$ , THF, 298 K.

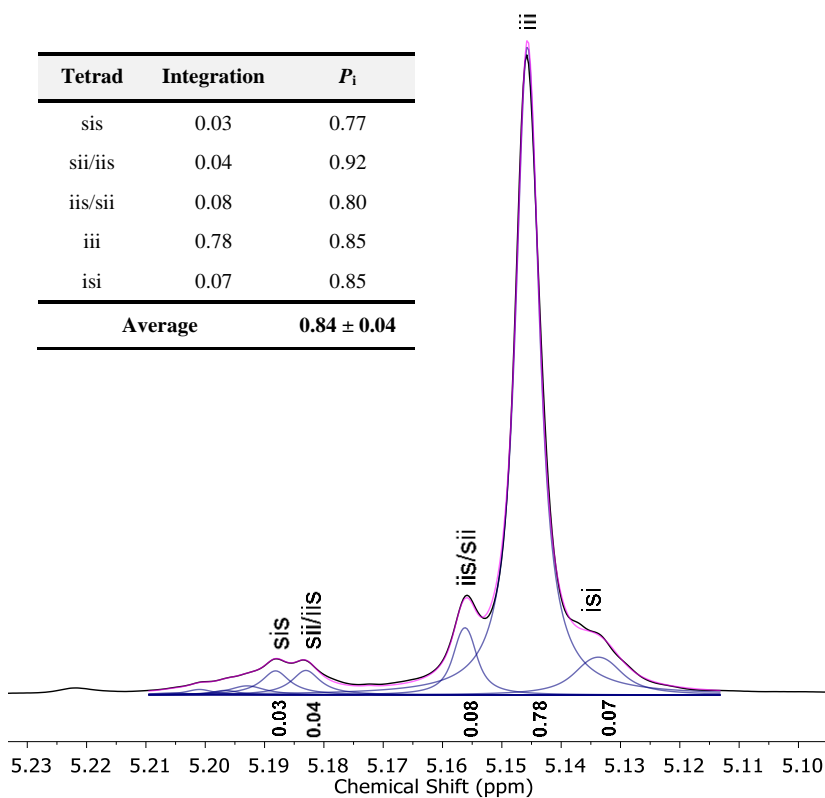


**Figure S73.**  $^1\text{H}\{^1\text{H}\}$  NMR spectrum of PLA prepared by complex **3**.  $[\text{LA}]:[\mathbf{3}] = 500$ ,  $[\text{LA}] = 1 \text{ M}$ , THF, 298 K.

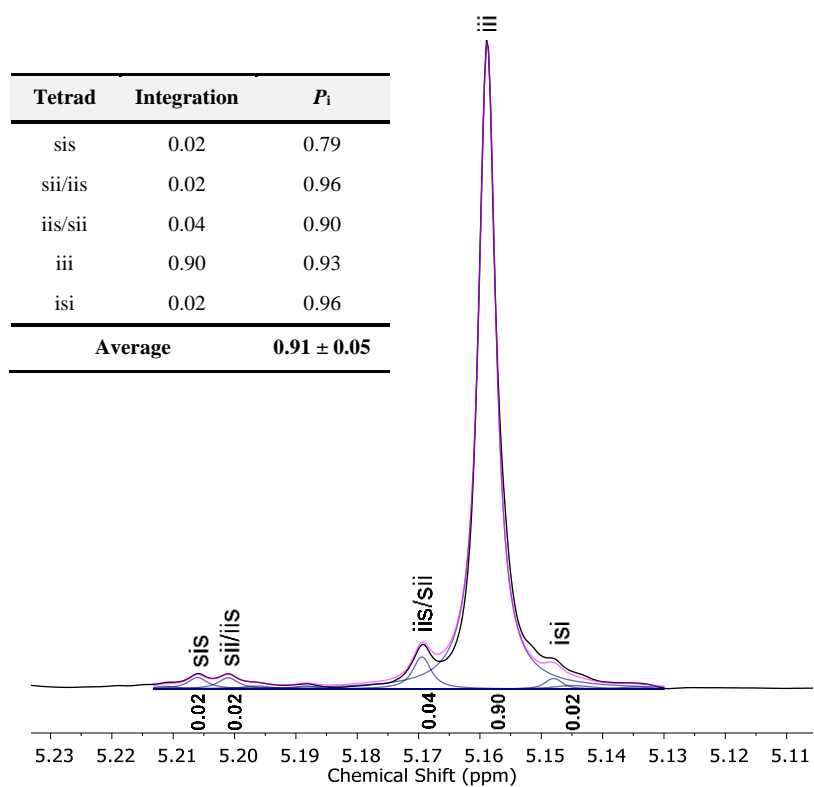


**Figure S74.**  $^1\text{H}\{^1\text{H}\}$  NMR spectrum of PLA prepared by complex **4**.  $[\text{LA}]:[\mathbf{4}] = 500$ ,  $[\text{LA}] = 1 \text{ M}$ , THF, 298 K.

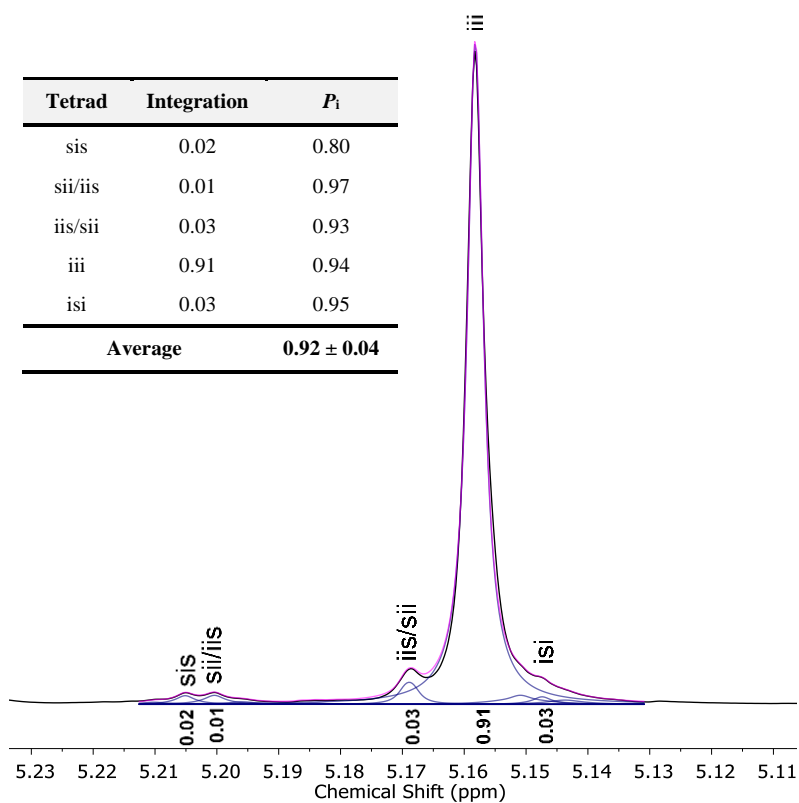


**Figure S75.**  $^1\text{H}\{^1\text{H}\}$  NMR spectrum of PLA prepared by complex **4**.  $[\text{LA}]:[\mathbf{4}] = 500$ ,  $[\text{LA}] = 1 \text{ M}$ , THF, 278 K.

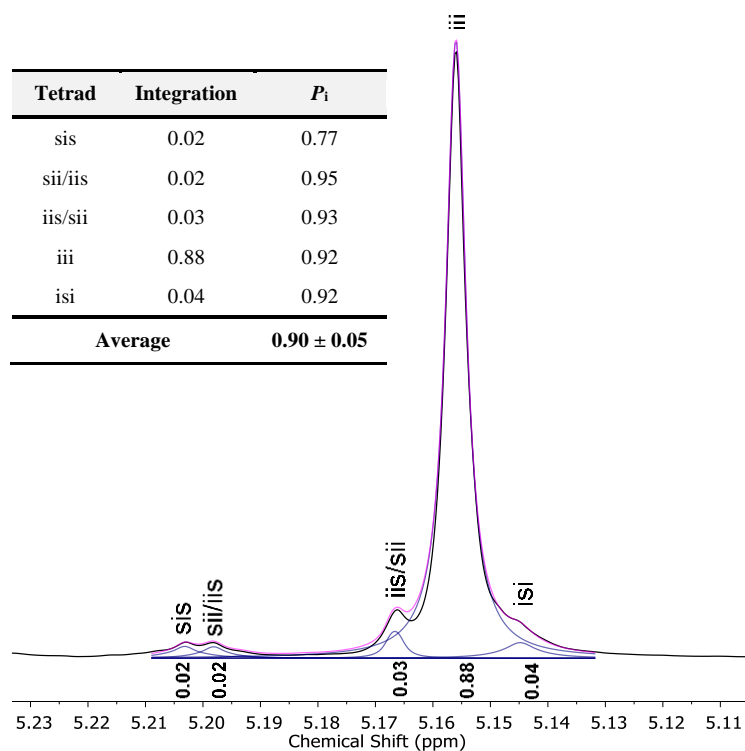


**Figure S76.**  $^1\text{H}\{^1\text{H}\}$  NMR spectrum of PLA prepared by complex **5**.  $[\text{LA}]:[\mathbf{5}] = 500$ ,  $[\text{LA}] = 1 \text{ M}$ , THF, 298 K.

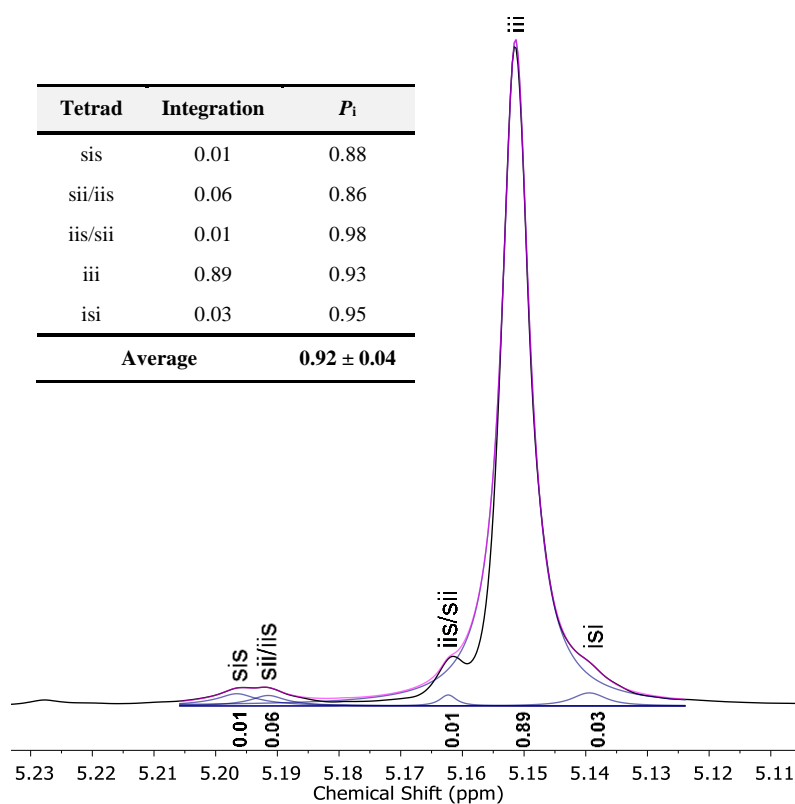


**Figure S77.**  $^1\text{H}\{^1\text{H}\}$  NMR spectrum of PLA prepared by complex **5**.  $[\text{LA}]:[\mathbf{5}] = 1500$ ,  $[\text{LA}] = 1 \text{ M}$ , THF, 298 K.

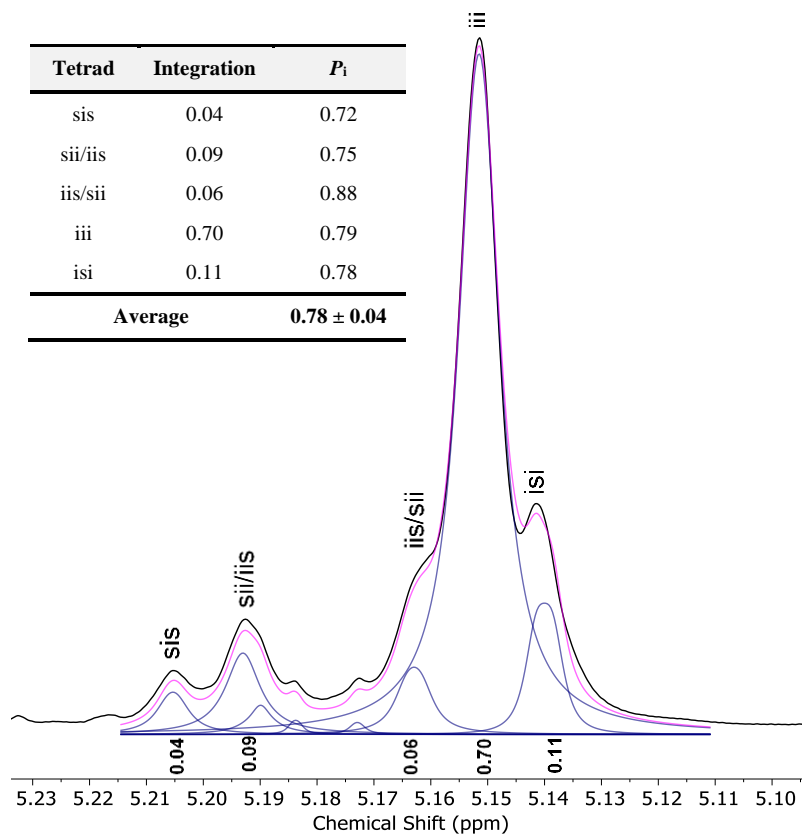


**Figure S78.**  $^1\text{H}\{^1\text{H}\}$  NMR spectrum of PLA prepared by complex **4**.  $[\text{LA}]:[\mathbf{4}] = 500$ , bulk, 403 K.

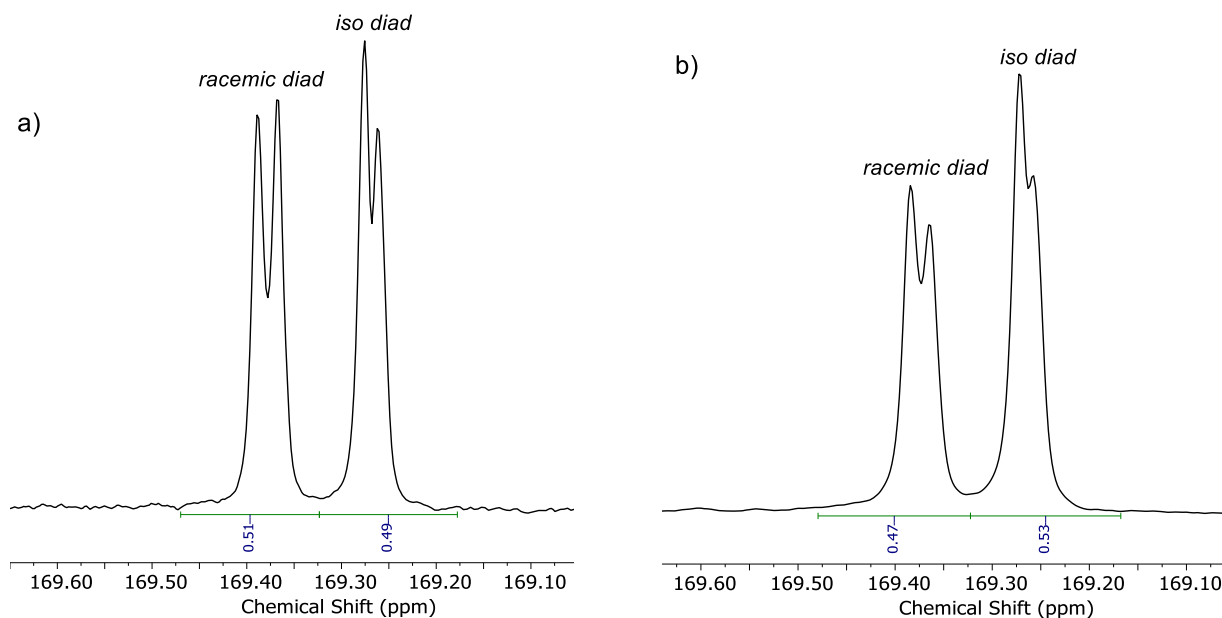


**Figure S79.** Carbonyl regions of the  $^{13}\text{C}\{^1\text{H}\}$  NMR spectra of PHB prepared by a) complex **1** and b) complex **2**.

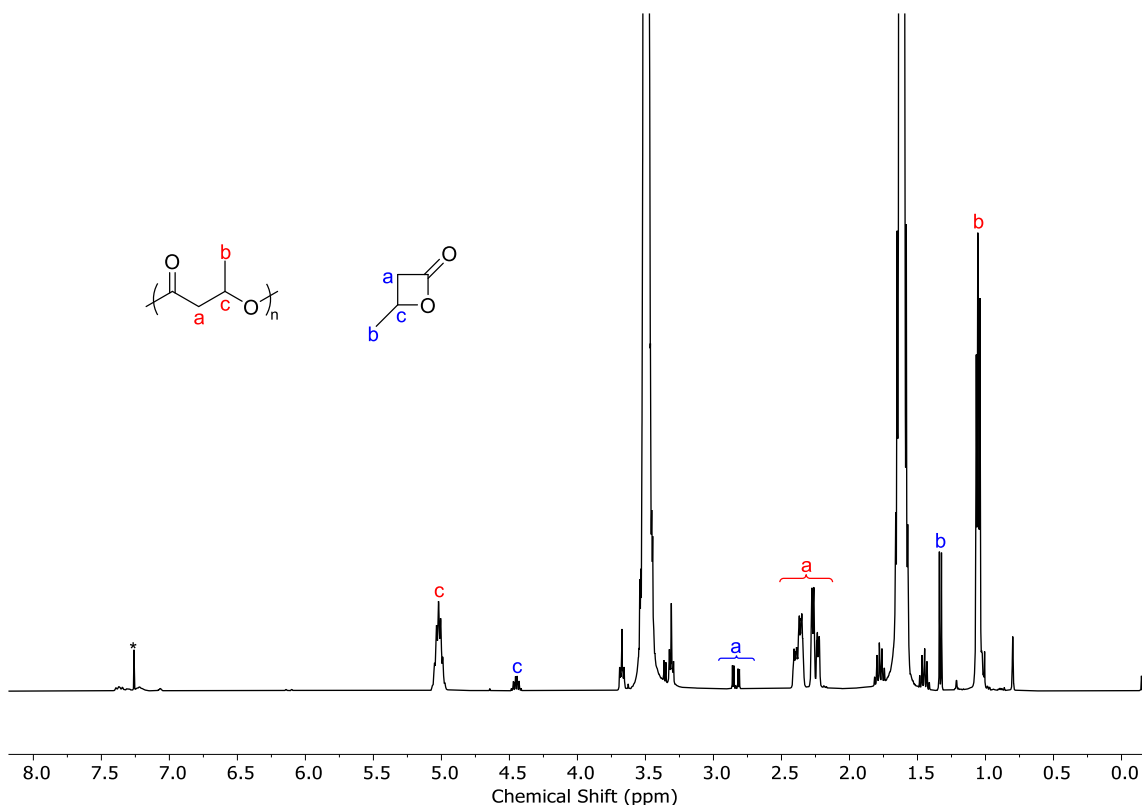


**Figure S80.**  $^1\text{H}$  NMR spectra of crude PHB, prepared by **2** in  $\text{CDCl}_3$ .

#### S4. Computational details

Density Functional theory (DFT) calculations were performed using Gaussian09 suite of codes (revision D.02). Geometries were fully optimised without any symmetry or geometry constraints. The nature of all the stationary points as minima or transition states (first-order saddle points) on the potential energy surface was verified by calculations of the vibrational frequency spectrum. Free enthalpies were calculated at 298.15 K within the harmonic approximation for vibrational frequencies.

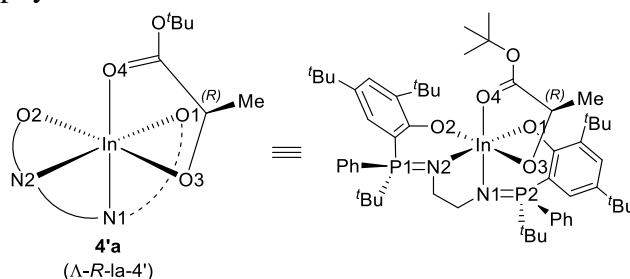
Geometry optimisations were carried out using M06-L functional. The 6-31+G(d,p) basis set was used for P, O and N atoms, 6-31G(d,p) for C and H atoms and the lanl2dz basis set and associated pseudopotential for In. Solvent effects in tetrahydrofuran were computed using the SMD continuum model.

Full coordinates for all structures, together with computed energies and vibrational frequency data, are available *via* the corresponding Gaussian 09 output files and calculation spreadsheet, stored in the open-access digital repository, DOI: 10.6084/m9.figshare.12513434.

#### Comparison of solid state molecular structure of **4'a** and DFT optimized geometry

Comparison of key bond lengths from X-ray crystallography molecular structure and the DFT optimized geometry revealed a good fit, with an average difference between X-ray data and computed lengths of <2% (Table S11).

**Table S11.** Comparison of key bond lengths for the structures of **4'a** obtained by DFT optimization and by X-ray crystallography.



Bond length (Å)	X-ray crystallography	DFT optimization	% difference
In(1)-N(1)	2.184(2)	2.163(3)	0.957
In(1)-N(2)	2.179(2)	2.208(5)	-1.345
In(1)-O(1)	2.101(2)	2.072(7)	1.356
In(1)-O(2)	2.125(2)	2.089(0)	1.703
In(1)-O(3)	2.100(2)	2.049(0)	2.438
In(1)-O(4)	2.355(2)	2.285(1)	2.976
Angle (°)			
N(1)-In(1)-N(2)	78.93(9)	78.20(3)	0.932
N(1)-In(1)-O(1)	89.14(9)	89.55(2)	-0.452
N(1)-In(1)-O(2)	107.42(9)	107.52(9)	-0.093
N(1)-In(1)-O(3)	95.7(1)	96.89(3)	-1.236
N(1)-In(1)-O(4)	169.30(9)	172.40(6)	-1.829
N(2)-In(1)-O(1)	164.01(9)	165.64(7)	-0.993
N(2)-In(1)-O(2)	84.50(9)	85.77(5)	-1.498
N(2)-In(1)-O(4)	103.19(9)	101.14(3)	1.992
O(1)-In(1)-O(2)	89.03(8)	90.89(0)	-2.080
O(1)-In(1)-O(3)	98.91(9)	96.41(5)	2.531
O(1)-In(1)-O(4)	90.51(8)	91.98(0)	-1.615
O(2)-In(1)-O(3)	155.69(9)	154.56(3)	0.730
O(2)-In(1)-O(4)	83.27(8)	79.89(1)	4.067
O(3)-In(1)-O(4)	73.77(9)	75.54(6)	-2.395

Isolated lactate complex **4'a** provides a model for the propagating alkoxide species during polymerization. However, there are multiple alternative isomers of **4'a** which were not isolated. These putative structures were examined by DFT in order to select the appropriate starting point(s) for the modelling of polymerization propagation.

### Isomerism at the phosphorus atoms for model propagating alkoxide species **4'a**

In the structure isolated experimentally, the phosphasalen ligand displays *R*, *S* stereochemistry at the phosphorus atoms. Assuming the phosphasalen would remain coordinated in a *cis*  $\beta$  fashion, hypothetical structures bearing *S,S* (**4'a $\alpha$** ), *R,R* (**4'a $\beta$** ) and *S*, *R* (**4'a $\gamma$** ) stereochemistry at the

phosphorus were optimised by DFT and their relative free enthalpies compared (Fig. S81). In conjunction with the selective formation of the *R,S/S,R* ligand diastereoisomeric pair experimentally, the *R,S* geometry proved to be the lowest in energy.

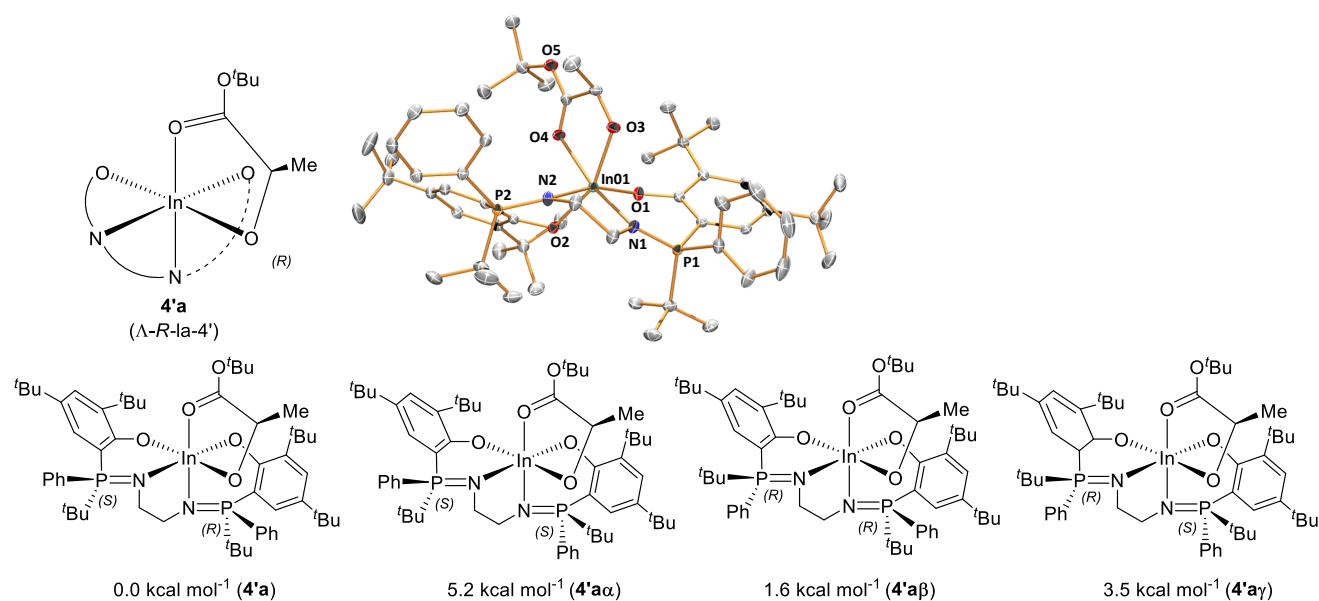


**Figure S81.** Structures of the different possible isomers of **4'a** depending on the stereochemistry at the phosphorus atoms and their relative free enthalpies calculated by DFT.

#### *Cis-trans* isomerism of the lactate ligand for model propagating alkoxide species **4'a**

In the structure obtained by X-ray crystallography, the *tert*-butyl lactate ligand is bidentate with the alkoxide moiety in *trans* to one of the phenoxides of the phosphasalene ligand. Assuming the phosphasalene ligand remains coordinated in a *cis*  $\beta$  fashion, a hypothetical structure with the alkoxide moiety *cis* to both phenoxide moieties and *trans* to one iminophosphorane (**4'aδ**) was optimised by DFT and its relative free enthalpy compared to that of **4'a** (Fig. S82). The *trans* geometry isolated experimentally had the lowest energy.

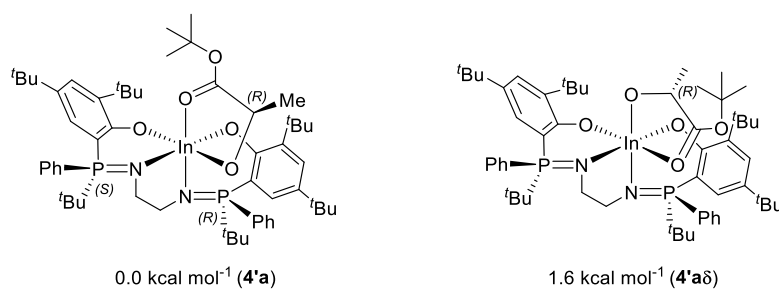


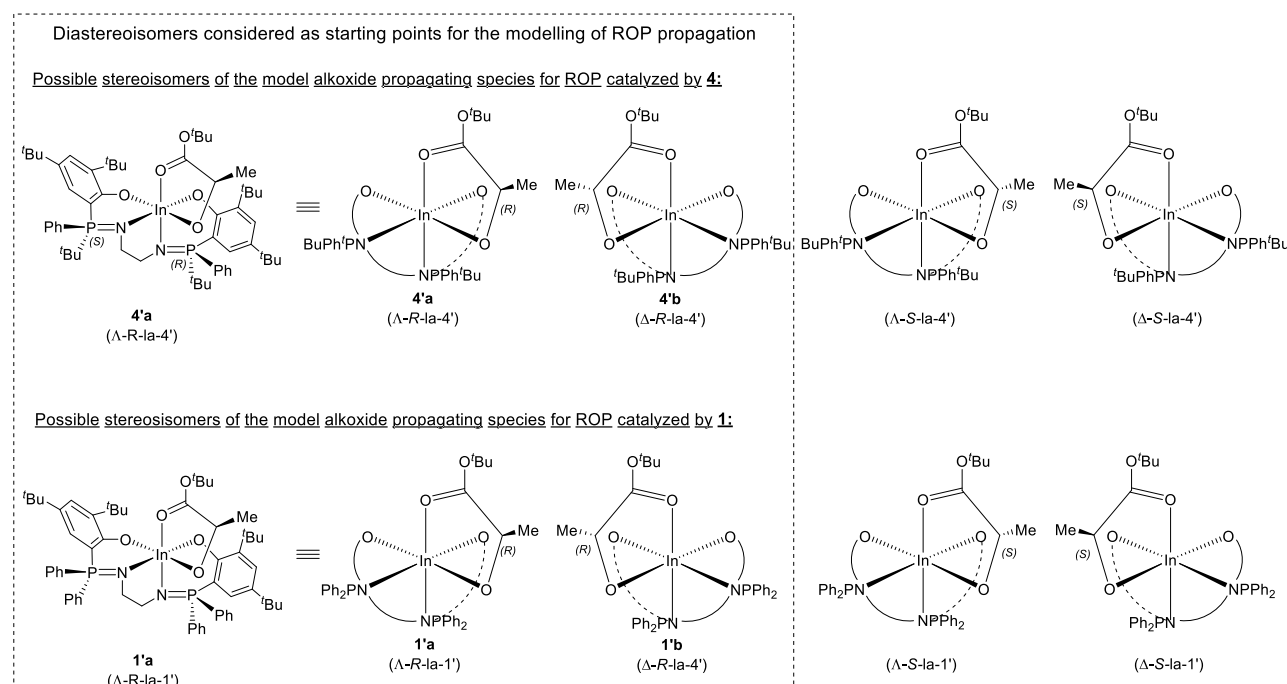
**Figure S82.** Structures of the different possible isomers of **4'a** depending on the coordination mode of the lactate ligand, and their relative free enthalpies calculated by DFT.

**Table S12.** Computed Gibbs free energy for **4'a**, **4'a $\alpha$** , **4'a $\beta$** , **4'a $\gamma$**  and **4'a $\delta$** .

	<b>4a</b>	<b>4'a<math>\alpha</math></b>	<b>4'a<math>\beta</math></b>	<b>4'a<math>\gamma</math></b>	<b>4'a<math>\delta</math></b>
G (Hartree)	-3392.146460	-3392.140075	-3392.145864	-3392.142808	-3392.145900

**Stereoisomers of 4'a arising from the coordination mode of the phosphasalen ligand and from the stereochemistry of the lactate ligand.**

**4'a** represents a model structure for the propagating alkoxide species during polymerization. However, based on the molecular structure of **4'a** revealed by X-ray crystallography, the tetradentate phosphasalen coordination mode ( $\Lambda$  vs  $\Delta$ ) and the lactate stereochemistry ( $R$  vs  $S$ ) give rise to two pairs of diastereoisomers, namely  $\Lambda$ - $R$ -la-4' (**4'a**) and  $\Delta$ - $R$ -la-4' (**4'b**), as well as  $\Lambda$ - $S$ -la-4' and  $\Delta$ - $S$ -la-4' (Fig. S83). Assuming that enantiomers should result in similar potential energy surfaces, only a single diastereotopic pair, **4'a**, and **4'b** was considered.

**Analogue 1'a and 1'b "Ph<sub>2</sub>P" models for the propagating alkoxide species during polymerization initiated by 1.****Figure S83.** Possible stereoisomers of the model alkoxide propagating species for ROP catalyzed by **4** and by **1**, and diastereotopic pairs considered in the DFT study.

To investigate the enhanced isoselectivity of **4** over **1**, hypothetical analogous diphenyl phosphasalen lactate complexes **1'a** and **1'b** were also considered as starting points for the modelling of polymerization propagation by **1**, assuming that the phosphasalen ligand coordinates in a similar  $cis\beta$  fashion and that coordination of the lactate is bidendate with the alkoxide moiety *trans* to one of the phenoxides of the phosphasalen ligand

## Alternative pathways per monomer opening event for 4'a, 4'b, 1'a and 1'b, depending on the initial coordination of a lactide molecule and its stereochemistry

For each lactate complex and a given LA enantiomer, assuming that the phosphasalén ligand remains coordinated in a *cis*  $\beta$  fashion, four pathways were determined per monomer ring-opening, depending on the initial coordination of the lactide molecule. The LA carbonyl can be disposed *trans* or *cis* to the phenoxide of the phosphasalén ligand, with either the *re* or *si* faces of the lactide facing the alkoxide ligand (which models the growing polymer chain). Figure S84 depicts the sixteen possibilities arising from the coordination of *D* or *L*-LA to 4'a or 4'b. Similarly, there are sixteen possibilities arising from the coordination of *D* or *L*-LA to 1'a or 1'b.

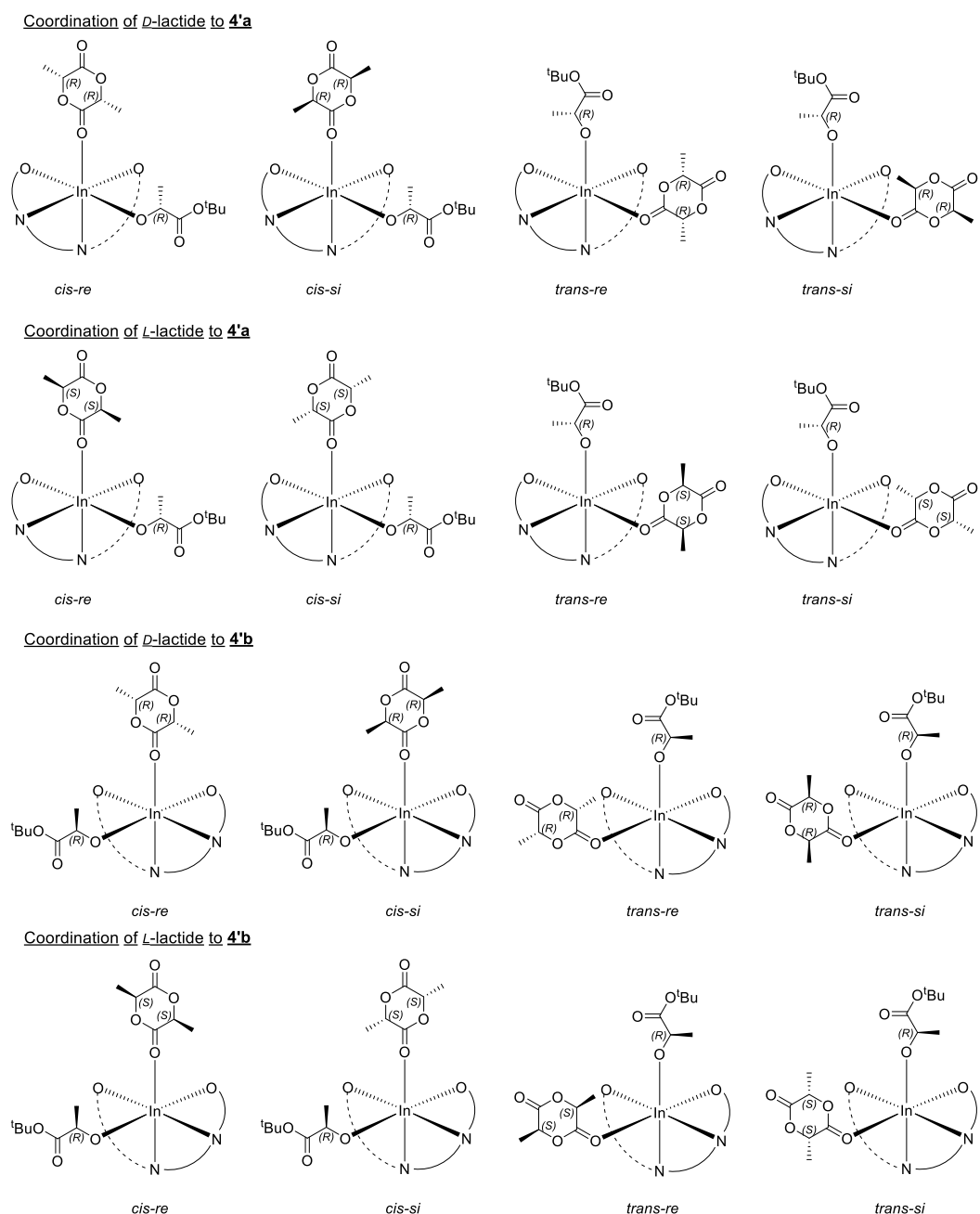


**Figure S84.** Possible coordination modes of *D* and *L*-LA to 4'a and 4'b, resulting in sixteen alternative pathways for ring-opening (ligand structure simplified as per Figures S81–S83).

## Lactide ring-opening transition states modelling for 4'a, 4'b, 1'a and 1'b

### Initial investigation using M06-L functional

For each lactide ring-opening event, two transition states were considered: TS<sub>I-II</sub>: the nucleophilic attack of the lactide carbonyl by the indium alkoxide TS<sub>II-III</sub>: the subsequent ring-opening of a quaternary intermediate to yield a new propagating alkoxide species.

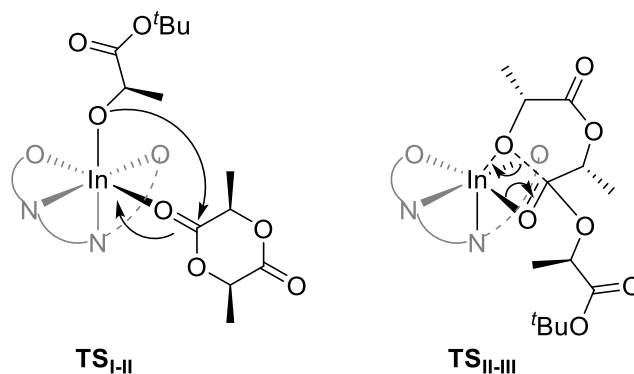


**Figure S85.** Schematics of exemplar transition states TS<sub>I-II</sub> and TS<sub>II-III</sub> (4'a/*D*-LA/*trans-si* pathway).

Based on the alternative pathways identified above for the ring-opening of *rac*-LA by 4'a, 4'b, 1'a and 1'b, a total of sixty-four transition states were optimised using the M06-L functional (their unique imaginary frequency values correspond to the intended reactions). Their free enthalpies ( $\Delta G$ ) were calculated against the sum of the free enthalpies of isolated lactide and the relevant starting lactate complex (Table S13).

For each complex, the isotactic preference was defined and calculated as the difference between the lowest activation barriers found for isotactic or heterotactic ring-opening pathways, respectively ( $\Delta\Delta G^\ddagger_{\text{isotactic}} - \Delta\Delta G^\ddagger_{\text{heterotactic}}$ ).

**Table S13.** Free enthalpy barriers to transition states for the isotactic or heterotactic ring-opening of LA by *D*-lactate complexes **4'a**, **4'b**, **1'a** and **1'b** (kcal mol<sup>-1</sup>)

Catalyst 4 ( <i>t</i> BuPhP phosphasalen)					Catalyst 1 (Ph <sub>2</sub> P phosphasalen)			
<i>D</i> -lactate model	<b>4'a</b>		<b>4'b</b>		<b>1'a</b>		<b>1'b</b>	
Transition State	TS <sub>I-II</sub>	TS <sub>II-III</sub>	TS <sub>I-II</sub>	TS <sub>II-III</sub>	TS <sub>I-II</sub>	TS <sub>II-III</sub>	TS <sub>I-II</sub>	TS <sub>II-III</sub>
ROP of <i>D</i> -LA (isotactic polymerisation)								
<i>cis-re</i> pathway	+31.3	+28.6	+20.1	+32.5	+29.5	+25.4	+15.6	+21.8
<i>cis-si</i> pathway	+31.3	+27.3	+27.2	+29.4	+27.9	+26.8	+23.7	+23.5
<i>trans-re</i> pathway	+22.0	+24.1	+25.9	+21.1	+26.5	+23.7	+21.4	+23.2
<i>trans-si</i> pathway	+28.7	+28.7	+23.4	+22.6	+30.0	+28.0	+22.1	+17.7
<i>Most favoured isotactic pathway</i>	<i>trans-re</i>		<i>trans-si</i>		<i>trans-re</i>		<i>cis-re</i>	
ROP of <i>L</i> -LA (heterotactic polymerisation)								
<i>cis-re</i> pathway	+17.8	+29.5	+33.6	+31.1	+16.8	+27.6	+27.7	+25.5
<i>cis-si</i> pathway	+27.6	+13.9	+29.9	+14.1	+25.9	+13.9	+16.7	+10.3
<i>trans-re</i> pathway	+29.3	+22.2	+30.6	+27.0	+28.7	+26.8	+29.2	+25.2
<i>trans-si</i> pathway	+23.2	+29.2	+23.2	+31.5	+24.0	+30.3	+20.3	+34.2
<i>Most favoured heterotactic pathway</i>	<i>cis-si</i>		<i>cis-si</i>		<i>cis-si</i>		<i>cis-si</i>	
$\Delta\Delta G^\ddagger_{\text{isotactic}}$	+24.1		+23.4		+26.5		+21.8	
$\Delta\Delta G^\ddagger_{\text{heterotactic}}$	+27.6		+29.9		+25.9		+16.7	
Isotactic preference ( $\Delta\Delta G^\ddagger_{\text{isotactic}} - \Delta\Delta G^\ddagger_{\text{heterotactic}}$ )	-3.5		-6.5		+0.6		+5.1	

**Table S14.** Computed Free Gibbs Energy for *D*-lactide, *L*-Lactide, **4'a**, **4'b**, **1'a** and **1'b**.

Structure	M06L G (Hartree)	PBE0 G (Hartree)	$\omega$ B97XD G (Hartree)
<i>D</i> -lactide	-534.2220890	-533.7058080	-534.1176740
<i>L</i> -lactide	-534.2215030	-533.7056380	-534.1178450
<b>4'a</b>	-3392.146460	-3389.170944	-3391.716928
<b>4'b</b>	-3392.148424	-3389.171834	-3391.717843
<b>1'a</b>	-3539.811262	-3536.683764	-539.3143620
<b>1'b</b>	-3539.806695	-3536.682791	-3539.313871

Calculations were performed using the specified functional with basis set 6-31+G(d,p) for N, P and O atoms, 6-31G(d,p) for C and H atoms, and basis sets and pseudo potential lanl2dz for In atoms. Solvent effects were modelled SMD continuum model for THF at 298 K.

**Table S15.** Computed Free Gibbs Energy for the isotactic or heterotactic ring-opening of LA by *D*-lactate complexes **4'a**, **4'b**, **1'a** and **1'b** (Hartree).

Catalyst 4 ('BuPhP phosphasalen)					Catalyst 1 (Ph <sub>2</sub> P phosphasalen)			
<i>D</i> -lactate model	4'a		4'b		1'a		1'b	
Transition State	TS <sub>I-II</sub>	TS <sub>II-III</sub>	TS <sub>I-II</sub>	TS <sub>II-III</sub>	TS <sub>I-II</sub>	TS <sub>II-III</sub>	TS <sub>I-II</sub>	TS <sub>II-III</sub>
ROP of <i>D</i> -LA (isotactic polymerisation)								
<i>cis-re</i> pathway	-3926.320555	-3926.324962	-3926.337412	-3926.337412	-4073.986374	-4073.992802	-4074.003894	-4073.994060
<i>cis-si</i> pathway	-3926.318662	-3926.325062	-3926.326132	-3926.326132	-4073.988811	-4073.990688	-4073.990963	-4073.991251
<i>trans-re</i> pathway	-3926.333537	-3926.330154	-3926.328129	-3926.328129	-4073.991103	-4073.995522	-4073.994695	-4073.991885
<i>trans-si</i> pathway	-3926.324697	-3926.324701	-3926.332096	-3926.332096	-4073.985575	-4073.988781	-4073.993541	-4074.000513
ROP of <i>L</i> -LA (heterotactic polymerisation)								
<i>cis-re</i> pathway	-3926.341534	-3926.322966	-3926.315240	-3926.319260	-4074.005920	-4073.988761	-4073.984098	-4073.987537
<i>cis-si</i> pathway	-3926.323997	-3926.345797	-3926.321230	-3926.346347	-4073.991471	-4074.010617	-4074.001662	-4074.011841
<i>trans-re</i> pathway	-3926.321226	-3926.332645	-3926.320130	-3926.320130	-4073.987047	-4073.990006	-4073.981689	-4073.988117
<i>trans-si</i> pathway	-3926.332987	-3926.323367	-3926.331937	-3926.331937	-4073.994567	-4073.984558	-4073.995858	-4073.973701

## **Functional benchmarking for selected pathways**

Transition states for the lowest free enthalpy pathways identified above were re-optimised and their free enthalpies re-calculated with the PBE0 (augmented with Grimme's empirical dispersion D3) and  $\omega$ B97XD functionals (same basis sets and solvent model as with M06-L, *vide supra*). Geometries were also optimised for the lactide coordination complex, I, to confirm the nature of the lowest energy intermediate for all pathways.

Free enthalpies ( $\Delta G$ ) were referenced against the sum of the free enthalpies of isolated lactide and the relevant starting lactate complex (Tables S16-17).

For each complex, the isotactic preference was defined and calculated as the difference between the lowest activation barriers found in isotactic or heterotactic ring-opening pathways, respectively ( $\Delta\Delta G^\ddagger_{\text{isotactic}} - \Delta\Delta G^\ddagger_{\text{heterotactic}}$ ).

**Table S16.** Functional benchmarking of computed Free Gibbs Energy for isotactic and heterotactic ring-opening of LA by *D*-lactate complexes **4'a**, **4'b**, **1'a** and **1'b** (Hartree).

Catalyst 4 ('BuPhP phosphasalen)					Catalyst 1 (Ph <sub>2</sub> P phosphasalen)			
<i>D</i> -lactate model	4'a		4'b		1'a		1'b	
Transition State	TS <sub>I-II</sub>	TS <sub>II-III</sub>	TS <sub>I-II</sub>	TS <sub>II-III</sub>	TS <sub>I-II</sub>	TS <sub>II-III</sub>	TS <sub>I-II</sub>	TS <sub>II-III</sub>
ROP of <i>D</i> -LA (isotactic)								
M06-L-D3	-3926.333537	-3926.330154	-3926.332096	-3926.333363	-4073.991103	-4073.995522	-4074.003894	-4073.994060
PBE0-D3	-3922.843886	-3922.842525	-3922.848475	-3922.844050	-4070.351135	-4070.356452	-4070.356251	-4070.359097
ωB97XD	-3925.798922	-3925.800242	-3925.804620	-3925.804077	-4073.391714	-4073.400425	-4073.397405	-4073.398772
ROP of <i>L</i> -LA (heterotactic)								
M06-L-D3	-3926.323997	-3926.345797	-3926.321230	-3926.346347	-4073.991471	-4074.010617	-4074.001662	-4074.011841
PBE0-D3	-3922.825690	-3922.856650	-3922.837148	-3922.853000	-4070.346904	-4070.373349	-4070.357027	-4070.370063
ωB97XD	-3925.783574	-3925.815509	-3925.793607	-3925.812631	-4073.390234	-4073.414437	-4073.398394	-4073.415048

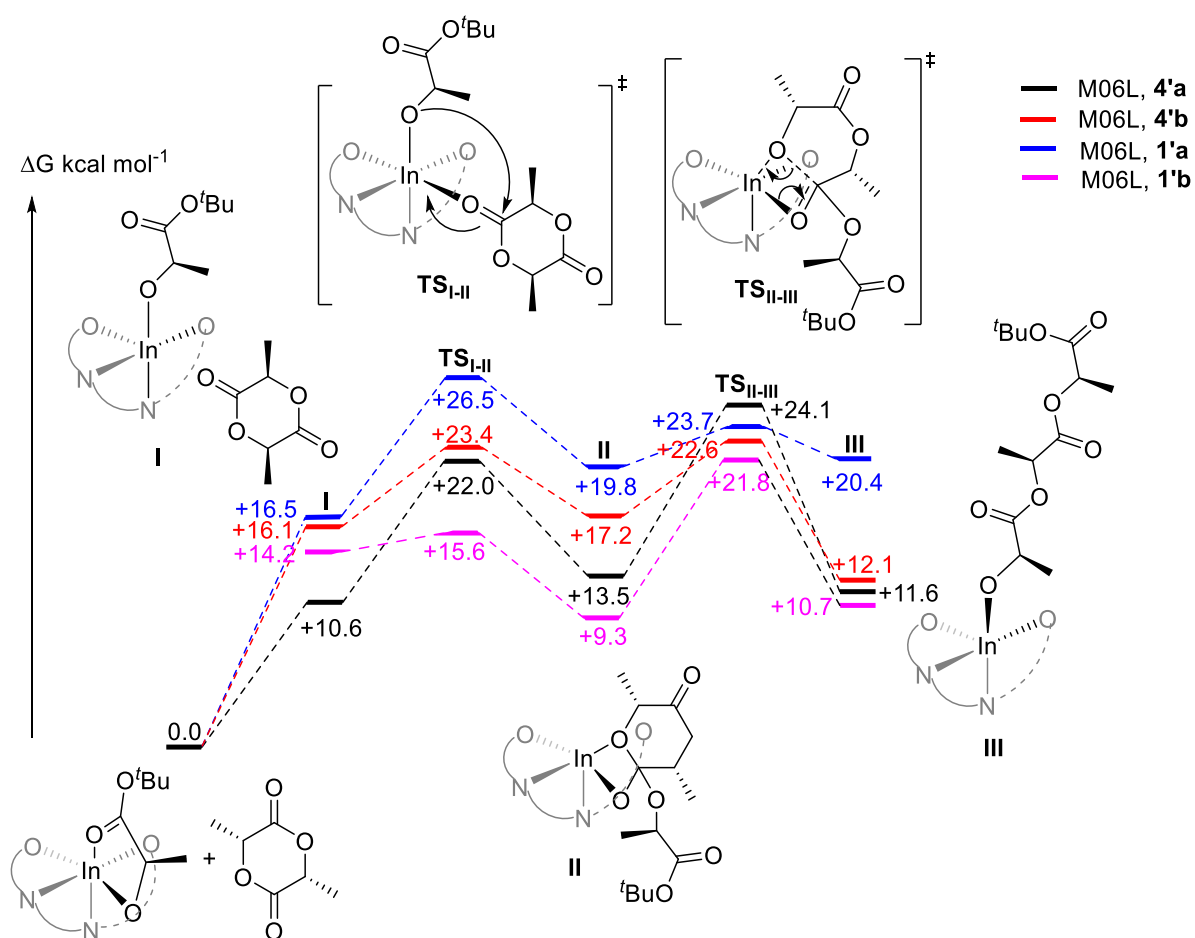
**Table S17.** Computed Free Gibbs Energy of lactide-coordination complexes **I** for all pathways and their  $\Delta G$  relative to **4'a**, **4'b**, **1'a** and **1'b** and LA.

<i>D</i> -lactate model	Catalyst 4 ('BuPhP phosphasalen)				Catalyst 1 (Ph <sub>2</sub> P phosphasalen)			
	<b>4'a</b>		<b>4'b</b>		<b>1'a</b>		<b>1'b</b>	
Intermediate	<b>I</b> (hartree)	$\Delta G$ (kcal mol <sup>-1</sup> )	<b>I</b> (hartree)	$\Delta G$ (kcal mol <sup>-1</sup> )	<b>I</b> (hartree)	$\Delta G$ (kcal mol <sup>-1</sup> )	<b>I</b> (hartree)	$\Delta G$ (kcal mol <sup>-1</sup> )
ROP of <i>D</i> -LA (isotactic)								
M06-L-D3	-3926.351672	+10.6	-3926.343808	+16.1	-4074.007018	+16.5	-4074.006115	+14.2
PBE0-D3	-3922.860962	+9.9	-3922.862026	+9.8	-4070.372406	+10.8	-4070.390578	-1.2
$\omega$ B97XD	-3925.815150	+12.2	-3925.822794	+8.0	-4073.411187	+13.1	-4073.437503	-3.7
ROP of <i>L</i> -LA (heterotactic)								
M06-L-D3	-3926.348890	+12.0	-3926.356037	+8.0	-4074.013036	+12.4	-4074.006825	+13.4
PBE0-D3	-3922.858268	+11.5	-3922.865498	+7.5	-4070.371259	+11.4	-4070.366283	+13.9
$\omega$ B97XD	-3925.811278	+14.7	-3925.826357	+5.7	-4073.411304	+13.1	-4073.406925	+15.6

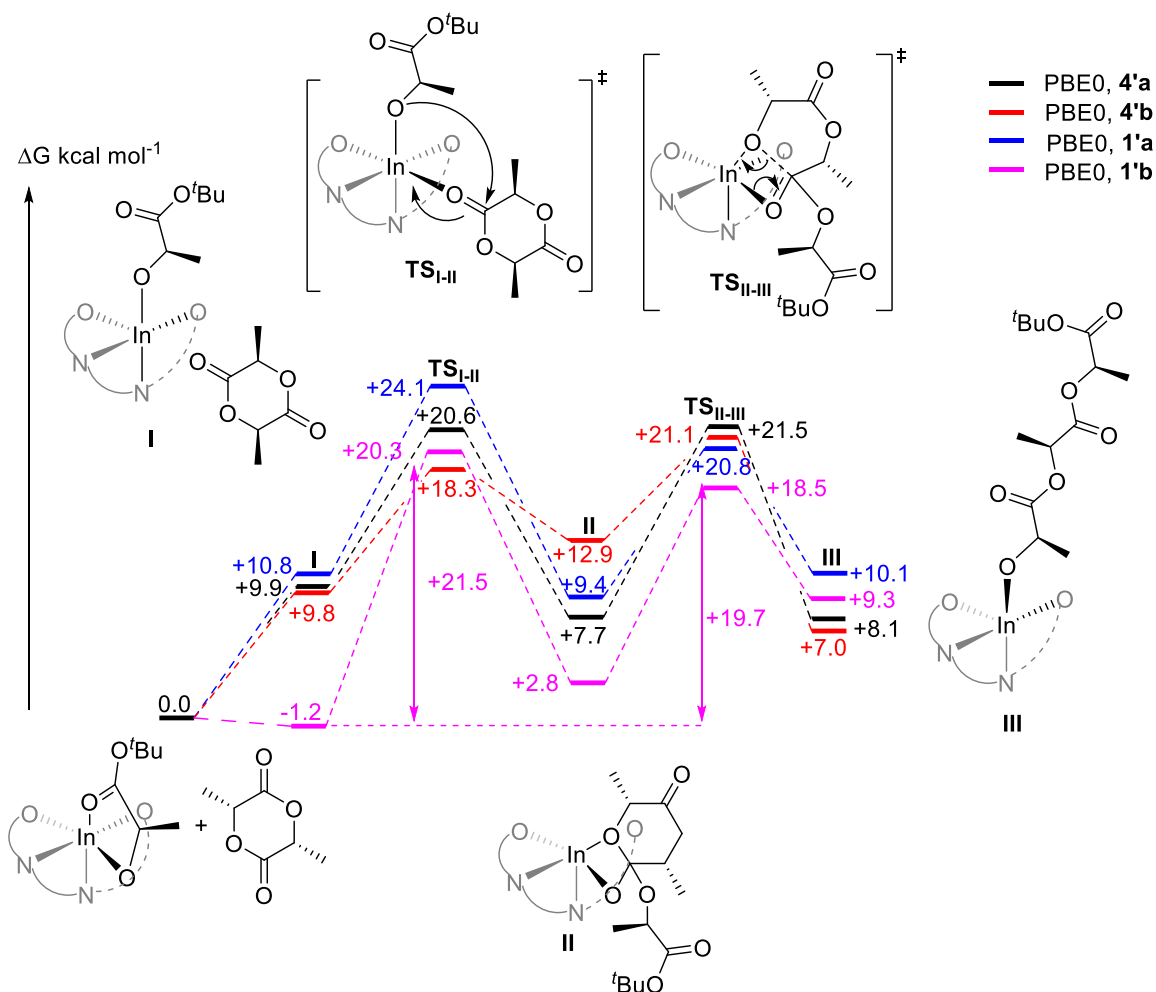
**Table S18.** Functional benchmarking of free enthalpy barriers to transition states for the isotactic or heterotactic ring-opening of LA by *D*-lactate complexes **4'a**, **4'b**, **1'a** and **1'b** (kcal mol<sup>-1</sup>; referenced to sum of the free enthalpies of isolated lactide and the relevant starting lactate complex or to free enthalpy of **I**, whichever is the lowest).

<i>D</i> -lactate model	Catalyst 4 ('BuPhP phosphasalen)				Catalyst 1 (Ph <sub>2</sub> P phosphasalen)			
	4'a		4'b		1'a		1'b	
Transition State	TS <sub>I-II</sub>	TS <sub>II-III</sub>	TS <sub>I-II</sub>	TS <sub>II-III</sub>	TS <sub>I-II</sub>	TS <sub>II-III</sub>	TS <sub>I-II</sub>	TS <sub>II-III</sub>
<u>ROP of <i>D</i>-LA</u> (isotactic)	<i>trans-re</i> pathway		<i>trans-si</i> pathway		<i>trans-re</i> pathway		<i>cis-re</i> pathway	
M06-L-D3	+22.0	+24.1	+23.4	+22.6	+26.5	+23.7	+15.6	+21.8
PBE0-D3	+20.6	+21.5	+18.3	+21.1	+24.1	+20.8	+21.5	+19.7
ωB97XD	+22.4	+21.6	+19.4	+19.7	+25.3	+19.8	+25.1	+24.3
<u>ROP of <i>L</i>-LA</u> (heterotactic)	<i>cis-si</i> pathway		<i>cis-si</i> pathway		<i>cis-si</i> pathway		<i>cis-si</i> pathway	
M06-L-D3	+27.6	+13.9	+29.9	+14.1	+25.9	+13.9	+16.5	+10.3
PBE0-D3	+31.9	+12.5	+25.3	+15.4	+26.7	+10.1	+19.7	+11.5
ωB97XD	+32.1	+12.1	+26.3	+14.4	+26.4	+11.2	+20.9	+10.5
<u>Isotactic preference</u> ( $\Delta\Delta G^\ddagger_{\text{isotactic}} - \Delta\Delta G^\ddagger_{\text{heterotactic}}$ )								
M06-L-D3	-3.5		-6.5		+0.6		+5.1	
PBE0-D3	-10.4		-4.2		-2.6		+1.8	
ωB97XD	-9.7		-6.6		-1.1		+4.2	

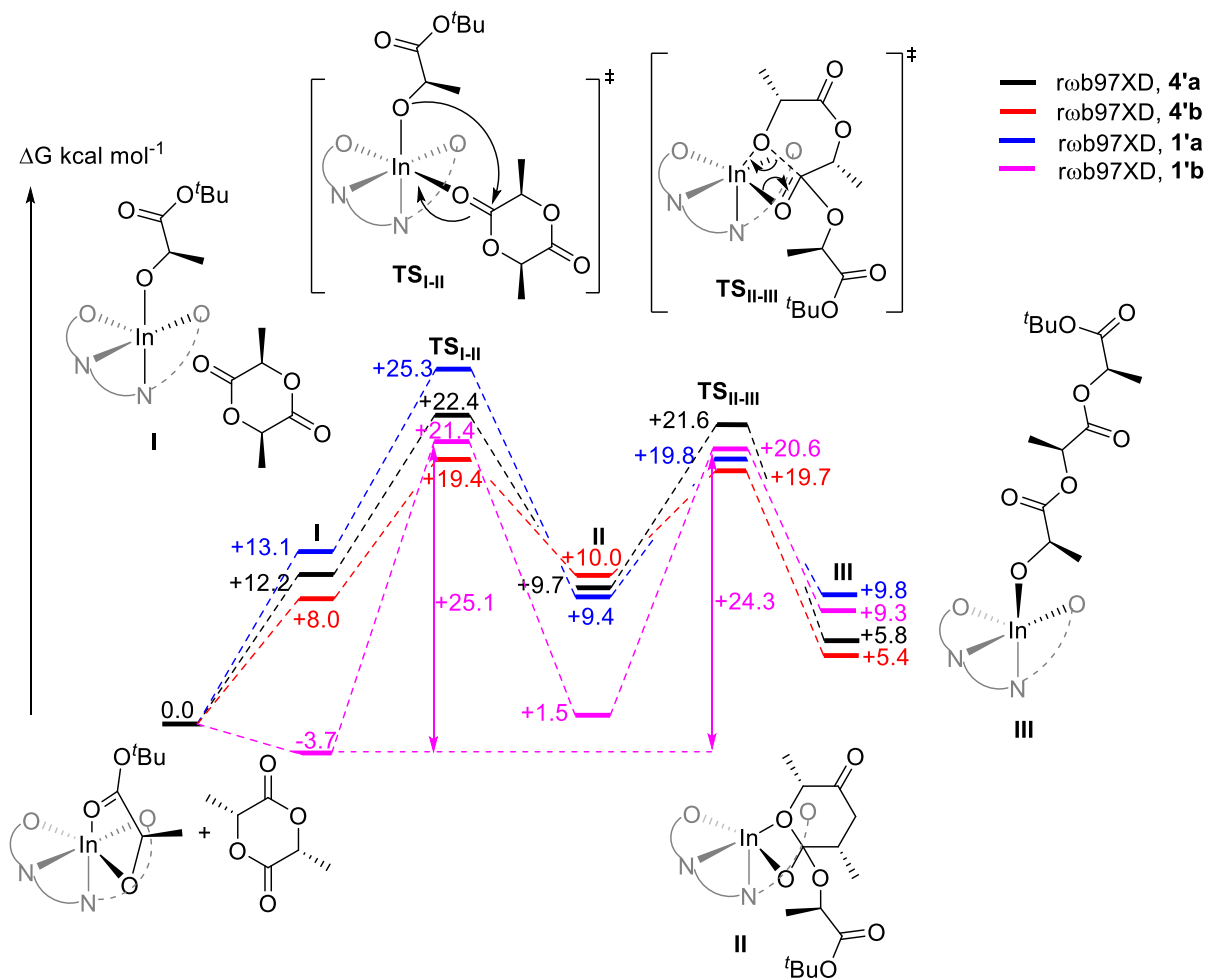
## Full free enthalpy landscape for the isotactic ring-opening of *D*-lactide by 4'a, 4'b, 1'a and 1'b



**Scheme S4.** Computed pathways of lowest free enthalpy TS barriers for the isotactic ring opening of *D*-lactide from 4'a (*trans*-re route; featured structures), 4'b (*trans*-si), 1'a (*trans*-re) and 1'b (*cis*-re) (see Tables S13 and S18). Calculations were performed using the M06L functional (with empirical dispersion correction factor, GD3, applied) basis set 6-31+G(d,p) for N, P and O atoms, 6-31G(d,p) for C and H atoms, and basis sets and pseudo potential lanl2dz for In atoms. Solvent effects were modelled using the SMD continuum model for THF at 298 K.



**Scheme S5.** Computed pathways of lowest free enthalpy TS barriers for the isotactic ring opening of *D*-lactide from **4'a** (*trans-re* route; featured structures), **4'b** (*trans-si*), **1'a** (*trans-re*) and **1'b** (*cis-re*) (see Tables S13 and S18). Calculations were performed using the PBE0 functional (with empirical dispersion correction factor, GD3), basis set 6-31+G(d,p) for N, P and O atoms, 6-31G(d,p) for C and H atoms, and basis sets and pseudo potential lanl2dz for In atoms. Solvent effects were modelled using the SMD continuum model for THF at 298 K.



**Scheme S6.** Computed pathways of lowest free enthalpy TS barriers for the isotactic ring opening of *D*-lactide from **4'a** (*trans*-re route; featured structures), **4'b** (*trans*-si), **1'a** (*trans*-re) and **1'b** (*cis*-re) (see Tables S13 and S18). Calculations were performed using the  $\omega$ b97XD functional, basis set 6-31+G(d,p) for N, P and O atoms, 6-31G(d,p) for C and H atoms, and basis sets and pseudo potential lanl2dz for In atoms. Solvent effects were modelled using the SMD continuum model for THF at 298 K.

**Table S19.** Functional benchmarking of the Gibbs free energy for the full reaction profile for the isotactic ring-opening of LA by *D*-lactate complexes **4'a**, **4'b**, **1'a** and **1'b** (Hartree). The pathways calculated were those of lowest isotactic free enthalpy TS barriers: *trans*-re route for **4'a**, *trans*-si for **4'b**, *trans*-re for **1'a** and *cis*-re for **1'b** (see Tables S13 and S18).

<b>4'a</b>	<b>I</b>	<b>TS<sub>I-II</sub></b>	<b>II</b>	<b>TS<sub>II-III</sub></b>	<b>III</b>
M06-L-D3	-3926.351672	-3926.333537	-3926.347055	-3926.330154	-3926.350114
PBE0-D3	-3922.860962	-3922.843886	-3922.864449	-3922.842525	-3922.863852
ωB97XD	-3925.815150	-3925.798922	-3925.819099	-3925.800242	-3925.825370
<b>4'b</b>	<b>I</b>	<b>TS<sub>I-II</sub></b>	<b>II</b>	<b>TS<sub>II-III</sub></b>	<b>III</b>
M06-L-D3	-3926.343808	-3926.332096	-3926.338866	-3926.333363	-3926.350141
PBE0-D3	-3922.862026	-3922.848475	-3922.857114	-3922.844050	-3922.866414
ωB97XD	-3925.822794	-3925.804620	-3925.819587	-3925.804077	-3925.826977
<b>1'a</b>	<b>I</b>	<b>TS<sub>I-II</sub></b>	<b>II</b>	<b>TS<sub>II-III</sub></b>	<b>III</b>
M06-L-D3	-4074.007018	-4073.991103	-4074.001797	-4073.995522	-4074.000886
PBE0-D3	-4070.372406	-4070.351135	-4070.374622	-4070.356452	-4070.373545
ωB97XD	-4073.411187	-4073.391714	-4073.417059	-4073.400425	-4073.416354
<b>1'b</b>	<b>I</b>	<b>TS<sub>I-II</sub></b>	<b>II</b>	<b>TS<sub>II-III</sub></b>	<b>III</b>
M06-L-D3	-4074.006115	-4074.003894	-4074.014000	-4073.994060	-4074.011787
PBE0-D3	-4070.390578	-4070.356251	-4070.384156	-4070.359097	-4070.373713
ωB97XD	-4073.437503	-4073.397405	-4073.429139	-4073.398772	-4073.416648

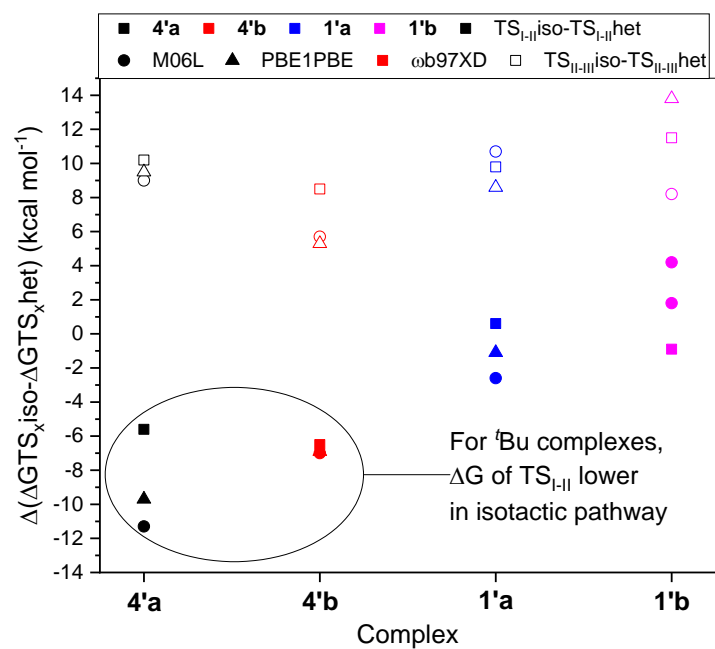


**Figure S86.** a)  $\Delta\Delta G$  (isotactic–heterotactic) of  $TS_{I-II}$  (filled) and  $TS_{II-III}$  (unfilled) for the isotactic and heterotactic opening of lactide for complexes **4'a** (black), **4'b** (red) and **1'a** (blue) using M06L (square), PBE0(circle) and  $\omega$ b97XD (triangle) functionals

## Investigation of catalytic pockets for transition states $\text{TS}_{\text{I-II}}$ for **4'a**, **4'b**, **1'a** and **1'b**

Comparison between the lowest computed energy pathways revealed that across the range of functionals tested,  $\text{TS}_{\text{I-II}}$  was almost exclusively the determining transition state for the complexes bearing diphenyl substituents on the phosphorus atoms. However, the differences in the associated  $\text{TS}_{\text{I-II}}$  barriers in the isotactic and heterotactic pathways were small. Upon introducing a *tert*-butyl substituent on the phosphorus atoms, the activation barriers associated with  $\text{TS}_{\text{I-II}}$  diverged, increasing for the heterotactic pathway and decreasing for the isotactic pathway. No correlation between the improved isoselectivities of **4'a-b** over **1'a-b** and the activation barriers associated with  $\text{TS}_{\text{II-III}}$  was found. The catalytic pocket around the metal centre for  $\text{TS}_{\text{I-II}}$  transition states was, therefore, further analyzed using steric maps generated from the SambVca 2 web tool developed by Cavallo and co-workers (Fig. S87).<sup>14</sup>

In order to consider the sole steric contribution of the ligand, *D*-LA and *D*-lactate were deleted from the  $\text{TS}_{\text{I-II}}$  structures prior to the calculation of the steric maps. Three steric maps were calculated per structure, centered on the In atom, with bond radii scaled by 1.17 at sphere radii of 3.5 Å, 6.0 Å and 9.2 Å. The range of radii were selected to test whether the diphenyl substituents affected any substantial changes to the close coordination sphere of In (scaled sphere radius ~3.5 Å), to the geometry at the P atoms (scaled sphere radius ~6.0 Å) or to the ligand as a whole (scaled sphere radius ~9.2 Å). The xy surface was chosen as the P=N/In or phenoxide/In plane (depending on the initial coordination of the lactide) and the z axis was defined along the O-In bond between *D*-lactate and In atoms. H atoms were included in the calculations.

At a given sphere radius, no specific interaction could be singled out as responsible for the observed increase in  $\text{TS}_{\text{I-II}}$  energies for the diphenyl substituted complexes. This suggests that subtler effects of the size and shape of the catalytic pockets may be at play.

Next, buried volumes were calculated from the 3.5 Å radius steric maps as they would represent best the catalytic pocket inside which the nucleophilic attack of the monomer occurs, encompassing the close coordination sphere of the metal centre while remaining free from the influence of longer range structural features. These values were plotted against the computed energies of  $\text{TS}_{\text{I-II}}$ . All heterotactic  $\text{TS}_{\text{I-II}}$  structures computed from **4'a** and **4'b** showed higher buried volumes than those derived from **1'a**, suggesting that the improved isoselectivity of **4** over **1** is governed by kinetics and of steric origin.

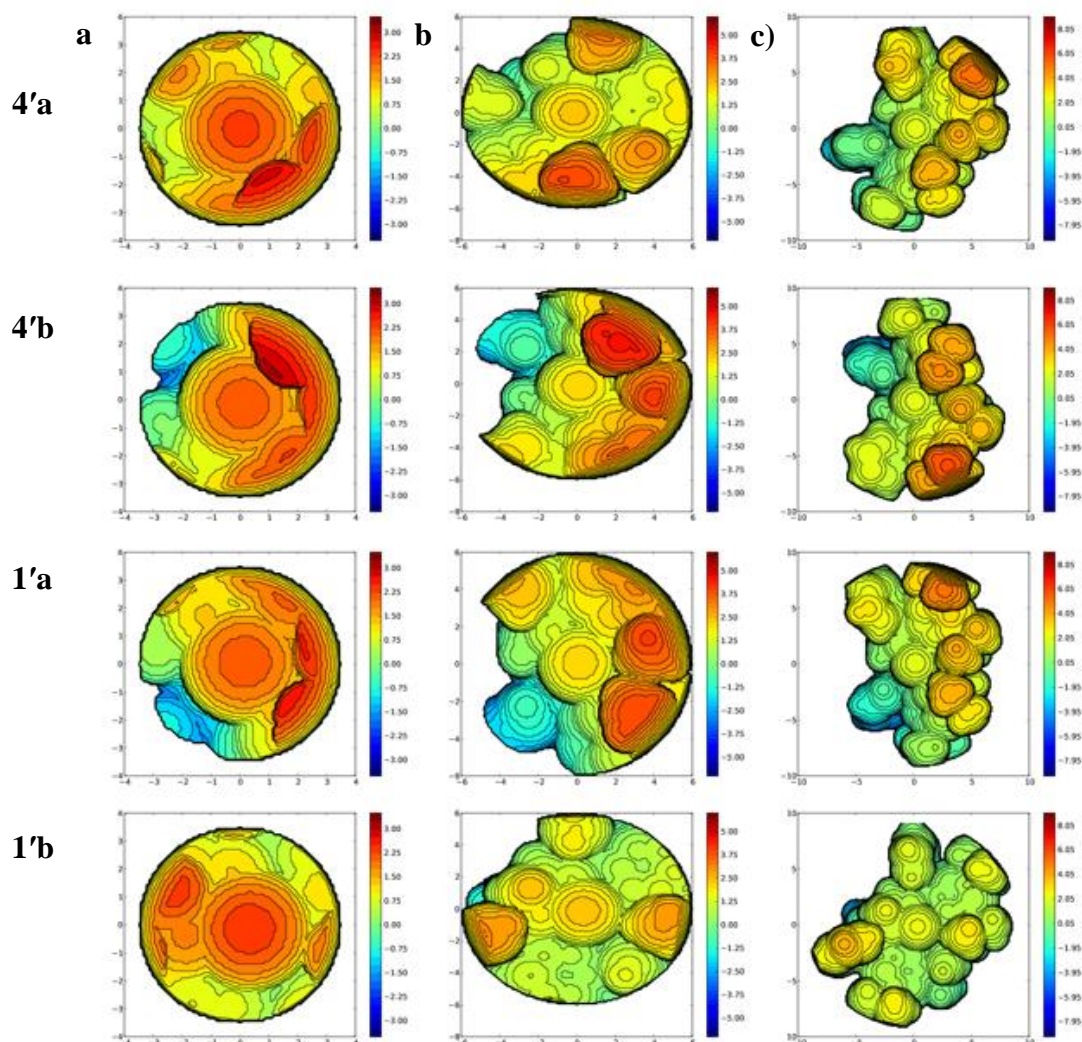
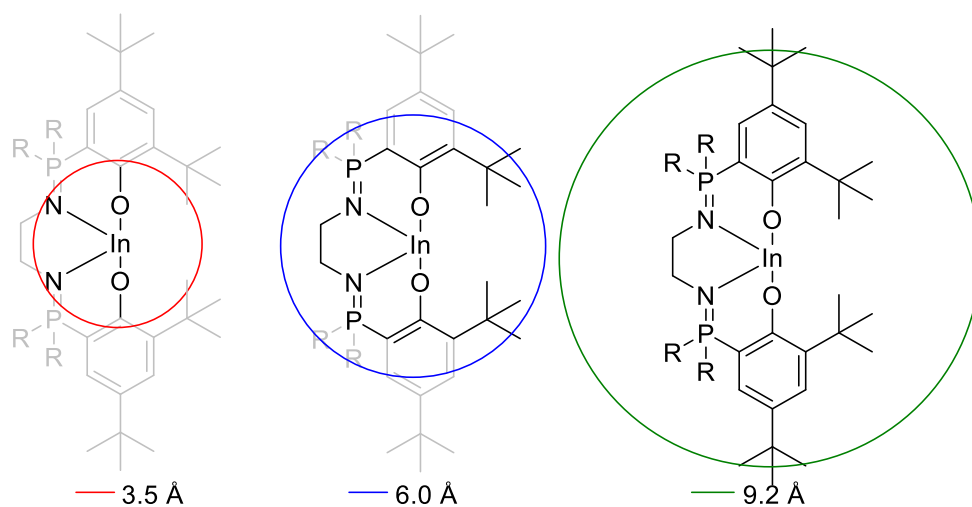


**Figure S87.** Representative steric maps generated for **4'a** (top line), **4'b** (second from top line) **1'a** (second from bottom line) and **1'b** (bottom line) from isotactic **TSr-II** structures calculated with the M06L functional at sphere radius = 3.5 (a), 6.0 (b) and 9.2 (c) Å scaled by 1.17

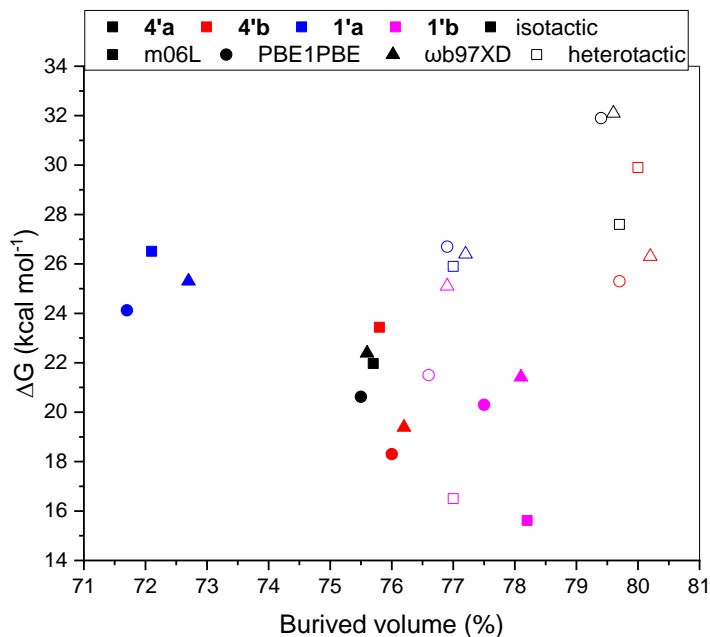


**Figure S88.** Buried volume at sphere radius = 3.5 Å (scale factor 1.17) vs  $\Delta G$  of isotactic (filled) and heterotactic (unfilled)  $\text{TS}_{\text{I-II}}$  for complexes **4'a** (black), **4'b** (red), **1'a** (blue) and **1'b** (magenta) using M06L (square), PBE0(circle) and  $\omega\text{b97XD}$  (triangle) functionals.

**Table S20.** % buried volume (at sphere radius = 3.5 Å, scale factor 1.17) vs  $\Delta G$  of  $\text{TS}_{\text{I-II}}$  for the lowest enthalpy path of isotactic and heterotactic ring-opening with complexes **4'a**, **4'b**, **1'a** and **1'b** ( $\text{kcal mol}^{-1}$ )

<i>D</i> -lactate model	Catalyst 4 ('BuPhP phosphasalen)				Catalyst 1 (Ph <sub>2</sub> P phosphasalen)			
	4'a		4'b		1'a		1'b	
Transition State	$\text{TS}_{\text{I-II}}$	% bv	$\text{TS}_{\text{I-II}}$	% bv	$\text{TS}_{\text{I-II}}$	% bv	$\text{TS}_{\text{I-II}}$	% bv
ROP of <i>D</i> -LA (isotactic)								
M06-L-D3	+22.0	75.7	+23.4	75.8	26.5	72.1	+15.6	78.2
PBE0-D3	+20.6	75.5	+18.3	76.0	24.1	71.7	+21.5	77.5
$\omega\text{B97XD}$	+22.4	75.6	+19.4	76.2	25.3	72.7	+25.1	78.1
ROP of <i>L</i> -LA (heterotactic)								
M06-L-D3	+27.6	79.7	+29.9	80.0	+25.9	77.0	+16.5	77.0
PBE0-D3	+31.9	79.4	+25.3	79.7	+26.7	76.9	+19.7	76.6
$\omega\text{B97XD}$	+32.1	79.6	+26.3	80.2	+26.4	77.2	+20.9	76.9

## S5. References

1. A. Kowalski, A. Duda and S. Penczek, *Macromolecules*, 1998, **31**, 2114–2122.
2. G. Sheldrick, *Acta Cryst. A*, 2008, **64**, 112–122.
3. L. Farrugia, *J. Appl. Crystallogr.*, 2012, **45**, 849–854.
4. A. L. Spek, *Acta Crystallogr. Sect. C Struct. Chem.*, 2015, **71**, 9–18.
5. A. L. Spek, *J. Appl. Crystallogr.*, 2003, **36**, 7–13.
6. V. Kavala, S. Naik and B. K. Patel, *J. Org. Chem.*, 2005, **70**, 4267–4271.
7. L.-P. He, M. Hong, B.-X. Li, J.-Y. Liu and Y.-S. Li, *Polymer*, 2010, **51**, 4336–4339.
8. (a) C. Bakewell, T.-P.-A. Cao, N. Long, X. F. Le Goff, A. Auffrant and C. K. Williams, *J. Am. Chem. Soc.*, 2012, **134**, 20577–20580; (b) T.-P.-A. Cao, A. Buchard, X. F. Le Goff, A. Auffrant and C. K. Williams, *Inorg. Chem.*, 2012, **51**, 2157–2169.
9. J. Beament, M. F. Mahon, A. Buchard and M. D. Jones, *New J. Chem.*, 2017, **41**, 2198–2203.
10. D. Myers, A. J. P. White, C. M. Forsyth, M. Bown and C. K. Williams, *Angew. Chem. Int. Ed.*, 2017, **56**, 5277–5282.
11. J. Coudane, C. Ustariz-Peyret, G. Schwach and M. Vert, *J. Polym. Sci. A: Polym. Chem.*, 1997, **35**, 1651–1658.
12. F. Chabot, M. Vert, S. Chapelle and P. Granger, *Polymer*, 1983, **24**, 53–59.
13. M. H. Rahaman and H. Tsuji, *Polym. Degrad. Stab.*, 2013, **98**, 709–719.
14. (a) L. Falivene, R. Credendino, A. Poater, A. Petta, L. Serra, R. Oliva, V. Scarano and L. Cavallo, *Organometallics*, 2016, **35**, 2286–2293; (b) L. Falivene, Z. Cao, A. Petta, L. Serra, A. Poater, R. Oliva, V. Scarano and L. Cavallo, *Nat. Chem.*, 2019, **11**, 872–879.